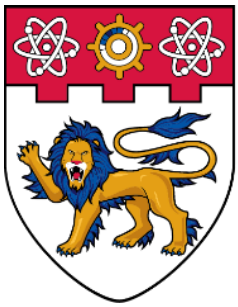

NANYANG TECHNOLOGICAL UNIVERSITY
SINGAPORE

FEMTOSECOND LASER POWER ABSORPTION OF GLASS

ARUN SATYAL

SCHOOL OF MECHANICAL AND AEROSPACE ENGINEERING

2020

FEMTOSECOND LASER POWER ABSORPTION OF GLASS

ARUN SATYAL

SCHOOL OF MECHANICAL AND AEROSPACE ENGINEERING

A thesis submitted to Nanyang Technological University in partial fulfilment of the requirement for the degree of

Doctor of Philosophy

2020

Statement of originality

I hereby certify that the work embodied in this thesis is the result of original research, is free of plagiarized materials, and has not been submitted for a higher degree to any other University or Institution.

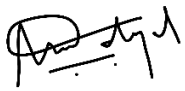

27 July 2020

. . . . . .

Date

. . . . . .

Arun Satyal

Supervisor declaration statement

I have reviewed the content and presentation style of this thesis and declare it is free of plagiarism and of sufficient grammatical clarity to be examined. To the best of my knowledge, the research and writing are those of the candidate except as acknowledged in the Author Attribution Statement. I confirm that the investigations were conducted in accord with the ethics policies and integrity standards of Nanyang Technological University and that the research data are presented honestly and without prejudice.

27 July 2020

. . . . . .

Date

. . . . . .

Prof Lam Yee Cheong

Authorship attribution statement

This thesis contains material from one paper accepted at conferences in which I am listed as an author.

Part of Chapter 4 is published as A. Satyal, J.C. Hernandez Castaneda, Y. C. Lam and H. Y. Zheng. *Nonlinear absorption of ultrashort laser pulse of chemically strengthened glass*. Proceedings of LPM2017, The 18th International Symposium on Laser Precision Microfabrication (2017)

The contributions of the co-authors are as follows:

- Prof Lam and Dr Zheng suggested the project and provided the direction and edited the manuscript drafts.
- Dr Hernandez and I designed the experiment.
- I performed all the laboratory works. I designed and computed the mathematical model with inputs from Prof Lam.
- I prepared the manuscript drafts. The manuscript draft was revised by Prof Lam, Dr Zheng and Dr Hernandez.

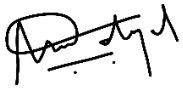

27 July 2020

. . . . . .

Date

. . . . . .

Arun Satyal

Abstract

The linear and nonlinear absorption of power from a femtosecond laser pulse by a chemically strengthened glass, Gorilla Glass 2320, has been studied. Laser irradiation with short pulsed laser results in high-intensity laser interacting with the sample. As a result, even a transparent material for the given laser wavelength would undergo optical breakdown. In addition to linear absorption, the optical breakdown results in nonlinear absorption. Laser power absorption is quantified through the coefficients of absorption, viz. coefficient of linear absorption and coefficient of nonlinear absorption. Z-scan technique, being one of the widely adopted and effective experimental technique for optical characteristics quantification of material, has been adopted for the determination of these coefficients of absorption.

In the Z-scan technique, to vary the laser beam intensity, a sample is translated along the axial direction of laser propagation passing through the focal plane. The laser power transmitted through the sample is recorded and analysed. When a sample is far away from the focal plane, the irradiated laser beam diameter is large and thus the laser beam intensity is low. In this low intensity region, the laser power is absorbed only through linear absorption. In contrast, when the sample is placed at or near the focal plane the incident laser beam diameter is small and thus the laser beam intensity is high. As a result of this high laser intensity, the laser power is absorbed through both linear and nonlinear absorption.

However, existing formulation in the literature of the overall absorption coefficient, consisting of both linear and nonlinear absorption coefficients, is insufficient to account for the delineation of the linear and nonlinear absorption regions. Indeed, there is no consideration of the transition from one region to the other; the units for the overall, linear and nonlinear coefficients of absorption are also inconsistent.

Here, a new formulation is proposed to account for the transition, and thus the delineation, between linear and nonlinear absorption. This is achieved through the introduction of the Nonlinear Absorption Threshold Intensity (NATI), which is defined as the laser power intensity at which the laser power absorption transits from linear laser power absorption to nonlinear laser power absorption. With the introduction of NATI, this formulation has a consistent unit for all the coefficients of absorption. Over a wide absorption range (linear and nonlinear), analyses demonstrate that this new formulation can describe the experimental observations far better than the existing formulation in the literature.

Sample thickness has been an important parameter in the analysis of laser power absorption using Z-scan technique. In the previous studies, a sample has to be classified as a “thick” or a “thin” sample based on the Rayleigh length of the lasing system. Different analytical methods are applicable for either the “thin” or the “thick sample. There is this implicit assumption that the original spatial laser beam distribution will remain constant as it traverses a “thin” sample, and may not be for a thick sample. However, there is no justification provided on this classification if a sample is “thin” or “thick, nor the validity of the implicit assumption.

This investigation shows that there is no physical basis for this classification. Indeed, it demonstrated that even for the so called “thin” sample, the spatial distribution of a laser beam changes as it traverses the sample thickness due to the nonlinear absorption of the laser power. The developed analytical approach here, together with the associated numerical procedure, can account for the changes of the spatial distribution of the laser beam as it traverses the thickness of the sample; this new approach can be applied to a sample of any thickness.

For nonlinear absorption, laser power absorption increases nonlinearly and rapidly with laser power. However, existing methods of analysis ignored the temporal distribution of laser power within a single pulse. For a proper and rigorous representation of nonlinear absorption, this temporal variation must be capture for the computation of the nonlinear absorption coefficient. This investigation has developed the necessary formulation and associated numerical procedure for this purpose.

Laser-induced plasma has been reported during laser-material interaction for different materials irradiated by ultrashort laser pulses. However, the effect of plasma formation on the study of laser power absorbed by the sample is lacking. Using high speed imaging, the laser-induced plasma was observed. It has been determined that the plasma decay time is less than 930 micro-seconds (μs). For the laser system with laser pulse duration of 130 femto-second (fs) and repetition rate of 1 milli-second (ms), this means that there is no laser-induced plasma interaction between two consecutive laser pulses. However, with the existing experimental

limitations, laser-induced plasma interaction within the same pulse could not be ruled. It was further observed that plasma formation was significant at high laser power intensity; in contrast at low laser power intensity, no/insignificant plasma formation was observed. Thus, for proper analysis of laser power absorption and subsequent calculation of absorption coefficient, it is recommended to carry out the experiments at low power intensity where the effect of plasma formation, and thus the energy associated with it, can be neglected.

Lastly, the obtained overall nonlinear absorption coefficients were independently verified through direct observation of temperature field during laser irradiation. Direct observation of temperature field was conducted using a thermal camera for in-situ measurements of temperature field during femtosecond laser irradiation of Gorilla Glass 2320. For the verification of overall absorption coefficients, a mathematical model for heat transfer during laser irradiation of Gorilla Glass 2320 was developed. The model accounts for femtosecond laser power absorption within Gorilla Glass 2320. Good correlations were obtained between the measured temperature fields with the predicted temperature fields as a result of heat energy absorption obtained through the overall absorption coefficients.

Acknowledgements

First, I would like to thank and acknowledge my supervisor Prof Lam Yee Cheong. His continuous support, inspirations, and guidance during my ups and downs have always motivated me. From the very first day, I have been admiring and appreciating his skills for the analysis and formulation of problems, and implementation of solutions. I feel fortunate that I have been able to learn from his knowledge and experience. His philosophy on academics and on personal life has always motivated me to be better. I cannot thank him enough. I am very fortunate that he accepted me as his student. I still have a lot to learn from Prof Lam. Thank you for this opportunity.

I would like to thank my co-supervisor Dr Wang Zhongke from Singapore Institute of Manufacturing Technology (SIMTech). His valuable inputs and feedbacks have always inspired me to do better. I would also like to thank my former co-supervisor Dr Zheng Hongyu. His support and guidance have always motivated me. Similarly, I would like to thank Dr Hernandez Castaneda Juan Carlos. Dr Carlos has always provided me with his support and guidance whenever I needed any. I am really fortunate to have been able to learn from all of you. Thank you.

I cannot miss my seniors and colleagues who have always been there for me. I would personally like to thank Dr Tai Jiayan, Dr Lim Chun Yee, Dr Lim Chun Ping, Dr Lim An Eng, Dr Wang Bing and Dr Nguyen Quoc Mai Phuong. I am very grateful for your support and help I have received from you.

I am grateful to Nanyang Technological University and School of Mechanical and Aerospace Engineering for providing me with resources and facilities for my work. I would also like to thank A*STAR and SIMTech for awarding me the SINGA scholarship for carrying out this research.

Finally, I would like to thank my family and my friends. I have always found my encouragement and strength to excel further through your love and understanding.

Table of contents

Statement of originality ..... - 1 -

Supervisor declaration statement ..... - 2 -

Authorship attribution statement ..... - 3 -

Abstract ..... - 4 -

Acknowledgements ..... - 8 -

Table of contents ..... - 10 -

List of figures ..... - 15 -

List of tables ..... - 25 -

Chapter 1: Introduction ..... - 26 -

1.1 Background ..... - 26 -

1.2 Motivation ..... - 29 -

1.3 Objective ..... - 33 -

1.4 Scopes ..... - 34 -

1.5 Organization of the thesis ..... - 34 -

Chapter 2: Literature review ..... - 37 -

2.1 Short pulse laser ..... - 37 -

2.2 Absorption ..... - 40 -

2.2.1 Linear absorption ..... - 40 -

2.2.2 Nonlinear absorption ..... - 41 -

2.2.3 Summary ..... - 46 -

2.3 Optical polarization ..... - 46 -

2.3.1 Polarization formulation ..... - 47 -
2.3.2 Characteristics of n-th order polarization ..... - 48 -
2.3.3 Absorption and refraction with respect to polarizaiton ..... - 49 -
2.4 Nonlinear optical characterization techniques ..... - 51 -
2.4.1 Optical Kerr gate technique ..... - 51 -
2.4.2 Wave-mixing technique ..... - 51 -
2.4.3 Z-scan technique ..... - 52 -
2.5 Z-scan technique ..... - 53 -
2.5.1 Original Z-scan technique ..... - 53 -
2.5.2 Unresolved issues in nonlinear absorption and Z-scan technique ... - 74 -
2.6 Optical breakdown and ablation ..... - 77 -
2.6.1 Laser ablation of material ..... - 77 -
2.6.2 Laser-induced plasma ..... - 80 -
2.7 Thermography ..... - 83 -
2.7.1 Fundamentals of thermography ..... - 84 -
2.7.2 Applications of thermography in ultrashort pulsed laser irradiation - 89 -
Chapter 3: Methodology ..... - 91 -
3.1 Introduction ..... - 91 -
3.2 Laser system ..... - 91 -
3.3 Z-scan technique ..... - 92 -
3.3.1 Material and devices employed ..... - 92 -
3.3.2 Experimental setup ..... - 93 -

3.4 Thermal Measurement ..... - 97 -

3.4.1 Materials and devices employed ..... - 97 -

3.4.2 Experimental setup ..... - 98 -

3.5 Plasma observation with high-speed imaging ..... - 101 -

3.5.1 Materials and devices employed ..... - 102 -

3.5.2 Experimental setup ..... - 104 -

Chapter 4: Optical absorption characterization ..... - 108 -

4.1 Introduction ..... - 108 -

4.2 Theoretical analysis ..... - 109 -

4.2.1 Nonlinear absorption coefficient formulation ..... - 112 -

4.2.2 Formulation of laser energy distribution within the material ..... - 114 -

4.2.3 Volumetric energy absorption formulation ..... - 118 -

4.3 Computational procedure ..... - 120 -

4.3.1 Nonlinear absorption threshold intensity ..... - 121 -

4.3.2 Determination of the coefficient of linear absorption ..... - 124 -

4.3.3 Determination of coefficient of nonlinear absorption ..... - 130 -

4.4 Results and discussion ..... - 134 -

4.4.1 Existing formulation of absorption coefficient in literature without nonlinear absorption threshold intensity ..... - 139 -

4.4.2 Rayleigh length and sample thickness ..... - 143 -

4.4.3 Intensity profiles of the laser beam within the material ..... - 145 -

4.5 Summary ..... - 149 -

Chapter 5: Laser-induced plasma during femtosecond laser irradiation .... - 151 -

5.1 Introduction.....- 151 -

5.2 Plasma imaging.....- 152 -

5.2.1 Optical filter selection.....- 153 -

5.2.2 Plasma observation.....- 160 -

5.3 Plasma formation during Z-scan measurement .....- 170 -

5.4 Summary.....- 175 -

Chapter 6: Thermal characterization of material during laser irradiation .. - 178 -

6.1 Introduction.....- 178 -

6.2 Theoretical analysis.....- 179 -

6.2.1 Governing equation.....- 180 -

6.2.2 Heat source .....- 181 -

6.2.3 Boundary conditions .....- 182 -

6.2.4 Meshing and computational time steps .....- 184 -

6.3 Experimental observations of thermal profiles.....- 185 -

6.3.1 Spatial temperature distribution.....- 186 -

6.3.2 Temporal temperature distribution.....- 187 -

6.3.3 Simulation of thermal profiles .....- 191 -

6.3.4 Summary.....- 197 -

Chapter 7: Conclusions and future work .....- 200 -

7.1 Conclusions.....- 200 -

7.2 Future work.....- 208 -

References ..... - 210 -

Appendix I ..... - 218 -

Appendix II ..... - 231 -

Appendix III ..... - 232 -

Appendix IV ..... - 234 -

List of figures

Figure 2-1: Timescale of various electron and lattice processes in semiconductor interaction, green bar shows characteristics time of each process [12].....- 39 -

Figure 2-2 : Schematic diagram of (a) multiphoton ionization process ionizing by simultaneous absorption of m photons (b) tunnelling (c) avalanche ionization [11]……...- 43 -

Figure 2-3 : Schematic Z-scan setup in which normalized transmission (ratio of power detected by detector D2 to power detected by reference detector D1) is recorded as function of sample position z [15]. .....- 54 -

Figure 2-4: (a) Normalized transmission as a function of z-position in closed aperture Z-scan technique, (b) Normalized transmission as a function of z-position in open aperture Z-scan technique [42].....- 56 -

Figure 2-5: Calculated normalized transmission with on-axis phase shift of ± 0.25 with small aperture of S=0.01 as a function of z-position in term of unit Rayleigh Length, z_o [15]. .....- 59 -

Figure 2-6: Normalized Z-scan transmittance of ZnSe measured using picosecond laser pulse at $\lambda=532$ nm with open aperture i.e. $S=1$, solid line represent the theoretical analysis, dots are experimentally obtained results [15].....- 61 -

Figure 2-7 : Z-scan for different sample thickness of CS_2, fitted with theoretical curve from the numerical solution [39].....- 66 -

Figure 2-8 : Closed-aperture z-scan curve, with nonlinear phase shift $\Delta\emptyset_R = 0.5$ and sample length $l = L/z_o = 6$: (a) numerical solution [46] , (b) analytical solution [46], (c) analytical solution [72] (d) analytic solution [73].....- 72 -

Figure 2-9: Linear photon absorption spectra of PS [74]. .....- 73 -

Figure 2-10: Normalized transmittance curve for open aperture z-scan technique with power at (a) 5.2 mW, (b) 10.4 mW, (c) 14.4 mW and (d) 23.5 mW [74] (black dots are experimental data and red line is theoretically analysed curve) .....- 74 -

Figure 2-11: Ablation depth per pulse for copper with varying laser fluence. The solid line represents the ablation depth at low fluence region (described by equation (2-38)) whereas the dashed line represents the ablation depth at higher fluence region (described by equation (2-39)). In lower fluence region, threshold fluence $\emptyset_{th}^{a} = 140mJ/cm^2$ whereas, the threshold fluence for high fluence region $\emptyset_{th}^{l} = 460mJ/cm^2$ [99].....- 79 -

Figure 2-12: (a) Different types of electromagnetic waves with their respective frequency and wavelength. (b) Thermal infrared region showing short-wave (SW), medium-wave (MW) and long-wave (LW) infrared region with their respective wavelength in micro-meter [110]. .....- 84 -

Figure 2-13 : Radiance of black body at different temperature. The rainbow colouring denotes the visible light range. Discontinuous red line passes the maximum radiance for different temperature [110]. .....- 87 -

Figure 3-1: Schematic diagram of open aperture Z-scan technique.....- 94 -

Figure 3-2: Schematic diagram for direct observation of temperature distribution during laser irradiation.....- 99 -

Figure 3-3: Response of CMOS photodiodes with coverings of (a) No polycrystalline silicon, (b) the first polycrystalline silicon layer, (c) the second polycrystalline silicon layer, and (d) both polycrystalline silicon layers [114].....- 103 -

Figure 3-4: Schematic diagram to observe plasma formation during laser irradiation .....- 104 -

Figure 4-1: Schematic diagram of the laser beam with a sample at z-distance away from the focal plane.....- 112 -

Figure 4-2: Schematic diagram of laser irradiation focused inside the material at distance s below the surface. $I_o(r,t)$ is incoming laser intensity profile at the entry surface of the sample at given values of r and t, $I(z,r,t)$ is intensity at a position '*z*' below the surface of the sample and $I(l,r,t)$ is the intensity profile at the exit surface of the glass. E_s is total energy entering the surface and E_e is total energy exiting the surface.....- 115 -

Figure 4-3: Polar representation of a radial system with *dr* elemental radial length and $d\theta$ elemental revolving angle. $I(z,r,t)$ is the fluence at the elemental area ABCD. .....- 117 -

Figure 4-4: Elemental volume in cylindrical coordinate with *dr* as elemental radial length, *dz* as elemental axial length and $d\theta$ as the elemental revolving angle. $I(z,r,t)$ is the laser intensity when it enters the elemental volume at position r distance away from the beam axial position and z-position below the surface at any given time t.

I(z+dz,r,t) is the laser intensity at the exit of the same elemental volume of thickness dz. .....- 118 -

Figure 4-5: Experimental absorption results by 500 μm Gorilla 2320 glass using Z-scan at a laser power of 99.6 mW showing regions of linear and nonlinear absorptions. .....- 121 -

Figure 4-6: Rate of change of absorption with respect to z-position. .....- 122 -

Figure 4-7: Absorption by 500 μm Gorilla 2320 glass using Z-scan at a laser power of 21.8 mW. The peak intensity was 2.13×10^{14} W/cm^2. Exp 1, Exp 2, and Exp 3 are obtained from three different experiments whereas the red solid line is the numerically calculated absorption using average values of the linear and the nonlinear coefficients, and the average value of the nonlinear absorption threshold intensity.....- 135 -

Figure 4-8: Absorption by 500 μm Gorilla 2320 glass using Z-scan at a laser power of 58.2 mW. The peak intensity was 1.34×10^{14} W/cm^2. Exp 1, Exp 2, and Exp 3 are obtained from three different experiments whereas the red solid line is the numerically calculated absorption using average values of the linear and the nonlinear coefficients, and the average value of the nonlinear absorption threshold intensity.....- 136 -

Figure 4-9: Absorption by 500 μm Gorilla 2320 glass using Z-scan at a laser power of 99.6 mW. The peak intensity was 2.13×10^{14} W/cm^2. Exp 1, Exp 2, and Exp 3 are obtained from three different experiments whereas the red solid line is the numerically calculated absorption using average values of the linear and the

nonlinear coefficients, and the average value of the nonlinear absorption threshold intensity..... - 137 -
Figure 4-10: Absorption by 500 μm Gorilla 2320 glass using Z-scan at a laser power of 21.6 mW. The peak intensity was 2.13×10^{14} W/cm^2. Exp 1, Exp 2, and Exp 3 are obtained from three different experiments whereas the red solid line is the numerically calculated absorption (line of best fit) based on equation (1-1) without consideration for nonlinear absorption threshold intensity..... - 141 -
Figure 4-11: Absorption by 500 μm Gorilla 2320 glass using Z-scan at laser power of 21.6 mW. The peak intensity was 2.13×10^{14} W/cm^2. Exp 1, Exp 2, and Exp 3 are obtained from three different experiments whereas the red solid line is the numerically calculated absorption by matching of the maximum absorption values between experimental observations and numerical calculations based on equation (1-1) without consideration for nonlinear absorption threshold intensity..... - 143 -
Figure 4-12: Intensity in the axial direction of laser propagation with maximum temporal peak intensity when the laser is focused at the centre of glass (z = 0 mm). Input power is 21.6 mW. The dotted line shows the intensity variation vs thickness for linear absorption only to give the same intensity value at the exit surface of the glass, indicating that there was only linear absorption for thickness greater than 220 μm..... - 144 -
Figure 4-13: Intensity distribution profile of the laser beam at the entry surface and the exit surface of the laser beam (a) radial direction (b) temporal time step... - 147 -

Figure 4-14: Intensity distribution profile of the laser beam at the exit surface of the laser beam with Gaussian fits (a) radial direction (b) temporal time step .....- 148 -
Figure 5-1: Consecutive images of laser irradiation captured at a frame rate of 60 fps and shutter speed of 1/60 s without any optical filter. The laser is operated at a repetition rate of 1kHz with an average power of 102.05 mW. First laser irradiation is observed in time 16.667 ms in frame (b). Red-line denotes the sample surfaces. The laser is irradiated from the surface on the right.....- 154 -
Figure 5-2: Spectral response of (a) FELH0850 (cut-on filter with cut-on wavelength at 850 nm) (b) FLSH0750 (cut-off filter with a cut-off wavelength of 750 nm) (as provided by the supplier) .....- 156 -
Figure 5-3: Consecutive images of laser irradiation captured at a frame rate of 60 fps and shutter speed of 1/60 s using FELH0850 (cut-on filter with cut-on wavelength at 850 nm). The laser is operated at a repetition rate of 1kHz with an average power of 102.05 mW.....- 158 -
Figure 5-4: Consecutive images of laser irradiation captured at a frame rate of 60 fps and shutter speed of 1/60 s using FLSH0750 (cut-off filter with a cut-off wavelength of 750 nm). The laser is operated at a repetition rate of 1kHz with an average power of 102.05 mW. Red-line indicates the sample surfaces. The laser is irradiated from the surface on the right.....- 159 -
Figure 5-5: Consecutive images of laser irradiation captured at a frame rate of 1000 fps and shutter speed of 1/1000 s using FLSH0750 (cut-off filter with a cut-off wavelength of 750 nm). The laser is operated at a repetition rate of 1kHz with an

average power of 102.05 mW. Red-line indicates the sample surfaces. The laser is irradiated from the surface on the right. .....- 162 -
Figure 5-6: Consecutive images of laser irradiation captured at a frame rate of 3,000 fps and shutter speed of 1/3,000 s using FLSH0750 (cut-off filter with a cut-off wavelength of 750 nm). The laser is operated at a repetition rate of 1kHz with an average power of 102.05 mW. Red-line indicates the sample surfaces. The laser is irradiated from the surface on the right. .....- 164 -
Figure 5-7: Images of laser irradiation captured at a frame rate of 10,000 fps and shutter speed of 1/10,000 s using FLSH0750 (cut-off filter with a cut-off wavelength of 750 nm). The laser is operated at a repetition rate of 1kHz with an average power of 102.05 mW. Red-line indicates the sample surfaces. The laser is irradiated from the surface on the right. (Note: - not all images shown are consecutive.).....- 165 -
Figure 5-8: Images of laser irradiation captured at a frame rate of 50,000 fps and shutter speed of 1/50,000 s using FLSH0750 (cut-off filter with a cut-off wavelength of 750 nm). The laser is operated at a repetition rate of 1kHz with an average power of 102.05 mW. Red-line indicates the sample surfaces. The laser is irradiated from the surface on the right. Here in this figure, the images are not consecutive. ..- 167 -
Figure 5-9: Images of laser irradiation captured at a frame rate of 300,000 fps and shutter speed of 1/300,000 s using FLSH0750 (cut-off filter with a cut-on wavelength of 750 nm) The laser is operated at a repetition rate of 1kHz with an average power of 102.05 mW. Red-line indicates the sample surfaces. The laser is irradiated from the surface on the right. (Note: - not all images shown are consecutive.).....- 168 -

Figure 5-10: Images of laser irradiation captured at a frame rate of 930,000 fps and shutter speed of 1/930,000 s using FLSH0750 (cut-off filter with a cut-off wavelength of 750 nm). The laser is operated at a repetition rate of 1kHz with an average power of 102.05 mW. Red-line indicates the sample surfaces. The laser is irradiated from the surface on the right. (Note: - not all images shown are consecutive.).....- 169 -

Figure 5-11: Consecutive images of laser irradiation captured at a frame rate of 1,000 fps and shutter speed of 1/1,000 s using FLSH0750 (cut-off filter with a cut-off wavelength of 750 nm) with laser beam focused at the centre of the glass (i.e. z = 0 mm). The laser is operated at a repetition rate of 1kHz with an average power of 101.65 mW. Red-line indicates the sample surfaces. The laser is irradiated from the surface on the right. .....- 171 -

Figure 5-12: Consecutive images of laser irradiation captured at a frame rate of 1,000 fps and shutter speed of 1/1,000 s using FLSH0750 (cut-off filter with a cut-off wavelength of 750 nm) with laser beam focused at the entry surface of the sample (i.e. z = -0.250 mm). The laser is operated at a repetition rate of 1kHz with an average power of 101.65 mW. Red-line indicates the sample surfaces. The laser is irradiated from the surface on the right. .....- 172 -

Figure 5-13: Consecutive images of laser irradiation captured at a frame rate of 1,000 fps and shutter speed of 1/1,000 s using FLSH0750 (cut-off filter with a cut-off wavelength of 750 nm) with laser beam focused at z = 1 mm). The laser is operated

at a repetition rate of 1kHz with an average power of 101.65 mW. Red-line indicates the sample surfaces. The laser is irradiated from the surface on the right.....- 173 -
Figure 5-14: Consecutive images of laser irradiation captured at a frame rate of 1,000 fps and shutter speed of 1/1,000 s using FLSH0750 (cut-off filter with a cut-off wavelength of 750 nm) with laser beam focused at z = 2 mm The laser is operated at a repetition rate of 1kHz with an average power of 101.65 mW. Red-line indicates the sample surfaces. The laser is irradiated from the surface on the right.....- 174 -
Figure 6-1: Orientation of the sample during laser-material interaction simulation. Numbers provide the references to the specific surfaces. Arrow indicates the location and direction of the laser beam. .....- 183 -
Figure 6-2: Temperature profile distribution at the surface of the glass with z-distance varied from - 2 mm to 2 mm, at 1 s time intervals. The dotted white line shows two surfaces of the glass.....- 186 -
Figure 6-3: The sampling locations for the analysis of temporal temperature profile. .....- 188 -
Figure 6-4: Temporal temperature distribution at the surface perpendicular to the surface of laser irradiation for (a) z = - 2 mm, (b) z = - 1 mm (c) z = 0 mm, (d) z = 1 mm and (e) z = 2 mm.....- 189 -
Figure 6-5: Simulated and experimental temporal thermal profiles at z = - 2 mm at sampling locations (a) A, (b) B, (c) C, and (d) D(see Figure 6-3).....- 192 -
Figure 6-6: Simulated and experimental temporal thermal profiles at z = - 1 mm at sampling locations (a) A, (b) B, (c) C, and (d) D(see Figure 6-3).....- 193 -

Figure 6-7: Simulated and experimental temporal thermal profiles at z = 0 mm at sampling locations (a) A, (b) B, (c) C, and (d) D (see Figure 6-3) ..... - 194 -
Figure 6-8: Simulated and experimental temporal thermal profiles at z = 1 mm at sampling locations (a) A, (b) B, (c) C, and (d) D(see Figure 6-3) ..... - 195 -
Figure 6-9: Simulated and experimental temporal thermal profiles at z = 2 mm at sampling locations (a) A, (b) B, (c) C, and (d) D(see Figure 6-3) ..... - 196 -

List of tables

Table 2-1: Threshold Intensities for optical breakdown [13] .....- 42 -

Table 2-2: Nonlinear coefficients value for different alkoxy-substituted PPV [24] .....…- 63 -

Table 2-3: Nonlinear coefficients value for different chalcogenide glasses [27]- 64 -

Table 2-4: Values of γ calculated through the least-square fitting method and through analytical theory [39].....- 68 -

Table 3-1: Integra-C 1.0 specification.....- 91 -

Table 4-1: Calculated nonlinear absorption threshold intensities at different power levels.....- 124 -

Table 4-2: Computed coefficients of linear absorption at different power level…….. .....- 130 -

Table 4-3: Computed coefficients of nonlinear absorption at different power levels ..... .- 134 -

Table 4-4: Computed values of the linear absorption coefficient αo, the nonlinear absorption coefficient α_1, and the nonlinear absorption threshold intensity $I_{th.}$- 138 -

Chapter 1: Introduction

In this chapter, the background of linear and nonlinear absorptions and their measurement techniques are introduced. The advantages and disadvantages of the current techniques are highlighted. The objectives and scopes of this investigation are outlined. Finally, the structure of this thesis is presented.

1.1 Background

Laser is an effective and a versatile non-contact tool widely used in material processing, medicine and in research and development. Laser has been used for cutting, drilling, welding, and modifications of materials [1], and the processing of polymers [2, 3], metal [4-6], and glasses [7, 8], etc.

For different lasers, laser pulse time duration varies from infinite time to a few atto-second (as) [9, 10]. Infinite time duration lasers are continuous lasers; in contrast, lasers with finite time duration are known as pulsed lasers. Pulsed lasers can be further classified into long pulsed laser, short pulsed laser and ultrashort pulsed lasers based on the thermalization time [11].

Laser-material interaction commences with the absorption of laser photons by the substrate's electrons. When a laser photon is absorbed by an electron it will induce a thermodynamic non-equilibrium state. To regain the thermodynamic equilibrium state, the excited electrons must transfer their excess energy to the phonons or other electrons. This energy transfer process is called thermalization. The time in which this transfer of energy occurs is known as the thermalization time.

If the laser pulse duration is greater than the thermalization time of a material, the laser is classified as a long pulse laser. Conversely, if the laser pulse duration is shorter but comparable to the thermalization time, it is a short pulse laser; if the laser pulse duration is very much shorter than the thermalization time, then the laser is an ultrashort pulse laser. Usually a pulsed laser with laser pulse duration less than 1 ps is an ultrashort pulse laser [12].

In the linear absorption regime, for the laser energy to be absorbed by a material, the photon energy must be equal or greater than the material's band gap energy [13]. However, if the laser power intensity is sufficiently high, multiple photons can be simultaneously absorbed by the material through nonlinear absorption. For nonlinear absorption to occur, the combined energy of multiple photons must exceed the material's band gap energy. There are different absorption mechanisms for nonlinear absorption, viz. multiphoton ionization, tunnelling ionization and/or avalanche ionization. These mechanisms will be outlined in section 2.2.2.

The resulting absorption can be quantitatively defined in terms of the overall absorption coefficient consisting of both linear and nonlinear absorptions as [14, 15]:

$$\alpha(I) = \alpha + \beta I \tag{1-1}$$

$\alpha(I)$ is the laser-intensity-dependent overall coefficient, α is the coefficient of linear absorption and β is the coefficient of nonlinear absorption. Hitherto, Equation (1-1) is the accepted representation to account for both linear and nonlinear absorptions.

Many optical characterization techniques have been developed over the years for optical material characterization. Optical Kerr Gate technique, Wave-mixing technique and Z-scan technique are some of the popular optical characterization techniques. Z-scan technique, developed by Mansoor Sheik-Bahae et al. [14, 15] in the 1990s, is the most widely used technique due to its simplicity and accuracy [16]. Many variations of the Z-scan technique have been developed for nonlinear optical characterization of materials [16].

Nonlinear optical characterization of liquids [17-20], polymers [21-25], glasses [26-30], semiconductors [31-34] and organic materials [35-37] have been studied quantitatively. Due to its simplicity and accuracy, Z-scan technique is the most widely used nonlinear characterization technique [16]. The original Z-scan technique and its different variations have been widely adopted for the study of optical nonlinear properties of different materials [17-19, 22, 24, 25, 27-30, 33-35, 37-48]. Some of the variations of the original single Gaussian beam Z-scan technique include Elliptic Z-scan (EZ-scan) [40], Z-scan using a top-hat beam [18] instead of a Gaussian beam, two colour single beam Z-scan technique [44], reflection Z-scan for the measurement of surface optical properties [43] and eclipsed Z-scan technique [45].

1.2 Motivation

Ultrashort pulsed lasers have a diverse scope of material processing for different materials [49-55]. The short time duration of an ultrashort pulse of a laser leads to high peak power intensity. As a result, not only opaque, [56-60] but also transparent materials for a given laser wavelength can be processed using an ultrashort pulsed laser. Ultrashort pulsed lasers have been used in the processing polymers [61-63] and glasses [64-66]. During the processing of materials with an ultrashort pulsed laser, the heat-affected zone is minute in contrast to a long-pulsed laser [67-69]. As such, an ultrashort pulsed laser is capable of precise processing of materials [70].

For any material processing, the key parameter is the absorption of the laser energy. For ultrashort pulses, nonlinear absorption mechanism could well be dominant. It has been established that the nonlinear optical property of any material can only be instigated when the intensity of the incoming laser beam is sufficiently high.

The Z-scan technique relies on translating the sample to and away from (and passing through) the focal plane (discussed below in section 2.5). The intensity at different position will be different due to its different focusing (or defocusing) laser beam spot diameter. Far away from the focal plan and at low intensity, the only prominent mode of absorption is linear absorption. In contrast, at and around the focal plane with a small focusing laser spot and sufficiently high laser intensity, linear and nonlinear absorptions can occur but with nonlinear absorption being the dominant mode of absorption. As such, two distinct regions of absorption exist, namely (a) only linear absorption away from the focal plane and, (b) both linear and nonlinear absorptions

at and around the focal plane. In between these two regions, there is a transition region where both linear and nonlinear absorptions could well be equally important.

Indeed, to obtain the absorption coefficients, analyses and interpretation of the Z-scan experimental results are necessary. Hitherto, all these analyses rely fundamentally on equation (1-1) 1 for the definition of the overall absorption coefficient. It describes the change in the absorption of a material with laser intensity (I) as an independent variable. However, hitherto equation (1-1) have been used in the analyses without consideration of the delineation and/or transition between the linear absorption region and the dominant nonlinear absorption region. Indeed, equation (1-1) implicitly assumes that nonlinear absorption will always occurs; this is not exactly correct as there must be a threshold laser intensity below which there is only linear absorption. In addition, the formulation as stated in equation (1-1) does not have a consistent unit between the absorption coefficients; the unit of nonlinear absorption coefficient β is different, and therefore inconsistent, with the unit of linear and overall coefficient of absorption.

One of the requirements for the analyses of the experimental results obtained from the Z-scan technique or its variations is that the analytical methods must be based on either a "thin" sample approximation [14, 15, 19, 20, 22-24, 27-29, 33, 42, 44, 71] or a "thick" sample approximation [39, 46, 72-74]. Different analytical methods have been developed depending if the sample is "thick" [46, 72-74] or "thin" [32, 39, 40, 42].

A sample is classified as "thick" if its thickness is greater than the Rayleigh length of the lasing system; conversely the sample is "thin" if its thickness is less than the Rayleigh length. However, there is no justification provided on the classification if a sample is "thin" or "thick" based on the Rayleigh length. Indeed, as Rayleigh length is related to the laser and its optical system for an appreciation of the focusing depth, the physical rationale to employ Rayleigh length for the delineation of the sample thickness into "thin" or "thick" is not at all obvious or appropriate.

In the existing analyses of the Z-scan results, there is this added implicit assumption that the original spatial laser beam distribution will remain constant as it traverses a "thin" sample. However, nonlinear absorption is a strong function of the laser intensity. As an example, if the laser beam has a Gaussian beam distribution, the intensity at the centreline of the beam will be much higher than its perimeter, and much more laser power will be absorbed at the vicinity of the centreline. The power intensity along the centreline will be depressed quickly as compared to the beam's perimeter; as such, the spatial distribution of the laser beam will change as it traverses the sample. Thus, it is not entirely certain if this implicit assumption is appropriate even for a "thin" sample as there is no examination of the validity of this assumption.

When the peak power intensity of the laser beam is high, the material will be ablated, and the ablated plume interacts with an incoming laser beam to form plasma. Plasma can be induced by a nanosecond laser, a picosecond laser, or a femtosecond laser. For a nanosecond or picosecond laser pulse, the interaction is complex [75] as the

laser-induced plasma has enough time to grow. In contrast, a femtosecond laser pulse has very little time for the growth of the plasma. Due to the shorter pulse duration of a femtosecond laser compared to other lasers, a femtosecond laser has a higher efficiency of turning ejected fumes into plasma [76]. Different Z-scan measurement techniques have been adopted for the characterization of nonlinear optical properties of materials using nanosecond lasers [18, 39], picosecond lasers [22, 24, 27] and femtosecond lasers [19, 37, 47, 48]. However, there is little attention on the effects of plasma formation, in particular for absorption coefficient determination.

For a holistic and rigorous study of absorption, both linear and nonlinear absorption and their delineation and transition have to be considered. Previous studies by our group has shown that in copper, silicon, or steel, more than 50%, 66.7%, and 67% respectively of the total incident laser energy was deposited into the materials [77-79]. However, all these materials were not transparent for the employed laser with a wavelength of λ=775 nm. Our group has also studied polystyrene and demonstrated that significant heat deposition occurs during femtosecond laser irradiation [63]. However, polystyrene is almost fully transparent at the laser wavelength of λ=795 nm. It would be of interest to employ a different material which is not fully transparent or opaque to the wavelength of the employed laser. A good material candidate for this investigation is Gorilla Glass 2320, a chemically strengthened glass. It is semi-transparent for the employed laser with a wavelength λ=775 nm.

1.3 Objective

Using Gorilla Glass 2320 as the model material, the objectives of this investigation on femtosecond laser material-interactions can be summarised as:

1. To examine the appropriateness of the existing overall absorption coefficient equation, and if a new formulation and the associated analyses can be developed to address the shortcomings of the existing equation. The new formulation and analyses are to address the delineation and transition between purely linear absorption region and the nonlinear absorption dominated region.
2. To examine the validity and necessity of having Rayleigh length to classify if a sample is "thin" or "thick" in the analyses of the experimental results of the Z-scan technique, and the validity of the implicit assumption that the laser beam spatial distribution remain constant as it traverses a "thin" sample.
3. To investigate the effects of laser-induced plasma formation on absorption characterization during ultrashort pulsed laser irradiation.
4. To independent verify the determined absorption coefficients by correlating the experimentally measure temperature fields with the predicted temperature fields as a result of heat energy absorption obtained through the overall absorption coefficients.

1.4 Scopes

The scopes of the investigation are:

1. To determine the nonlinear absorption threshold intensity, the linear, nonlinear and overall absorption coefficients during femtosecond laser irradiation of glass using the Z-scan technique.
2. To examine the absorption characteristic of the sample in the Z-scan technique for the determination of the appropriateness of using the Rayleigh length to classify the sample thickness.
3. To observe the laser-induced plasma and to determine the plasma decay time and/or duration, and its effect on laser power absorption.
4. To simulate thermal heating during femtosecond laser irradiation through the use of the determined overall absorption coefficient.
5. To correlate the observed temperature field with the simulated temperature field for an independent verification of the determined linear, nonlinear and overall absorption coefficients and nonlinear absorption threshold intensity.

1.5 Organization of the thesis

- Chapter 1 introduces the overall structure of the thesis, with objectives and scopes of the investigation outlined.
- The fundamentals of the laser-material interaction are discussed in Chapter 2. Previous work on nonlinear absorption using ultrashort pulsed laser is reviewed. Limitations of the previous investigations are highlighted. Thermal

effects arising during the interaction of ultrashort pulsed laser with materials are reviewed.

- In Chapter 3, the research methodology is introduced. Experimental setup and experimental protocol adopted for the open aperture Z-scan experiment, plasma observation and the direct thermal observation during laser irradiation with an ultrashort pulsed laser are presented.
- Chapter 4 presents a new formulation for the overall absorption coefficient with the introduction of the nonlinear absorption threshold intensity. The mathematical model developed and the numerical procedures adopted to solve the mathematical model are described. The experimental absorption results are correlated with the simulated absorption results to determine the linear, nonlinear and overall coefficients of absorption and the nonlinear absorption threshold intensity. Simulated absorption power using the existing conventional formulation of the overall absorption coefficient is compared with the proposed overall absorption coefficient. The necessity and appropriateness on the classification of a sample as "thick" or "thin" based on the Rayleigh length for the Z-scan analysis are examined and discussed. The intensity decay of the laser beam within the material as a result of the nonlinear absorption is analyzed.
- In Chapter 5, direct observation of the laser-induced plasma is studied through high-speed imaging. The necessity of having an optical filter is discussed along with the criterion for the choice of the optical filter. An

attempt is made for the determination of the duration and/or decay time of the laser-induced plasma. The laser-induced plasma is observed at different z-locations in the Z-scan technique at different laser power levels.

- In Chapter 6, direct observation of the temperature field during femtosecond laser irradiation of glass is conducted. A mathematical model, using the proposed overall absorption coefficient and the nonlinear absorption threshold intensity, for the thermal heat transport is developed and solved using COMSOL Multiphysics. The observed and the simulated temperature fields are correlated to provide an independent verification and accuracy assessment on the determined values of coefficients of absorption and the nonlinear absorption threshold intensity.
- In Chapter 7, the conclusions reached are highlighted. Recommendations are provided for future work.

Chapter 2: Literature review

Laser is the abbreviation for 'Light amplification of stimulated emission of radiation'. Laser is a coherent beam of photons at a wavelength which can be optically focused. Laser has been used for cutting, drilling, welding, and modifications of materials [1], and the processing of polymers [2, 3], metal [4-6], and glasses [7, 8], etc.

Laser is an effective, versatile non-contact tool with small or negligible heat affected zones for material processing. As a result, laser machining is one of the widely used techniques for material processing. Different types of lasers are available for material processing. In terms of mode of operation, lasers can be classified as a continuous-wave (CW) lasers and a pulsed laser. In a CW operated laser, the laser is continuously pumped, and the output laser is also continuous. In contrast, in pulsed mode operation of laser, the output is a periodic pulse laser. Compared to CW laser, a pulsed laser can be used for precision machining. Undesirable effects like heat affected zone can be minimized, and sharp contours can be achieved with a short pulsed laser [8].

2.1 Short pulse laser

To understand how a pulsed laser can be classified as a short pulsed laser, it is essential to have knowledge on laser interaction. Basically, it consists of four processes (a) carrier excitation, (b) thermalization, (c) carrier removal and (d) thermal and structural effects [12]. Photon energy absorbed during laser irradiation will induce electronic non-equilibrium thermodynamic state. To regain

thermodynamic equilibrium, energy of electron transfers to either phonon or other electrons at a lower state. The process of an excited electron transfering excess energy to phonon or other electron is called thermalization [12]. The time in which thermalization occurs is the thermalization time. After thermalization, electron and lattice will be in the same temperature; nonetheless there will still be excess free electrons compared to the initial state of the material. These excess free electrons either diffuse out of the excited region or recombine with holes leading to carrier removal. Eventually, the thermal energy dissipates into the substrate through thermal and structural effects and changes. Carrier removal and the thermal and structural effects resulting in electron returning to its original energy state is called relaxation [12]. The time in which relaxation is realized is the relaxation time. Figure 2-1 shows the electron-phonon processes that occur after photon absorption with the timescale of each process completion in crystalline GaAs, amorphous GaAs and thin films amorphous GeSb [12].

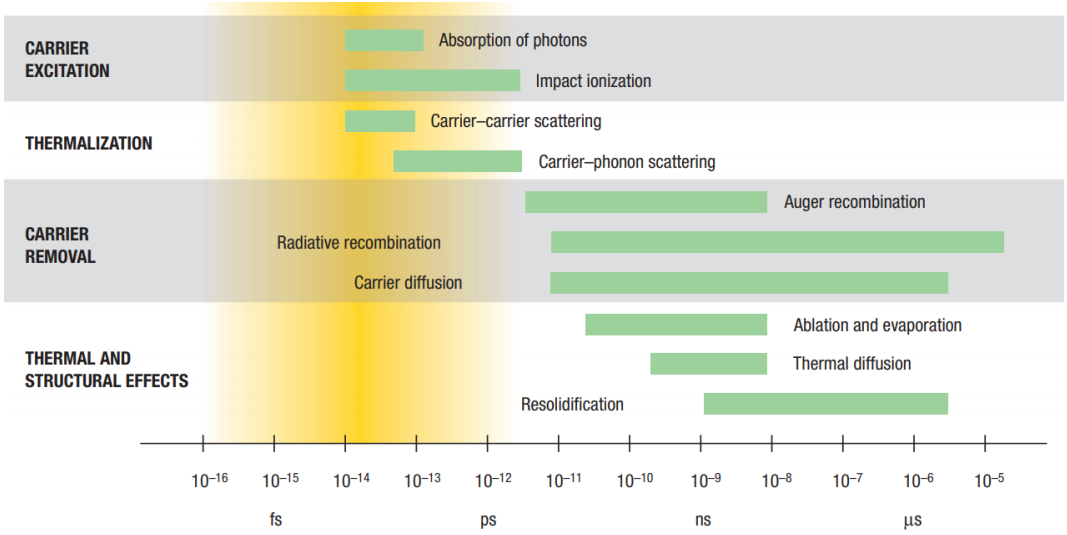

Figure 2-1: Timescale of various electron and lattice processes in semiconductor interaction, green bar shows characteristics time of each process [12]

With the distinction of thermalization time and relaxation time, laser can be classified in terms of laser pulse duration with respect to thermalization time. If the pulse of a laser is shorter than or comparable to the material thermalization time, the laser can be considered as a short pulsed laser for the material; otherwise the laser is considered as a long pulsed laser.

Figure 2-1 indicates that in general, the overall thermalization time is around 1 ps, carrier-carrier thermalization time is between ~10 fs to ~100 fs, and carrier-phonon scattering occurs within ~200 fs to ~1 ps. In this case, if the laser pulse duration is shorter than 1 ps then the laser is considered a short pulsed laser. Thus, in general, short pulsed lasers refer to a class of lasers whose pulse duration is less than a few picoseconds.

2.2 Absorption

Laser material interaction commences with the absorption of the irradiated photon by the target. The nature of interaction of the irradiated laser beam depends on the combination of laser parameters – wavelength, pulse duration, and intensity [80]. For laser wavelengths in infrared or visible spectrum, absorption mechanisms are different for metals, semiconductors and dielectric materials such as glasses or polymers [1]. The absorption can be either linear absorption or non-linear absorption. For optically opaque material, linear absorption occurs at long pulse and low power intensity. The absorption may shift to nonlinear absorption with a short and high intensity laser pulse. For optically transparent media, nonlinear absorption will be dominant through laser induced optical breakdown of material.

2.2.1 Linear absorption

As indicated earlier, linear absorption takes place for optically opaque material for long pulse (e.g. continuous wave lasers or for lasers with pulse width in nanometres range) and low power intensity lasers. The absorption takes place only when the photon energy is greater than or equal to the material's band gap given as [80]:

$$E_p \geq E_g \tag{2-1}$$

Where E_p is the energy of the photon and E_g is the band gap energy of the material. Band gap energy is defined as the difference in energy level between the valance band and the conduction band of a material. The energy of the photon is defined as [80]

$$E_p = hv \tag{2-2}$$

where *h* is the Planck constant (6.62606957×10^{-34} Js), and *v* the frequency.

The intensity of laser decays along the direction parallel to the laser beam axis. The decay rate is determined by the material's absorption coefficient *α. α* is a function of laser wavelength and substrate temperature. However, for an assumed constant value of α, the decay in intensity can be described by the Beer-Lambert Law [80]

$$I(z) = I_o e^{-\alpha z} \tag{2-3}$$

where *I(z)* is the laser intensity at depth *z, α* the absorption coefficient and I_o the incident intensity.

The optical penetration or absorption depth can be defined as [80]

$$\mathrm{d} = 1/\alpha \tag{2-4}$$

Which is the depth at which the intensity of the transmitted light drops to 1/e of its initial value at the interface.

2.2.2 Nonlinear absorption

Nonlinear optics is the study of modification in properties of the optical medium in the presence of light, which include the study of nonlinear absorption. The optical phenomenon that occurs at high intensity is "nonlinear" in the sense that material properties change nonlinearly with a change in intensity.

Normally in an optically transparent medium, in non-UV spectra, focused femtosecond laser pulses have low photon energy to be linearly absorbed [11]. In such a material, laser-induced breakdown must occur for absorption. Typically, the intensity of light must be sufficiently intense for an optical medium to undergo nonlinear changes. Table 2-1 shows the optical breakdown intensities for some given materials. It should be noted the threshold intensities for optical breakdown is in the range of 10^{13} W/cm^2.

Table 2-1: Threshold Intensities for optical breakdown [13]

Material	**Intensities (W/cm^2)**
Glass	$(2.8 \pm 0.4) \times 10^{13}$
Magnesium fluoride	$(1.5 \pm 0.4) \times 10^{13}$
Sapphire	$(1.3 \pm 0.4) \times 10^{13}$
Fused silica	$(1.0 \pm 0.4) \times 10^{13}$

This sufficiently high intensity for nonlinear interaction can be achieved typically only with a laser. Among lasers, during short-pulsed laser irradiation, the time of releasing the total pulse energy is short (less than few picoseconds); as a result, short-pulsed lasers have very high peak intensity. For example, a 1 kHz repetition rate Gaussian beam profile laser with 1.5 W average power output and pulse duration of 130 fs (FWHM) has a peak intensity of 3.3×10^{15} W/cm^2. Therefore, during short pulsed laser irradiation, nonlinear optical phenomenon is prominent. The laser-induced breakdown occurs by nonlinear absorption processes such as avalanche photoionization or avalanche ionization [11] .

Photoionization

Multiphoton ionization occurs by simultaneous absorption of multiple photons by an electron at the valance band [1, 11]. An optically transparent material can be directly ionized in a strong laser field by multiple photon absorption. The process is schematically shown in Figure 2-2(a).

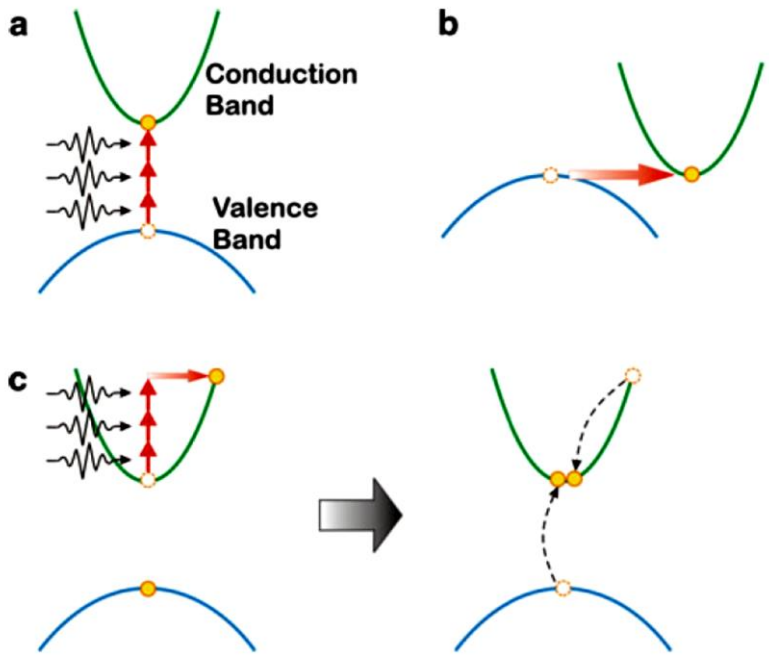

Figure 2-2 : Schematic diagram of (a) multiphoton ionization process ionizing by simultaneous absorption of m photons (b) tunnelling (c) avalanche ionization [11]

A valance electron with ionization potential or band gap energy (E_g) can be lifted to the conduction band absorbing 'm' photons of photon energy 'hf' such that [11]

$$mhf \geq E_g \tag{2-5}$$

Multiphoton ionization is significant in low laser intensities and high frequencies. In contrast, tunnelling is the cause of nonlinear absorption at high laser intensities and low frequencies [11]. Tunnelling effect is schematically shown in Figure 2-2(b). The strong laser field distorts the band structure of the material and reduces the band gap or potential barrier. In this case, quantum tunnelling takes place where direct transfer of electron from a valance band to a conduction band occurs. Multiphoton ionization and tunnelling ionization can be described by the Kedlysh parameter [11]:

$$\gamma' = \frac{\omega}{e}\sqrt{\frac{m_e c n \varepsilon_o E_g}{I}} \tag{2-6}$$

Where ω is the laser frequency, e the fundamental electron charge, m_e the effective mass of an electron, c the speed of light, n linear refractive index of media, ε_o absolute permittivity of free space and I the laser intensity at the focus. If γ' is much greater or less than 1.5, quantum tunnelling photoionization dominates. For γ' ~ 1.5, photoionization is the combination of multiphoton ionization and quantum tunnelling [11].

Avalanche Ionization

When linear absorption is not possible in an optically transparent medium, the valance band electron has band gap energy greater than the laser photon energy. In this case the valance band electron does not absorb the photon energy. However, in a real material, there are always some free electrons from metallic impurities, lattice imperfections (vacancies, interstitials) [81] , thermally excited impurities or other photoionization process. These free electrons or electrons in the conduction band are the seeds for avalanche ionization [1, 11]. The free electrons can absorb several laser photons. This absorption of energy will result in an increase in conduction band electrons' energy. The difference between the excited electron energy and the minimum energy state of the conduction band can be more than the band gap energy of an atom. In this case, the excited hot electron can impact with the electron in the valance band which can result in at least two electrons in the conduction band as shown in Figure 2-2(c). These electrons can further undergo sequential absorption of laser photon and cause further ionization. This process repeats itself until there is an avalanche of electrons where free electron density grows exponentially [1, 11]. When enough electrons are ionized, "critical density" plasma is formed. The plasma transforms the optically transparent material into an absorbing material.

Critical density of electron for nanosecond or longer pulse laser is in the range of 10^{18} cm^{-3}. For a shorter pulse duration laser, the critical plasma density for laser wavelength defined in *cgs* unit is given as [1]

$$n_c = \frac{m_e \omega^2}{4\pi e^2} \tag{2-7}$$

Where m_e is the mass of the electron and ω is the laser frequency. This is the critical density at which the plasma oscillation frequency equals to the laser frequency and the material becomes absorbing.

2.2.3 Summary

Any laser whose pulse width is less than the thermalization time can be considered as a short-pulsed laser for the material. When employing a short-pulsed laser, the laser power intensity is very high. The laser energy is absorbed by electron(s) in the material in time less than a few picoseconds, with insufficient time for thermalization. As a result, in addition to linear absorption, there will be nonlinear absorption of the laser power by the material. Therefore, not only non-transparent material, but also transparent materials can be processed using a short-pulsed laser.

2.3 Optical polarization

"Nonlinear optical phenomenon" is a rather broad term. Different nonlinear processes such as second harmonic generation, sum frequency generation, difference frequency mixing, optical rectification, single-photon nonlinear absorption, two-photon nonlinear absorption, self-phase modulation optical Kerr effect, cross-phase modulation optical Kerr effect and many other processes might occur during laser interaction. However, to better understand nonlinear absorption, it should be differentiated from other nonlinear processes.

2.3.1 Polarization formulation

For a better understanding of the nonlinear optical phenomenon, polarization $\tilde{\tilde{P}}^{(n)}(t)$of an optical medium for a given electric field $\tilde{\tilde{E}}(t)$ must be defined. The polarization of an optical medium is defined as the dipole moment per unit volume which is proportional to the strength of the incident electric field. The n-order polarization [82] can be defined as:

$$\tilde{\tilde{P}}^{(n)}(t) = \varepsilon_o \chi^{(n)} \tilde{\tilde{E}}(t) \tag{2-8}$$

where ε_o is the absolute permittivity of vacuum and $\chi^{(n)}$is a dimensionless proportionality constant known as n^{th}-order optical susceptibility. Optical susceptibilities are complex tensors that relate electric field's strength and frequency to strength and direction of induced polarization.

First order, second order, third order, and higher order nonlinear polarization can be defined in terms of higher order electric field as [82]:

$$\begin{aligned} \tilde{\tilde{P}}^{(1)}(t) &= \varepsilon_o \chi^{(1)} \tilde{\tilde{E}}(t) \\ \tilde{\tilde{P}}^{(2)}(t) &= \varepsilon_o \chi^{(2)} \tilde{\tilde{E}}^2(t) \\ \tilde{\tilde{P}}^{(3)}(t) &= \varepsilon_o \chi^{(3)} \tilde{\tilde{E}}^3(t) \\ &\vdots \end{aligned} \tag{2-9}$$

$\chi^{(n)}$ is n-order optical susceptibilities (n = 1, 2, 3, ...). The total polarization can thus be defined as the sum of all polarization orders as [82]:

$$\tilde{\tilde{P}}(t) = \tilde{\tilde{P}}^{(1)}(t) + \tilde{\tilde{P}}^{(2)}(t) + \tilde{\tilde{P}}^{(3)}(t) + \cdots \quad (2\text{-}10)$$

The total polarization can be defined in terms of electric field and optical susceptibilities by substituting equation (2-9) into equation (2-10) [82]:

$$\tilde{\tilde{P}}(t) = \varepsilon_o \left[\chi^{(1)} \tilde{\tilde{E}}(t) + \chi^{(2)} \tilde{\tilde{E}}^2(t) + \chi^{(3)} \tilde{\tilde{E}}^3(t) + \cdots \right] \quad (2\text{-}11)$$

2.3.2 Characteristics of n-th order polarization

The linear polarization $\tilde{\tilde{P}}^{(1)}(t)$ is responsible for the linear optical properties of the material, namely linear absorption and linear refraction [82]. Higher order polarizations are responsible for nonlinear optical properties. Distinct optical nonlinearities arise from different order polarization. For example, second order polarization is responsible for nonlinear properties like second harmonic generation, sum frequency generation, difference frequency mixing and optical rectification [16, 83]. For third order polarization, nonlinear processes including but not limited to single-photon nonlinear absorption, two-photon nonlinear absorption, self-phase modulation optical Kerr effect, and cross-phase modulation optical Kerr effect [83].

Polarization changes sign when the optical electric field is reversed. In a material with inversion symmetry, the polarization induced is equal but opposite as the electric field is reversed. As a result, the net polarization is zero. Therefore, second-order polarization cannot occur in materials with inversion symmetry [82]. In fact, in materials that shows inversion symmetry, all the even-ordered susceptibilities

vanish. The effect of polarization due to even-ordered polarization is nonexistent [82]. Therefore, in an isotropic medium such as glasses, the nonlinearity is caused by third order or odd higher-ordered polarization [84, 85]. As such, in this investigation on a chemically strengthened glass, second order polarization and other even-ordered polarization can be neglected. The lowest order nonlinear polarization that gives rise to nonlinearity in the glass is, therefore, the third order polarization.

Higher order nonlinear processes can be addressed as the cascade process of lower order nonlinear processes [86]. Cascading of third-order susceptibilities $\chi^{(3)}$: $\chi^{(3)}$ has been reported to act as effective fifth-order susceptibility [87]. As the cascade process of lower order suceptitibilites can be effectively act as higher order suceptibilites, higher order polorization may be neglected. As such, only first-order polarization and third-order polarization will be considered in this investigation. By ignoring even-ordered suceptibilities and cascading higher-order odd-ordered suceptibilites, the polarization equation can be written as:

$$\tilde{\tilde{P}}(t) = \varepsilon_o \left[\chi^{(1)}\tilde{\tilde{E}}(t) + \chi^{(3)}\tilde{\tilde{E}}^3(t)\right] \tag{2-12}$$

2.3.3 Absorption and refraction with respect to polarizaiton

First-order polarization would give rise to linear optical properties and third-order polarization would be responsible for higher order or nonlinear optical properties. It has been described earlier that susceptibilities are complex tensors. The real part of susceptibilities is proportional to the refractive index whereas the imaginary part of

susceptibilities is proportional to the absorption coefficient. When only first-order susceptibilities and third-order susceptibilities are considered, the overall refractive index *n* and overall absorption coefficient $\boldsymbol{\alpha}$ (already discussed in Chapter 1, equation (1-1)) can be written as [15, 84, 85]:

$$n(I) = n_o + \gamma I \tag{2-13}$$

$$\alpha(I) = \alpha + \beta I \tag{1-1}$$

where n_o and α_o are linear refractive index and linear absorption coefficient respectively arising from first-ordered polarization; n_1 and α_1 are nonlinear refractive index and nonlinear absorption coefficient respectively arising from third order polarization; I is irradiated laser intensity. The nonlinear refractive index n_1 and nonlinear absorption coefficient α_1 can be described in terms of third-order susceptibilities $\chi^{(3)}$ as [15, 85]:

$$\gamma = \frac{3\ Re\left[\chi^{(3)}\right]}{4\varepsilon_o c n_o^2} \tag{2-14}$$

$$\beta = \frac{3\ \omega\ Im\left[\chi^{(3)}\right]}{2\varepsilon_o c^2 n_o^2} \tag{2-15}$$

Where $\boldsymbol{\omega}$ and $\boldsymbol{c}$ are the laser frequency and the speed of light respectively.

2.4 Nonlinear optical characterization techniques

Many optical characterization techniques have been studied over the years for optical material characterization. Different techniques have been developed for different material. In this section, some of the common nonlinear optical characterization techniques will be reviewed.

2.4.1 Optical Kerr gate technique

Kerr effect is the change in optical refractive index in the presence of an electrical field. Kerr effect is responsible for nonlinear optical effects like self-focusing and self-phase modulation. Indeed, the study of nonlinearity in a material started when Kerr-effect was recognized in 1969 AD [88]. Optical Kerr effects has been studied in liquids [89, 90] , glasses [91] and semiconductors [92]. However, using Kerr gating technique for the measurement of nonlinearity, the background signal/noise is large for long-lived samples [93], which usually is the case.

2.4.2 Wave-mixing technique

Forward four-wave mixing (FWM) technique is the most common form of wave-mixing technique employed for nonlinear optical characterization. In FWM, lights of three frequencies f_1, f_2 and f_3 are incident on the target material. These three frequencies interact in a nonlinear medium to produce a new wavelength of light at frequency f_4 [94]. Two common forms of FWM are sum and different frequency generation. In sum frequency generation, the three fields are input and the output is a new high frequency field at the sum of the three input frequencies. In difference frequency generation, the typical output is the sum of two minus the third.

FWM has been used as the main technique for the characterization of an optical medium [82, 95]. FWM can be used for the characterization of any media from gases, liquids and solids [82]. Semiconductors nonlinear properties are mostly studied using FWM [96, 97]. However, in the already complicated experimental setup while using FWM technique, the experimentation requires highly stable laser beam intensity for the proper characterization of an optical material. This is the major disadvantage of the FWM technique [98].

2.4.3 Z-scan technique

The Z-scan technique is performed by inserting a sample and translating it along the direction of laser propagation and through the laser's focal plane. The Z-scan involves tightly focusing a single Gaussian laser beam into a thin sample [15]. The transmittance changes are observed in the far-field. In the far-field, the diffraction pattern as a result of nonlinear interaction is measured with/without an aperture. The result is a characteristic peak and valley as the sample is scanned through the beam waist. Through analysis of these characteristic peak and valley, the nonlinear coefficients can be determined. Since the first formulation of the Z-scan technique in 1990 [14, 15], many variations [18, 38, 41, 44] of the Z-scan technique have been developed.

2.5 Z-scan technique

First described in 1989 by Mansoor Sheik-Bahae et al. [14, 15], the Z-scan technique allowed the direct measurement of nonlinear refraction and nonlinear absorption. As indicated in the previous section, the Z-scan technique is conducted by inserting and translating the sample along the direction of laser propagation and through the laser's focal plane.

2.5.1 Original Z-scan technique

The Z-scan technique proposed by Mansoor Sheik-Bahae et al. [14, 15] was based on spatial beam distortion as a result of optical nonlinearities as the beam propagates through a material. A single Gaussian laser beam in a tightly focus geometry was used. The transmitted laser beam power through a nonlinear medium was measured with or without a finite aperture in the far-field. With a use of a finite aperture the coefficient of nonlinear refraction could be inferred by plotting the transmitted power as a function of sample position with respect to the focus plane. The Z-scan experiment using a finite aperture is called the "closed aperture" Z-scan technique. In contrast, in the absence of an aperture, the coefficient of nonlinear absorption could be inferred by plotting the transmitted power as a function of the sample position. The Z-scan experiment without the use of aperture is called the "open aperture" Z-scan technique.

2.5.1.1 Closed aperture Z-scan technique

Figure 2-3 shows the schematic diagram of a closed aperture Z-scan technique for the determination of nonlinear refraction.

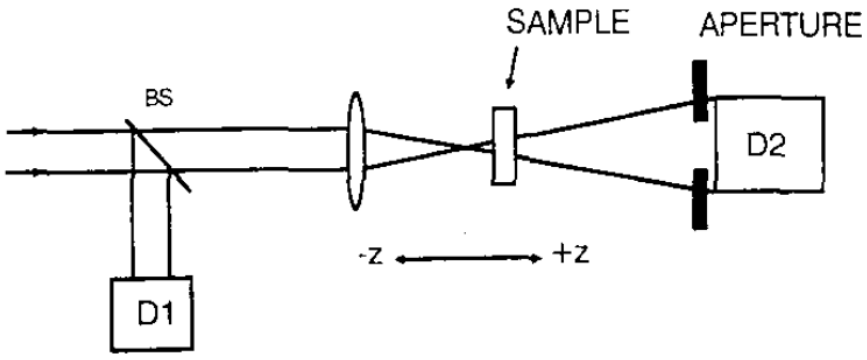

Figure 2-3 : Schematic Z-scan setup in which normalized transmission (ratio of power detected by detector D2 to power detected by reference detector D1) is recorded as function of sample position z [15].

Mansoor Sheik-Bahae et al. [15] explains the technique by assuming a material with a negative nonlinear refractive index for a thin sample. A thin sample infers that the sample thickness is less than the diffraction length of the focused beam which will act as a lens with variable focal length. It should be noted that in Figure 2-3, the power detected by D2 is going through an aperture. As the Z-scan is initiated with sample far away from the focal plane (negative z), the intensity of the beam is low with small refractive index; there is negligible change in the normalized transmittance (D2/D1). However, as the sample approaches the focal plane, the beam intensity increases leading to self-focusing in the sample. A negative self-lensing prior to focus will collimate the beam. This causes a beam narrowing at the aperture resulting in an increase in the measured transmittance at D2, and thus an increase in the normalized transmission. As the scan in z continues, the sample translates past

the focal plane to the right (positive z). The same self-defocusing increases the beam divergence, leading to beam broadening at the aperture, and thus a decrease in transmittance. This technique of using an aperture to restrict the amount of power reaching D2 in Figure 2-3 based on collimating or diverging of beam is called the "closed aperture" Z-scan technique. This technique is employed for the determination of nonlinear refractive index. Figure 2-4(a) shows a normalized transmission as a function of z-position in the "closed" aperture Z-scan technique.

2.5.1.2 Open aperture Z-scan technique

For the determination of nonlinear absorption coefficient, the same experimental setup is used but with a wide-open aperture (see Figure 2-3). This arrangement allows all the transmitted laser power to be detected by detector D2 irrespective of the changes caused by nonlinear refraction. As such, changes detected in detector D2 will account for changes due to nonlinear absorption only. The experimental setup for the determination of nonlinear absorption is termed as the "open aperture" Z-scan technique. Figure 2-4(b) shows a normalized transmission as a function of z-position in the "open" aperture Z-scan technique.

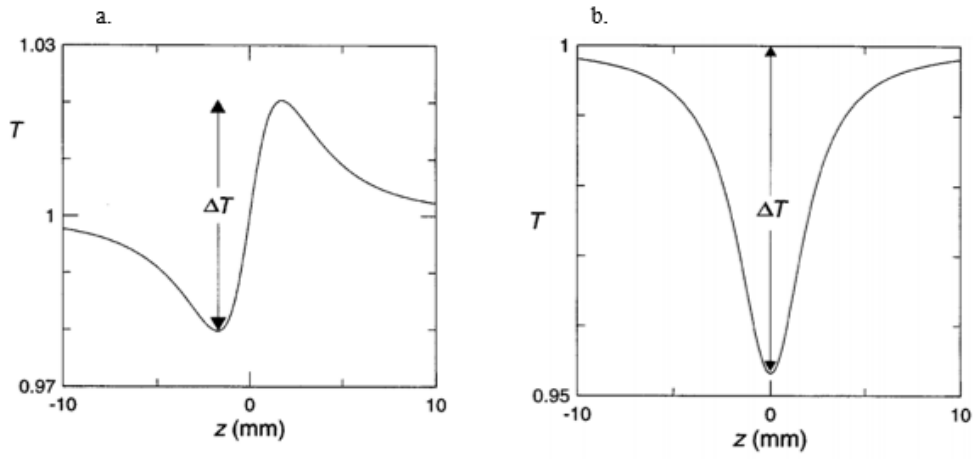

Figure 2-4: (a) Normalized transmission as a function of z-position in closed aperture Z-scan technique, (b) Normalized transmission as a function of z-position in open aperture Z-scan technique [42]

2.5.1.3 Z-scan formulation

As indicated earlier in section 3.3.3 (above), the coefficients of nonlinear absorption and nonlinear refraction are represented in [15] as mentioned earlier in equation (2-13) and equation (1-1) as:

$$n(I) = n_o + \gamma I \tag{2-13}$$

$$\alpha(I) = \alpha + \beta I \tag{1-1}$$

Where *n(I)* and *α(I)* are the refraction coefficient and overall absorption coefficient respectively, with n_o and γ the linear and nonlinear coefficient of refraction

respectively, and α and β the linear absorption coefficient and nonlinear absorption coefficient respectively. *I* is the intensity of radiated laser energy.

Slow varying envelop approximation was employed by Mansoor Sheik-Bahae et al. [15] to define the governing equation for the change in intensity (*I)* and the change in phase shift ($\Delta\phi$) as:

$$\frac{d\Delta\phi}{dz'} = \Delta n(I)k \tag{2-16}$$

$$\frac{dI}{dz'} = -\alpha(I)I \tag{2-17}$$

Where $k = 2\pi/\lambda$ is the wave vector, and $\Delta n(I)$ and $\alpha(I)$ are the overall refractive index and overall absorption coefficient respectively.

Equation (2-16) and equation (2-17) were solved for the case of cubic nonlinearity and negligible nonlinear absorption to obtain the phase shift at the exit surface as [15]

$$\Delta\phi(z,r,t) = \Delta\phi_o(z,t)\ exp\left(-\frac{2r^2}{w^2(z)}\right) \tag{2-18}$$

With,

$$\Delta\phi_o(z,t) = \frac{\Delta\Phi(t)}{1+\frac{z^2}{z_o^2}} \tag{2-19}$$

Here, $z_o = kw_o{}^2/2$ is the Rayleigh length of a laser beam with w_o as the beam diameter at the focal plane, and $\Delta\Phi(t)$ is the on-axis phase shift at the focal plane defined as [15]

$$\Delta\Phi(t) = k\Delta n_o(t)L_{eff} \tag{2-20}$$

Where $L_{eff} = (1 - e^{-\alpha L})/\alpha$ is the effective length with L as the sample length, and α the linear absorption coefficient. $\Delta n_o(t) = \gamma I_o(t)$ is the change in overall nonlinear refractive index at any given time t with $I_o(t)$ being the on-axis focal irradiance.

With the determination of phase shift, the normalized transmission power was calculated as [15]:

$$T(z) = \frac{\int_{-\infty}^{\infty} P_T(\Delta\phi_o(t))\,dt}{S\int_{-\infty}^{\infty} P_i(t)dt} \tag{2-21}$$

Where $P_T\big(\Delta\phi_o(t)\big)$ is the instantaneous power transmitted through the aperture, $S = 1 - \exp\left(-\frac{2r_a^2}{w_a^2}\right)$ is the aperture linear transmittance with r_a and w_a the radius of aperture and beam diameter at the aperture respectively. $P_i(t) = \pi\omega_o^2 I_o(t)/2$ is the instantaneous power input within the sample.

For an aperture linear transmittance of 0.01, the normalized transmission in the far-field is shown in Figure 2-5 with a constant on-axis phase shift with respect to time. It has been noted [15] that the valley-peak was as expected for positive nonlinearity

and peak-valley for negative nonlinearity. The magnitude of normalized transmittance does not depend on the wavelength or geometry [15].

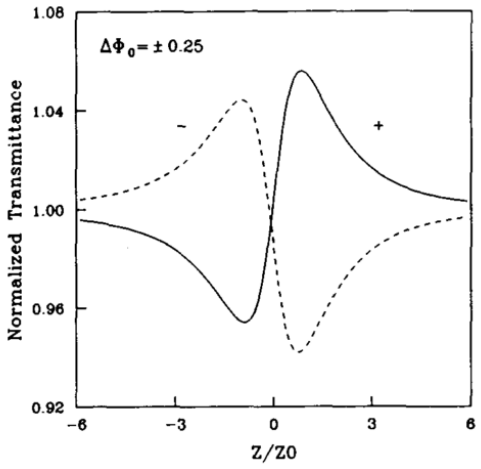

Figure 2-5: Calculated normalized transmission with on-axis phase shift of ± 0.25 with small aperture of S=0.01 as a function of z-position in term of unit Rayleigh Length, z_o [15].

For the calculation of nonlinear absorption with the "open" aperture Z-scan technique, equation (2-16) and equation (2-17) were solved with free-carrier effects (refractive and absorptive) neglected for obtaining the irradiance and phase shift at the exit surface as [15]:

$$I_e(z,r,t) = \frac{I(z,r,t)\exp(-\alpha L)}{1+q(z,r,t)} \tag{2-22}$$

$$\Delta\emptyset(z,r,t) = \frac{k\gamma}{\beta} ln[1+q(z,r,t)] \tag{2-23}$$

where $q(z,r,t) = \beta I(z,r,t) L_{eff}$. Again, β is the nonlinear absorption coefficient, γ is the nonlinear refractive coefficient, and $k = \frac{2\pi}{\lambda}$ is the wave vector. The normalized transmitted power was then calculated with open aperture i.e. *S=1*, as [15]:

$$T(z,S=1) = \frac{1}{\sqrt{\pi} q_o(z,o)} \int_{-\infty}^{\infty} \ln\left[1+q_o(z,0)\exp(-\tau^2)\right] d\tau \tag{2-24}$$

Nonlinear absorptive coefficient can be easily deduced from the normalized transmittance energy in an open aperture configuration because the system is insensitive to phase change [15] . Knowing the nonlinear absorption coefficient, the nonlinear refractive coefficient can be then calculated [15]. Figure 2-6 shows the normalized transmittance of ZnSe using laser central wavelength of λ=*532* nm in an open aperture configuration.

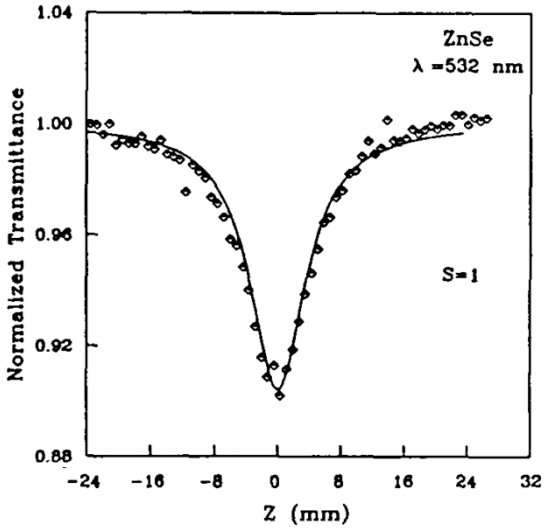

Figure 2-6: Normalized Z-scan transmittance of ZnSe measured using picosecond laser pulse at $\lambda=532$ nm with open aperture i.e. $S=1$, solid line represent the theoretical analysis, dots are experimentally obtained results [15]

Mansoor Sheik-Bahae et al. [15] used 2.7 mm thickness ZnSe for experimental verification. A frequency doubled Nd-YAG laser with a pulse duration of 27 ps (FWHM) at 532 nm had been employed. The diffraction length ($n_o z_o$) was reported to be approximately four times the sample thickness. As such, the thin sample approximation is applicable for their analysis. Using the technique developed, the nonlinear absorption coefficient for ZnSe was determined to be 5.8×10^{-9} cm/W and the nonlinear refractive index was determined to be 6.8×10^{-5} cm^2/GW. The technique is sensitive to less than $\lambda/300$ nonlinearity induced phase distortion [15].

2.5.1.4 Variations of Z-scan technique

Many variations of the Z-scan technique have been studied subsequently. Some of the variations of the original single Gaussian beam Z-scan technique include Elliptic Z-scan (EZ-scan) [40], Z-scan using a top-hat beam [18] instead of Gaussian beam, two colour single beam Z-scan technique [44], reflection Z-scan for measurement of surface optical properties [43] and eclipsed Z-scan technique [45].

The Z-scan technique has been employed to study the nonlinearity of different materials. Nonlinear optical characterization of liquids [17-20], polymers [21-25], glasses[26-30], semiconductors [31-34] and organic materials [35-37] have been studied using the single beam Z-scan technique or its variation.

Qi et al. [45] studied the nonlinear refractive index of methanol and ethanol using single beam time-resolved eclipsed Z-scan technique. A Ti-sapphire laser with central wavelength at 785 nm, average power of 605 mW, pulse duration of 150 fs (FWHM) and 76 MHz repetition rate was employed for the experiment. The aperture linear transmission (S) of 0.92 was used for the experiment. The measured nonlinear refractive index for methanol and ethanol were reported to be 2.04×10^{-16} cm^2/W and 1.72×10^{-16} cm^2/W respectively. However, the nonlinear absorption coefficient for ethanol and methanol has not been reported.

Cassano et al. [24] investigated third order nonlinear optical properties for three alkoxy-substituted poly(p-phenylenevinylene) (PPV), namely: poly[2,5-bis(2-methylbutoxy)-1,4-phenylenevinylene] (DMB-PPV), poly[2,5-bis(octyloxy)-1,4-

phenylenevinylene] (DOO-PPV) and poly[2,15-dioxabicyclo[14.2.2]icosa-1(19),16(20),17-trien-17,19-ylenevinylene] (bridged dialkoxy (BDA)-PPV)). A single beam Z-scan experiment was performed using Q-switched, mode-locked Nd3+:YAG (yttrium aluminium garnet) laser with central wavelength at 1064 nm, pulse energy 20 mJ, pulse duration of 35 fs (FWHM) and 10 Hz repetition rate. Table 2-2 summarizes the observed nonlinear refraction coefficient (n_2) and nonlinear absorption coefficient (α_2).

Table 2-2: Nonlinear coefficients value for different alkoxy-substituted PPV [24]

Sample	n_2 **(10^{-12} cm^2/W)**	α_2 **(10^{-9} cm/W)**
DMB-PPV	−4 ± 1	35.5 ± 9
DOO-PPV	−0.8 ± 0.2	14 ± 3
BDA-PPV	− 0.4 ± 0.1	9 ± 2

Smektala et al. [27] investigated the nonlinear properties of chalcogenide glasses. Binary glasses in the [Ge–Se] system, As_2S_3 and As_2Se_3 glasses, as well as ternary glasses in the [Ge–Se–As] system were characterized using the Z-scan technique. A Q-switched mode-locked Nd-Yag laser with central wavelength at 1064 nm, average power between 1 μW to 100 μW, pulse duration of 45 ps (FWHM) and 10 Hz repetition rate was employed for the experiment. Table 2-3 summarizes the observed nonlinear refraction coefficient (n_2) and nonlinear absorption coefficient (α_2) for different chalcogenide glasses.

Table 2-3: Nonlinear coefficients value for different chalcogenide glasses [27]

Sample	n_2 **(10^{-18} m^2/W)**	α_2 **(10^{-9} cm/W)**
$Ge_{10}Se_{90}$	15	1.8
$Ge_{20}Se_{80}$	13	1.8
$Ge_{30}Se_{70}$	21	1.1
$Ge_{10}As_{10}Se_{80}$	22	2.7
$Ge_{10}As_{20}Se_{70}$	14	3.1
$Ge_{15}As_{10}Se_{75}$	12	2.6

Although Z-scan is a highly effective and efficient technique for measuring the nonlinearities of materials, it is not without any limitations. Experimental conditions must be controlled carefully otherwise the observed results may not represent the true nonlinearity of material [42]. As the Z-scan technique relies on analysing a laser beam's far field distortion, it is particularly important to know the laser beam profile. Without a proper knowledge of the beam profile, the observed results will not be accurate [42]. Another important factor to consider for a proper study of the nonlinearities of material is sample thickness. In general, thin sample is employed with sample thickness less than the Rayleigh length, z_R [42]. Sample properties, namely, imperfections in sample and sample surface roughness also affect the Z-scan observation. A rough sample or imperfection in the sample diverging or reflecting the incoming laser beam will contribute to error in the observed transmission. This might lead to misleading values of optical nonlinearities [42]. Other factors that influences the result of the Z-scan technique include aperture size and aperture alignment [42], which affect only the nonlinear refractive index studies. Aperture

size influences the sensitivity in the observed far-field transmission. Therefore, pin-hole approximation of aperture (*S=0.01*, i.e. 1% linear transmittance) is advisable for good correlation between numerical and analytical results of the observed transmission. Aperture alignment is also important for the study of nonlinear refractive index as Gaussian beam approximation is used for single beam Z-scan measurement. The beam concentration is high at the axis of transmission; therefore, a misaligned aperture would again give false reading. To properly align the aperture, pinhole aperture is translated in x and y direction in low irradiance regime (i.e. linear regime or far from the tight focus) to obtain a maximum signal at the detector [42]. Limitations pertaining to laser beam profile, aperture size and aperture alignment have been mitigated through proper planning of an experiment. Careful consideration has been given on choosing sample thickness. In the literature, it can be observed that most of the analyses conducted is limited to thin sample approximation [14, 15, 19, 20, 22-24, 27-29, 33, 42, 44, 71]. The Z-scan analysis for thin media is based on the theory developed by Mansoor Sheik-Bahae et al. [14, 15]. Hitherto, all the examples discussed are based on thin sample analysis. There are different theoretical and experimental analyses conducted for thick samples [39, 46, 72-74].

Chapple et al. [39] performed the Z-scan studies on carbon disulphide (CS_2) using a Nd:YAG laser with 6.5 ns pulse duration on different sample thickness. The aperture linear transmission of 0.013 was used. Figure 2-7 shows the theoretical curves obtained from the numerical calculations correlated with the Z-scan observations.

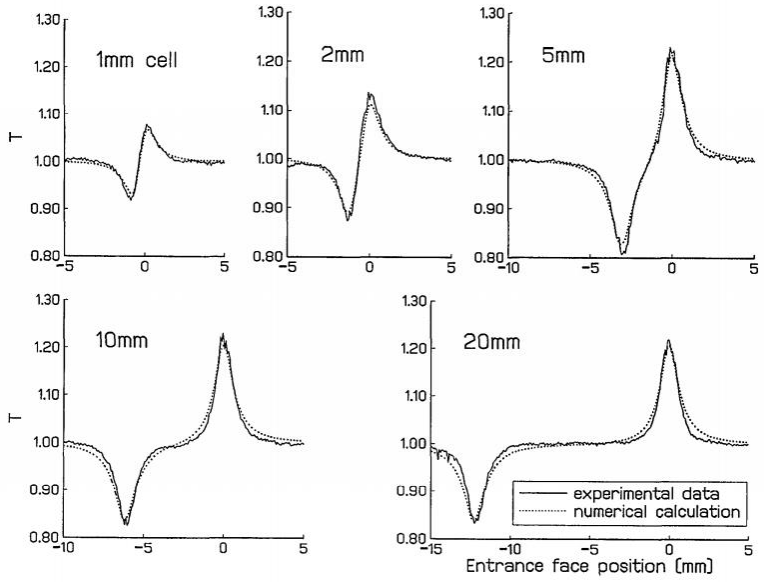

Figure 2-7 : Z-scan for different sample thickness of CS_2, fitted with theoretical curve from the numerical solution [39]

The theoretical curves obtained through numerical calculation were obtained through least-squares fitting of Z-scan data with β as independent variable. β is defined through an expression that relates to the difference between the maximum and the minimum normalized transmission ΔT given as [39]

$$\Delta T = 0.203|\beta|\frac{l}{n_o z_r} \tag{2-25}$$

Where

$$\beta = 2k\gamma I_o z_r n_o^2 \tag{2-26}$$

I_o is the on-axis laser power irradiation at the focal plane, l is the sample length, n_o is the linear refractive index, $k = \frac{2\pi}{\lambda}$ is vacuum wave number, γ relates to nonlinear refractive index and z_r is the Rayleigh length of the beam.

In [39] the normalized transmission $T(\beta,z)$ was defined as a third-order polynomial in β

$$T(\beta, z) = 1 + P_1(z)\beta + P_2(z)\beta^2 + P_3(z)\beta^3 \qquad (2\text{-}27)$$

Where $P_n(z)$ are the coefficients calculated through a least-square fitting with the observed Z-scan.

A modified normalized transmission $T^*(\beta,z)$ was also defiened to account for the different levels of power used (i.e. low, medium and high) during data acquition. This was carried out by multiplying the polynomilal coefficient in equation (2-27) by $(1 - r^n)$, such that [39]

$$T^*(\beta, z) = 1 + P_1(z)(1 - r)\beta + P_2(z)(1 - r^2)\beta^2 + P_3(z)(1 - r^3)\beta^3 \qquad (2\text{-}28)$$

Using equation (2-27) and equation (2-28), the effective normalized transmission was obtained as [39]

$$\overline{T^*}(\beta_o, z) = \frac{\int T^*(\beta_o, z)\beta(t)dt}{\int \beta(t)dt}$$

$$\overline{T^*}(\beta_o, z) = 1 + P_1(z)(1-r)\frac{\beta_o}{\sqrt{2}} + P_2(z)(1-r^2)\frac{{\beta_o}^2}{\sqrt{3}} + P_3(z)(1-r^3)\frac{{\beta_o}^3}{2} \quad (2\text{-}29)$$

Where

$$\beta(t) = \beta_o exp\left(-\frac{t^2}{\tau^2}\right) \quad (2\text{-}30)$$

β_o is the value of β at the peak irradiance and τ is the pulse duration.

Table 2-4 shows the values of nonlinear refractive index calculated through the method of least-square fitting and that calculated through the analytical theory method defined in [73]. Chapple et al. [39] concluded that the difference between the maximum and minimum normalized transmission can be significantly increase by increasing the effective sample length beyond the effective length as described by Mansoor Sheik-Bahae et al. [15] as $l_{eff} = 3.1\, n_o z_r$.

Table 2-4: Values of γ calculated through the least-square fitting method and through analytical theory [39]

Sample length(mm)	**Peak Irradiance (10^{12} W/m^2)**			**γ (10^{-18} m^2/W) [Equation (2-29)]**	**γ (10^{-18} m^2/W) [Analytical Theory]**
	High	**Medium**	**Low**		
20	9.9	-	1.7	3.42	3.75
20	-	4.0	1.7	3.47	3.63
10	10.2	-	1.8	3.60	3.92
10	-	4.0	1.8	3.43	3.59
5	11.3	-	1.8	3.63	4.11
5	-	4.1	1.8	3.66	3.88
2	9.7	-	2.2	3.89	4.28
1	9.4	-	1.7	3.67	3.87
Average				3.60	3.88

Zang et al. [46] presented a theoretical analysis for thick material. In the analysis, a thick medium with nonlinear absorption and nonlinear refraction is analysed using a Gaussian decomposition method treating the medium as a distributed lens model for a Gaussian beam. In their analysis, the coupling of nonlinear refraction and nonlinear absorption is accounted for.

Zang et al. [46] consider a thick medium as a stack of multi-layers thin material. They start with the normalized transmittance for thin film with a small on-axis shift, in the absence of absorption as defined in [14], to get the normalized transmittance for a thick nonlinear material as:

$$T = \prod_{i\approx 1}^{n}\left[1 + \frac{4\Delta\emptyset_{oi}x_i}{(x_i^2+1)(x_i^2+9)}\right] \cong exp\left[\sum_{i=1}^{n}\frac{4\Delta\emptyset_{oi}x_i}{(x_i^2+1)(x_i^2+9)}\right] \tag{2-31}$$

Where $\Delta\emptyset_{oi} = k\Delta n_o(t)L_i = \Delta\emptyset_R(t)\Delta x_i$, $\Delta\emptyset_R(t) = k\Delta n_o(t)z_o$ with L_i being the thickness of the i_{th} layer and, k and $\Delta n_o(t)$ are vacuum wave number and instantaneous on-axis change in refractive index. Also is $x_i = z_i/z_o$ with z_o as Rayleigh length of Laser beam and z_i the z-position of the i_{th} layer. With limit $n \to \infty$, the thickness of the i_{th} layer, $L_i \to 0$; the normalized transmission in equation (2-31) then takes the form [46]:

$$T = \left\{\frac{[(x+l)^2+1]\times(x^2+9)}{[(x+l)^2+9]\times(x^2+1)}\right\}^{\Delta\varphi_R(t)/4} \tag{2-32}$$

Here $l = L/z_o$ and L is the thickness of the medium.

For higher power regime, an approximate correlation factor, $C_\emptyset(t)$, was introduced [46]:

$$C_\emptyset(t) \cong \Delta\emptyset_R(t) + \tanh\left(\frac{l}{3}\right) \times \left[\frac{[\Delta\emptyset_R(t)]^2}{4} + \frac{[\Delta\emptyset_R(t)]^3}{16}\right] \tag{2-33}$$

To include the correlation factor in the higher power regime, the normalized transmission could be then written by substituting $\Delta\emptyset_{\boldsymbol{R}}(t)$ in equation (2-32) as

$$T = \left\{\frac{[(x+l)^2+1]\times(x^2+9)}{[(x+l)^2+9]\times(x^2+1)}\right\}^{C_\emptyset(t)/4} \tag{2-34}$$

Equation (2-34) represents the transmittance with a purely non-absorptive medium during closed aperture Z-scan measurements.

In a similar fashion, by considering a thick material as a stacked of multi-layers of thin material, the normalized transmittance in the presence of nonlinear absorption was calculated in [46] as:

$$T' = \frac{1}{1+\frac{1}{2}C_q(t)[\tan^{-1}(x+1)-\tan^{-1}(x)]} \tag{2-35}$$

Here $C_q(t)$ is a new correlation function given as [46]:

$$C_q(t) \cong Q_R(t) \times \left(1 + \tanh\left(\frac{l}{2}\right) \times \left\{\frac{3\Delta\emptyset_R(t)}{10} + \frac{[\Delta\emptyset_R(t)]^2}{8}\right\}\right) \quad (2\text{-}36)$$

Where $Q_R(t) = \beta I_o(t) z_o$, β being the two-photon absorption coefficient.

With the determination of the far field transmittance for a purely refractive medium (represented by equation (2-34)) and a purely absorptive medium (represented by equation (2-35)

, the far-field transmittance when nonlinear absorption and nonlinear refraction are present simultaneously can then be written as [46]

$$\hat{T} = T \times T' \quad (2\text{-}37)$$

Figure 2-8 shows the numerical and analytical solutions for the method developed by Zang et al. [46]. They also compared their investigation with other analyses of thick material [72, 73] of closed aperture Z-scan, see Figure 2-8. It has to be highlighted here that they only conducted the theoretical analysis without any experimental analysis and validation. During the formulation, the thick sample is considered as a stack of thin samples, however, the coupling of the nonlinearities between the sample is neglected. As such, although not specified explicitly, the evolution of the laser beam profile due to nonlinear absorption as the laser beam passes through the material is not accounted, thus, inherently assuming the beam profile remains intact as the beam propagates through different layers.

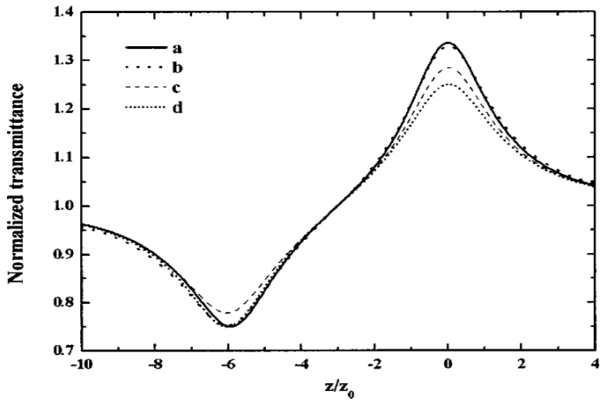

Figure 2-8 : Closed-aperture z-scan curve, with nonlinear phase shift $\Delta\emptyset_R = 0.5$ and sample length $l = \frac{L}{z_o} = 6$: (a) numerical solution [46] , (b) analytical solution [46], (c) analytical solution [72] (d) analytic solution [73]

Wang et al. [74] investigated the nonlinear absorption of thick (1.2 mm) polystyrene (PS) samples. Similar approach, as adopted by Zang et al. [46], of treating a thick sample as a stack of thin sample was adopted. A Ti-sapphire laser with central wavelength at 795 nm, pulse duration of 130 fs (FWHM) and 1000 Hz repetition rate was employed for the experiment. With beam waist diameter of 30 μm, the Rayleigh length z_o, was calculated to be 0.889 mm; effectively making a 1.2 mm PS sample a thick sample. Linear photon absorption spectra of PS is shown in Figure 2-9 [74]. With linear absorption at 795 nm wavelength negligible as shown in Figure 2-9, coefficient of linear absorption was considered negligible $(\alpha = 0)$. As such, only nonlinear absorption coefficient was considered for the analysis of the nonlinearity in a thick PS medium.

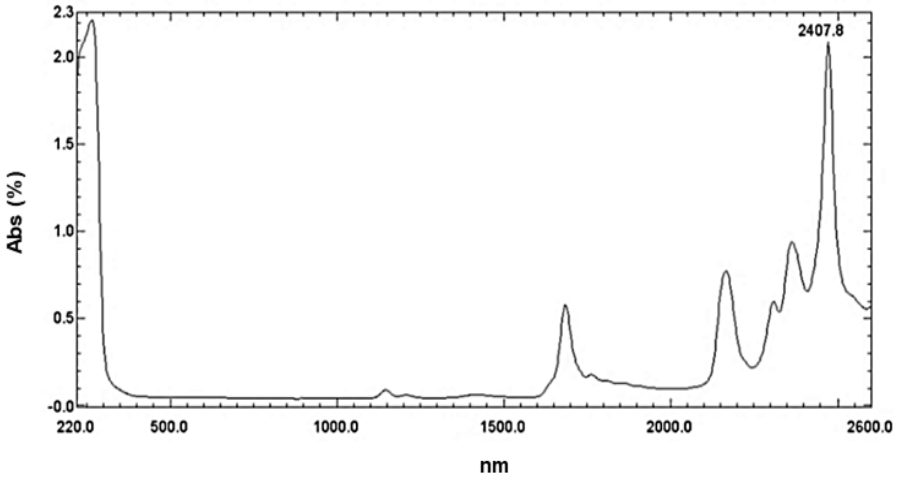

Figure 2-9: Linear photon absorption spectra of PS [74].

Different average power of 5.2 mW, 10.4 mW, 14.4 mW and 23.5 mW were used for the investigation of nonlinear absorption coefficient. The coefficient of nonlinear absorption for polystyrene was determined to be 0.000695 m/W with a standard deviation of 0.000026 m/W. Figure 2-10 shows the experimental data and theoretically analysed normalized transmittance curve for open aperture Z-scan technique using different power levels [74]. Similar to the work presented by Zang et al. [46], the evolution of the laser beam profile as it propagates through the material has not been considered.

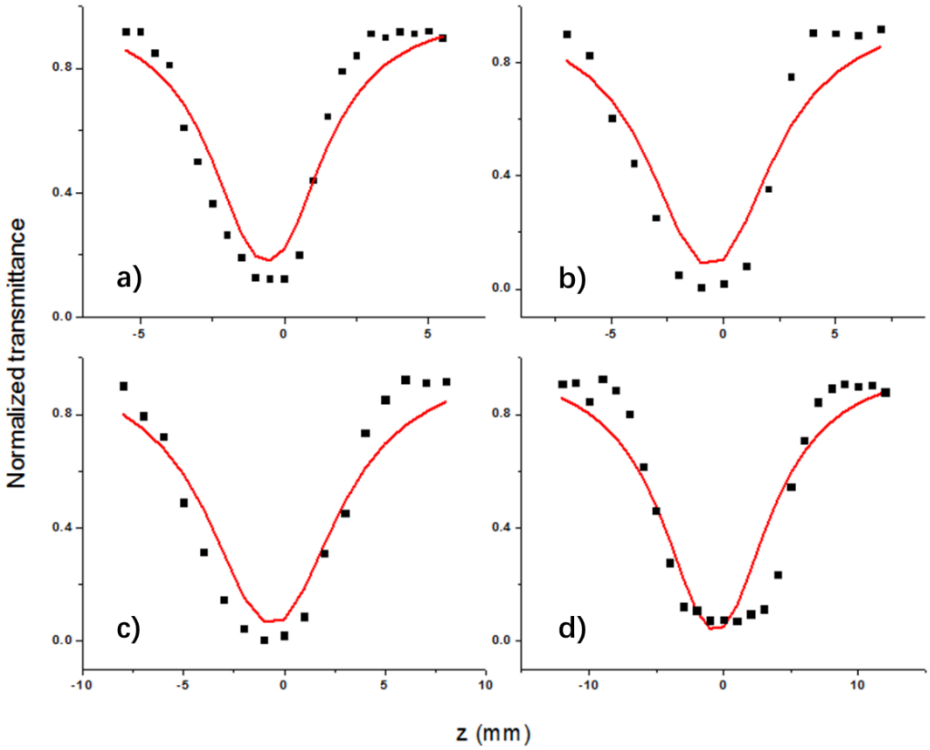

Figure 2-10: Normalized transmittance curve for open aperture z-scan technique with power at (a) 5.2 mW, (b) 10.4 mW, (c) 14.4 mW and (d) 23.5 mW [74] (black dots are experimental data and red line is theoretically analysed curve)

2.5.2 Unresolved issues in nonlinear absorption and Z-scan technique

Since the pioneering work proposed by Mansoor Sheik-Bahae et al. [14, 15], the Z-scan technique has been widely adopted for the characterization of materials. In this investigation, the primary focus is on characterization of absorptions, therefore, characterization of refraction will not be further discussed.

In all the work for the characterization of absorption by a material, equation (1-1) has been used to describe the coefficient of absorption. It is evident from the Z-scan experimental results reported that there are two distinct regions of absorption, i.e. nonlinear absorption near the focal plane of the laser where the laser intensity is high, and linear absorption far away from the focal where the laser intensity is low. As such, there must be a threshold intensity experienced by the material which delineated the region of linear absorption from the region of nonlinear absorption. Surprisingly, there is no discussion in literature on this threshold intensity.

Without this threshold intensity, when equation (1-1) is used for the calculation of the overall absorption coefficient, there will always be contribution from the coefficient of nonlinear absorption, even in the region of linear absorption only. This does not seem to be appropriate, and further investigation is justified.

In addition, as stated in equation (1-1), the unit of the coefficient of linear absorption (cm^{-1}) and the unit of the coefficient of nonlinear absorption (cm/W) are different. Ideally, as both are coefficients of absorption, they should have the same consistent unit. A different formulation for the overall absorption coefficient should be explored to resolve this lack of unit consistency for the coefficients of absorption.

While using the Z-scan technique, the sample is either classified as a “thin” sample or a “thick” sample by comparing the sample thickness with the Rayleigh length. Generally, the Z-scan studies are only carried out with thin sample experimentally. Some analyses have been reported for “thick” sample by approximating it as a stack

"thin" sample. However, the Rayleigh length has its origin for the description of a laser beam quality. There is a lack of theoretical basis for using it to classify the thickness of a sample. The necessity or appropriateness for the use of this classification has not been elucidated. There is a necessity to examine the necessity or appropriateness of classifying a sample as either a "thin" sample or a "thick" sample based on the Rayleigh length. In addition, nonlinear absorption is strongly dependent on the laser intensity. The implicit assumption of a "thin" sample of having the same absorption mode and characteristic throughout the whole sample thickness might not be justified.

During high intensity laser irradiation, it is evident from the literature, that the laser beam undergoes nonlinear absorption within the sample. Most of the investigations in the literature, including the pioneering work by Mansoor Sheik-Bahae et al. [14, 15] on which other investigations are based, use Gaussian distribution of laser beam in temporal time step and spatial direction. For a Gaussian distribution, the intensity of the laser beam at different spatial position at different time is different. Nonlinear absorption is an intensity dependent phenomenon. As such, the nonlinear absorption of the laser beam by the material will be different at different beam positions at different time, with the absorption especially pronounced at high laser intensity, i.e. generally near the axial region of the beam. Therefore, the beam distribution profile as the laser beam enters the material will evolve, with the peak intensity at the beam axis depressed relatively to other location. The distribution of the beam intensity will not remain as the same as the original distribution. However, hitherto there are no

investigations to be found in the literature on the beam distribution profile within the material and at the exit surface of the material in comparison with the entry distribution.

2.6 Optical breakdown and ablation

Micromachining processes like cutting and drilling with short pulsed laser occur through removal of material. This material removal takes place through ablation. The removed material interacts with the incoming laser beam to produce plasma. In this section, laser ablation and the plasma induced by laser will be reviewed.

2.6.1 Laser ablation of material

Ablation is a multi-step process. The target material first absorbs the laser energy, which can either be linear or nonlinear [1]. The next step of laser ablation is the breakdown of the material. The breakdown occurs with transformation of material into either a liquid or a vapor. The vapor drifts away and removes itself directly; the melted liquid in the interaction region is expelled by the recoil action.

For opaque material, linear absorption is dominant at long or continuous pulse, whereas at ultrashort pulse width, nonlinear absorption is dominant. Hence, laser absorption depends on laser intensity, and the pulse width of the laser [1]. For an optically transparent material at a given laser wavelength, nonlinear absorption is the only dominant mechanism for absorption.

Nolte et al. [99] described two regimes for the ablation process, both depend logarithmically on the laser fluence. For a low laser fluence, the ablation depth is described as:

$$L = \frac{1}{\alpha} ln\left(\frac{\emptyset}{\emptyset_{th}^{\alpha}}\right) \tag{2-38}$$

Where $\boldsymbol{\alpha}$ is the absorption coefficient, $\emptyset$ is the laser fluence and $\emptyset_{th}^{\alpha}$ is the ablation threshold fluence [99]. (Note: - The term '$\boldsymbol{\alpha}$' in $\emptyset_{th}^{\alpha}$ is merely a notation but not the power raised to the ablation threshold fluence).

For increasing laser fluence, the ablation depth can be described as

$$L = \frac{1}{l} ln\left(\frac{\emptyset}{\emptyset_{th}^{l}}\right) \tag{2-39}$$

Where $\boldsymbol{l}$ is the thermal diffusion depth at the higher laser fluence and $\emptyset_{th}^{l}$ is the higher abltation threshold at the higher laser fluence [99]. (Note- Similarly, here '$\boldsymbol{l}$' in $\emptyset_{th}^{l}$ is merely a notation but not the power raised to the ablation threshold fluence.)

The thermal diffusion depth can be estimated as [100]

$$l = 2\sqrt{k\tau_p} \tag{2-40}$$

Where k is the thermal diffusivity of material and τ_p is the laser pulse duration. For a given material, assuming homogeneity, the thermal diffusivity is constant. Thus,

from equation (2-40), it can be observed that with decreasing laser pulse duration, the thermal diffusion depth also decreases.

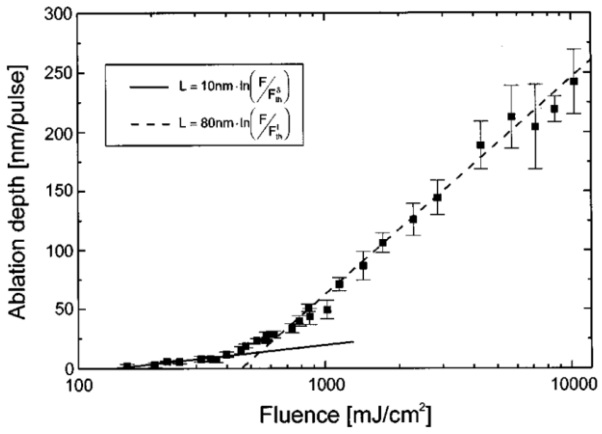

Figure 2-11: Ablation depth per pulse for copper with varying laser fluence. The solid line represents the ablation depth at low fluence region (described by equation (2-38)) whereas the dashed line represents the ablation depth at higher fluence region (described by equation (2-39)). In lower fluence region, threshold fluence $\emptyset_{th}^{\alpha} = 140\,\frac{mJ}{cm^2}$ whereas, the threshold fluence for high fluence region

$$\emptyset_{th}^{l} = 460\,\frac{mJ}{cm^2}$$ [99]

Cheng et al. [101] studied the single-pulse drilling with a 10 ps pulse duration laser at 1024 nm central wavelength on gold, aluminium and titanium alloys used in industrial application. Using a 780 nm laser with pulse duration of 150 fs and repetition rate of 1 kHz, Ostendorf et al. [102] studied the influence of the laser

fluence on the ablation rate on copper and silicon. Their investigations [101, 102] support the two regimes ablation processes.

For ultrafast laser processing of material, optical and thermal properties, and many other factors have effects on ablation [100]. However, the laser pulse duration is the most important factor determining the ablation [103, 104].

2.6.2 Laser-induced plasma

Plasma, often considered as the fourth state of matter, is a hot ionized gas with approximately equal positively charged ions and negatively charged electrons. Different studies on plasma induced during laser material interaction have been reported in [76, 105-107].

In a transparent material, the ionization potential of a bound electron is greater than the laser photon energy. In this case, typically, the bound electrons do not absorb the incoming laser photon. Laser energy absorption via electron and subsequent ionization (and plasma formation) may occur via two mechanisms depending on the strength of laser field intensity:

(a) For low laser field intensity: In any given material, there are always impurities which provide seed electrons from ionization. These seed electrons may come from metallic ions, thermal or linear optical ionization of low energy levels of inclusions [1]. A free electron in a laser electric field cannot absorb laser energy. However, free electrons can absorb laser energy when it collides with the bound electrons and the lattice through dephasing;

this is a Joule heating process known as inverse Bremsstrahlung [1]. The seed electrons then get accelerated. A sufficiently accelerated seed electron when collides with a bound electron can transfer its energy to the bound electron resulting in ionization. This collision will result in two free electrons with low kinetic energy. This is the process of impact ionization. Similarly, two free electrons can collide with other bound electrons in a similar fashion giving rise to more free electrons through impact ionization. As a result free electron density grows exponentially. When enough bound electrons are ionized, a plasma is created with a critical plasma density.

At a given pulse-width, breakdown can be observed only when the laser field strength exceeds a threshold. This threshold is taken as the laser fluence threshold expressed as a function of pulse-width [1]. Only when the laser field strength is greater than the laser fluence threshold, the plasma density increases above the critical value where irreversible breakdown takes place. For a short-pulsed laser, the critical plasma density, n_c, is given as [1]

$$n_c = \frac{m_e \omega^2}{4\pi e^2} \tag{2-41}$$

Here, m_e is the electron mass, ω is the laser frequency. At this critical plasma density, the plasma oscillation frequency equals the laser frequency, and the material becomes completely opaque [1]. For transparent materials in visible or near infrared region, the critical density $n_c \sim 10^{21}\ cm^{-3}$.

(b) For high laser field intensity: High laser intensity can be obtained with ultrashort-pulsed lasers. In this case, seed electrons are not required to ionize the bound electrons. As long as the sum of photon energy absorbed exceeds the ionization potential or bandgap, the bound electrons of the transparent material can be directly ionized through multiphoton ionization.

Zheng et al. [76] compared the ablation plumes during nanosecond pulse machining and femtosecond pulse machining of a stainless steel. It was concluded that nanosecond pulses produced higher concentration of low-energy ions and low-charge-state electrons compared to femtosecond pulses. However, the femtosecond pulses produced well defined plasma even at lower fluences compared to nanosecond pulses. It has been concluded that femtosecond laser pulses are more efficient at producing high-charge-state electrons and high-energy ions. They also concluded that for both, nanosecond and femtosecond laser pulses, significant percentage of the ablated plumes are at a neutral state. This signifies that only a small fraction of the ablated plumes is converted into high-charge-state.

In nanosecond and picosecond laser pulses the interaction is complex [75]. In these cases, the laser-induced plasma has enough time to grow. However, for femtosecond pulses, the plasma has little time to grow. The plasma formed during laser irradiation has an effect on ablation quality and efficiency [100]. This effect has a strong dependence on laser fluence. Plasma shielding occurs for the next incoming laser pulse in low and moderate fluence. Thus, the plasma absorbs some fraction of the

incoming laser beam. However, increasing the laser fluence yields plasma transparent to light [100].

Different studies on the laser-induced plasma in aluminium (at λ = 780 nm) [76], silicon (at λ = 616 nm) [105], lithium manganese oxide ($LiMn_2O_4$) (at λ = 248 nm) [106], and copper (at λ = 800 nm) [107] have been reported in the literature. These materials were opaque for the laser wavelength used.

It is well established that during ultrashort pulse irradiation, the material is ablated, and plasma can be induced by the laser. However, investigations on the laser-induced plasma for a transparent glass seem to be lacking. In particular, although the Z-scan technique is a widely adopted technique for the study of nonlinear behaviour of materials during short pulsed laser irradiation, no study can be found on the effect of the plasma formed during the short-pulsed laser irradiation of material while employing the Z-scan technique.

As such, a study on the laser-induced plasma, its evolution and decay for a transparent material like glass, will be beneficial. A suitable tool for the study of the ultrashort pulsed laser-induced plasma in glass could be high-speed imaging. Indeed, high-speed imaging has been employed for the investigations of related areas such as the study of plasma arc cutting [108] and in combustion research [109] etc.

2.7 Thermography

Thermography is a convenient, non-contact method for temperature measurements over a large area based on electromagnetic waves. Use correctly, it can provide

accurate temperature measurements with little distortion or interference on the temperature of an object being measured.

2.7.1 Fundamentals of thermography

The visible, ultraviolet and infrared radiations are electromagnetic waves. Figure 2-12 (a) gives an overview of the different types of electromagnetic waves with their characteristic frequency and wavelength. For infrared thermography, only a small range (between 0.9 µm to 14 µm) of the infrared spectrum is used, see Figure 2-12(b). This range can be further divided into short-wave (SW) between 0.9 µm to 1.7 µm wavelength, medium-wave (MW) between 3 µm - 5 µm wavelength and long-wave (LW) between 7 µm - 14 µm wavelength.

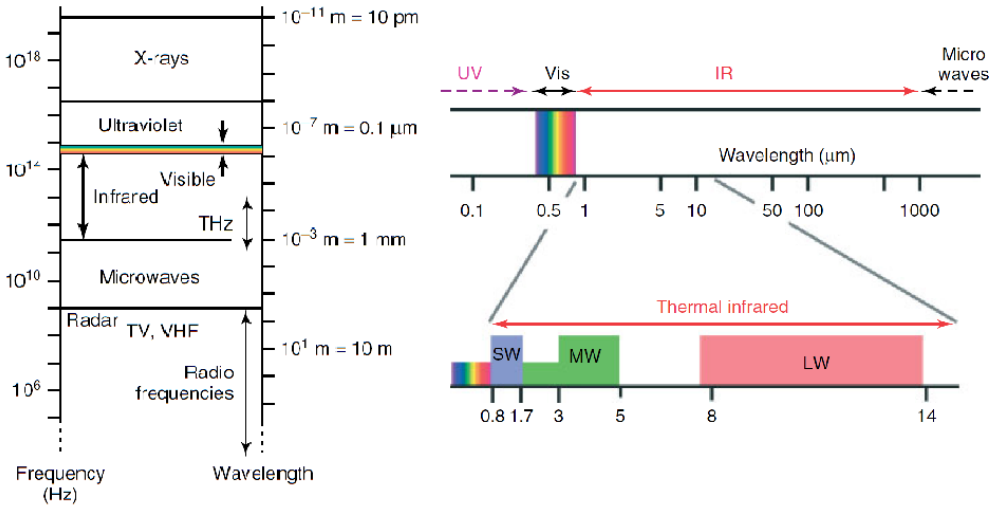

Figure 2-12: (a) Different types of electromagnetic waves with their respective frequency and wavelength. (b) Thermal infrared region showing short-wave (SW), medium-wave (MW) and long-wave (LW) infrared region with their respective wavelength in micro-meter [110].

Thermal radiation is the most important process in thermography. All matters above the absolute zero temperature (i.e. 0 K) emit electromagnetic radiation. The amount of radiation emitted as a function of wavelength is a function of the temperature and emissivity of the body. Thus, the amount of radiation can be directly correlated to the temperature of the body if the emissivity of the body is known.

For infrared thermography, a convenient concept is a "blackbody" indicating an ideal thermal surface satisfying the following conditions [111]:

- A blackbody can absorb all the incident radiation, regardless of direction and wavelength;
- No other body can emit more radiation than a black body for any given temperature and wavelength;
- The radiation emitted by a black body depends on the wavelength but not on the direction of the radiance.

A blackbody serves as a standard body for the study of thermal radiation, and thus thermography, as they are perfect absorber and perfect emitter [110]. In real practice, the non-perfect behaviour of a material can be characterized by its emissivity. Emissivity is defined as the ratio of radiance power of a material to the radiance power of a black body at the same temperature [111]:

$$\varepsilon = \frac{\Phi(T)}{\Phi_o(T)} \tag{2-42}$$

Here, (T) is the power radiance of a real body at temperature T and Φ_o(T) is the power radiance of a blackbody at the same temperature T.

A useful concept is the spectral exitance, which is the total radiant power into the hemisphere of a black body at a given temperature T, in wavelength interval (λ, λ+dλ), given as [111]:

$$M_\lambda(T)d\lambda = \frac{2\pi hc^2}{\lambda^5}\frac{1}{e^{\frac{hc}{\lambda kT}}-1}d\lambda \tag{2-43}$$

where h = 6.626 ×10^{-34} is the Planks constant, c = 2.998 × 10^8 m/s is the speed of light in vacuum, λ is the wavelength of radiation and T is the temperature of the black body in Kelvin. Figure 2-13 shows the spectra of a black body at various temperatures.

The respective radiance, L_λ(T), can be written as [111]:

$$L_\lambda(T) = \frac{M_\lambda(T)}{\pi} \tag{2-44}$$

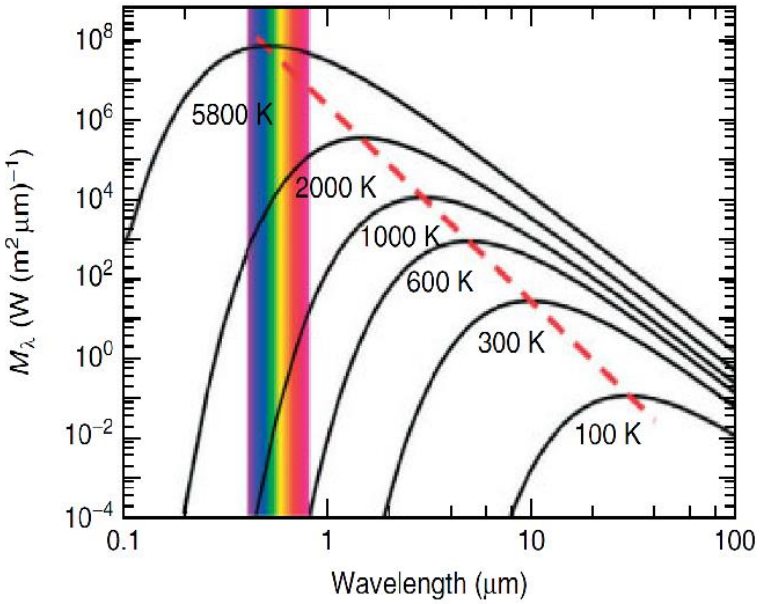

Figure 2-13 : Radiance of black body at different temperature. The rainbow colouring denotes the visible light range. Discontinuous red line passes the maximum radiance for different temperature [110].

From Figure 2-13, which shows the radiance of a black body at different temperature, a number of conclusions can be drawn [110] :

- Emission spectra is continuous,
- For any given wavelength the radiance increases with an increase in temperature,
- Spectral region emission depends on temperature. Higher the temperature shorter is the wavelength of emission, and lower the temperature longer is the wavelength of emission.

The maximum peak of radiance can be determined by differentiating equation (2-44) with respect to wavelength and equating it to zero. From this, Wien's displacement law can be derived as [111]:

$$\lambda_{max} T = 2879.8\ \mu m.K \tag{2-45}$$

Here λ_{max} is the wavelength at which the radiance is a maximum at any given temperature T.

The emissive power of a black body radiation can be related to the temperature of the blackbody by Stefan-Boltzmann law. Stefan-Boltzmann law states that the total radiance power emitted by a black body per unit surface area for all wavelengths per unit time is proportional to the fourth power of the surface temperature of the black body and is written as [111]:

$$E = \sigma T^4 \tag{2-46}$$

where $\sigma = 5.67 \times 10^{-8}\ Wm^{-2}K^{-1}$ is Stefan's constant. For any real body, the Stefan-Boltzmann law is written by introducing the surface emissivity of a body, $\boldsymbol{\varepsilon}$, as [111]

$$E = \varepsilon \sigma T^4 \tag{2-47}$$

Here $\boldsymbol{\varepsilon}$ is the surface emissivity of a real body as defined by equation (2-42).

The emission of any object can be determined using the surface emissivity (**ε**) and temperature (T), which can be described using Planck's Law, Wien's Displacement Law and Stefan-Boltzmann Law.

2.7.2 Applications of thermography in ultrashort pulsed laser irradiation

As discussed earlier, thermography is a convenient, non-contact method for temperature measurements. It can provide accurate temperature measurements with little distortion or interference on the temperature of an object being measured. Therefore, thermography can be a useful tool for the study of heat absorption by the material during laser irradiation through the proper interpretation of the obtained temperature field.

It had been a popular belief that there is no or negligible heat deposition into the bulk of a material during ultrashort pulsed laser irradiation [112, 113]. However, it has been shown that in copper, silicon, or steel, more than 50%, 66.7%, and 67% respectively of the total incident laser energy was deposited into the materials [77-79]. All these materials were not transparent at a given laser wavelength of λ = 775 nm. For transparent polystyrene, at a laser wavelength of λ = 795 nm, it was shown that significant heat deposition occurs during femtosecond laser irradiation [63]. All the observations for temperature distribution in [63, 77-79] were achieved using thermography.

This, thermography can be used to study the thermal effect induced by a femtosecond laser and its subsequent heat conduction after laser power absorption in both a

transparent or a non-transparent material. It will be appropriate to explore here the use of thermography to register the temperature fields of a sample, and to correlate these temperature fields with the calculated temperature fields derived from the determined coefficients of absorption.

Chapter 3: Methodology

3.1 Introduction

To understand the short-pulsed laser interaction with a chemically strengthened glass during laser processing, nonlinear absorption must be considered. Here in this chapter, equipment and methods employed during the study of interactions will be discussed.

3.2 Laser system

Femtosecond laser system Quantronix Integra-C 1.0 has been employed. It is a Ti: Sapphire amplifier system. It uses Calmar's Q-Light PM as seed laser and Darwin 527-40-M, an Nd: YFL rod laser, as a pump laser. Chirp pulse amplification is employed to produce the output laser pulse. It employs both regenerative amplification and multi-pass amplification; specifically, it uses two-pass amplification. Specification of the output laser is listed in Table 3-1.

Table 3-1: Integra-C 1.0 specification

Repetition rate	1.0 kHz
Central wavelength	795 nm ± 10 nm
Energy per pulse	1.5 mJ
Pulse width (FWHM)	<130fs
Beam Size (Gauss fit FW $1/e^2$ M)	7 mm
Objective focal length	163 mm
Beam waist at focus (Diameter)	30 μm

3.3 Z-scan technique

The z-scan technique can be employed as an effective and efficient method for the study of nonlinear absorption and nonlinear refraction [16]. In this study, the standard open-aperture Z-scan technique [14, 15] has been employed for the experimental investigation, albeit with a slight variation. The limit of z-translation, positive z distance and negative z distance, has been increased from the recommended value of $\pm 5z_R$ (Rayleigh length) [14, 15]; this is to allow for an accurate analysis of the linear absorption region in addition to the nonlinear absorption region.

As discussed in the previous chapter, transmission power through the sample can be interpreted for the study of nonlinear absorption and nonlinear refraction. In this section the equipment used, experimental setup and experimental procedure employed for the study of nonlinear absorption will be elaborated.

3.3.1 Material and devices employed

3.3.1.1 Laser system

Quantronix Integra-C 1.0 laser amplifier system at 795 nm ± 10 nm wavelength has been used. The maximum average power of the laser system is 1.5 W; however, experiments have been conducted at attenuated power levels. The collimated laser beam from the Integra-C 1.0 amplifier system is focused using a f-θ lens with a focal length of 163 mm. The FW $1/e^2$ M diameter of the unfocused TEM_{00} laser beam is 7 mm. At the focal plane, the beam waist is 30 μm.

3.3.1.2 Thermopile power sensor

Coherent's PowerMax-USB model PM-USB PM3, a thermopile sensor, has been employed to measure the laser power. The range in which PM3 can measure is 500 μW to 2 W. PowerMax-USB PM3 is thermally stabilized for low-power sensitivity. The maximum power density and the maximum energy density of the thermopile sensor are 500 W/cm^2 and 50 mJ/cm^2 respectively. The diameter of the thermal sensor is 19 mm. The response time of the sensor is 1.9 s.

3.3.1.3 Sample

Gorilla glass 2320, a chemically strengthened glass, manufactured by Corning Incorporated (USA) has been used. The compressive stress of Gorilla glass 2320 is greater than 950 MPa with a depth of compressive layer more than 50 μm. Sample dimensions used in the study are 50 mm × 50 mm × 500 μm.

3.3.2 Experimental setup

Standard open aperture Z-scan technique has been employed for the study of the coefficients of nonlinear absorption. In the open aperture Z-scan technique, the whole laser beam exiting the sample's surface is measured by the sensor as depicted in Figure 3-1.

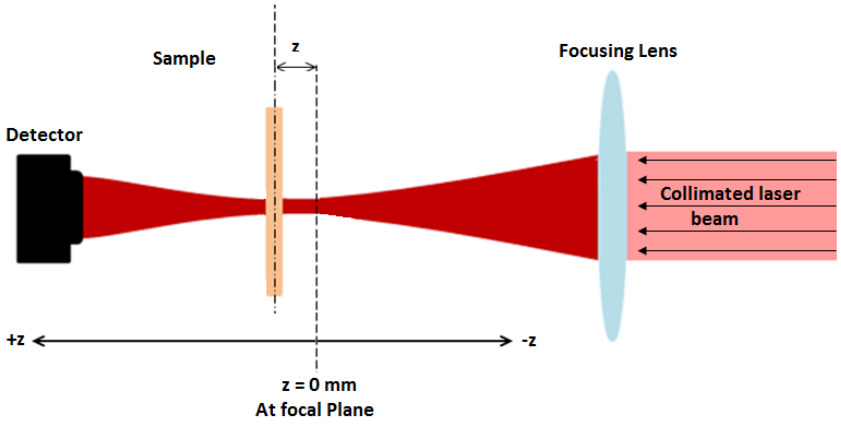

Figure 3-1: Schematic diagram of open aperture Z-scan technique

The power transmitted at different laser intensity through a sample is to be measured by the PowerMax PM3 sensor. Different laser intensity is achieved by translating the glass sample along the laser propagation axis, in particular through the focal plane of the laser beam. The beam diameter of the laser beam at any given z position is [14, 15]

$$w_z = \sqrt{w_o^2\left(1+\left(\frac{z}{z_R}\right)^2\right)} \tag{3-1}$$

Where w_o is the beam diameter at the focal plane and $z_R = {}^{\pi\omega_o^2}/_{\lambda}$ is the Rayleigh length with λ being the laser wavelength. To avoid damaging the thermopile power sensor, the sensor was placed at a position where the power density and energy density did not exceed the maximum power density and maximum energy density allowable of the sensor. Power density and energy density are respectively calculated as

$$I = \frac{P}{\pi w_z^2} \tag{3-2}$$

$$F = \frac{E}{\pi w_z^2} \tag{3-3}$$

The maximum power density of the thermopile power sensor is 500 W/cm^2. For the laser operating at its maximum power of 1.5 W, the minimum beam radius w_z should not be less than 0.31 mm. From equation (3-1), for $w_z \geq 0.31$ mm, the thermopile has to be located at 18.3 mm or further from the focal point. As the diameter of the thermopile sensor is 19 mm, the distance of the sensor from the focal plane should be less than 563.1 mm to ensure that the whole laser beam is within the sensor.

The experimental procedure is as follow:

1. The laser system was switched on and left idle for at least 30 min for the power to stabilize.
2. The sample holder was placed in the XYZ translation stage. Gorilla Glass 2320 was clamped to the sample holder. The position of the sample holder was maintained at 163 mm below the scanner.
3. The thermal sensor was placed below the sample. Not to damage the thermopile sensor, the sensor was placed approximately 100 mm below the focal plane; this is to ensure the capturing of the whole laser beam and to avoid the power intensity of the incident laser beam exceeding the allowable maximum power density of the thermopile sensor. To ensure proper

alignment such that the whole laser beam was collected by the sensor, sensor alignment was achieved using leaked laser power.

4. The sample was removed from the sample holder and the laser power was measured. Three measurements of the power were taken for 5 s each. The measurement time of 5 s was chosen to ensure proper measurement as the response time of the thermopile sensor is 1.9 s. The average of three measurements gave the reference power for laser irradiation.
5. The sample was then placed on the sample holder. The laser was turned on and focused at the surface of the sample. The sample was then translated 250 μm towards the lens ensuring that the focal plane of the laser is at the central plane of the glass. This position was then established as the z = 0 reference point.
6. The sample was translated along the z-direction using the XYZ translational stage. Starting from a far-point, where there is only linear absorption, the sample was moved towards the focus and beyond. The stepping along the z-direction was not maintained constant. In the linear absorption regime far away from the focal plane, a step size of 500 μm was used. When the sample was near the focal plane and thus approaching the nonlinear absorption regime, the step size was reduced to 100 μm. At every step, three readings of 5 s each were measured.
7. Once all the readings were taken, the sample was removed from the sample holder. Three further readings were taken and compared with the initial readings without the sample. The comparison of the readings provides a good

assessment of the power stability of the laser throughout the whole experiment.

8. Step 3 to step 6 was repeated for different power levels.
9. The absorption curve was plotted against the z-distance. Absorption was calculated as the difference between the reference power without the sample and the transmitted power measured with the sample at different z-positions.

3.4 Thermal Measurement

Direct observation of temperature distribution during laser irradiation on Gorilla Glass 2320 has been studied. The thermal measurement was conducted using FLIR® Silver SC5000 thermographic camera. The thermal measurements has been conducted at different z-position with experimental setup following the standard Z-scan technique; this is the first-of-its-kind direct observation of thermal energy for correlation with the Z-scan measurement of laser energy absorption. The thermal camera was first calibrated using thermocouples prior to the study of the temperature distribution of the sample during laser irradiation. Appendix I provides the calibration details.

3.4.1 Materials and devices employed

3.4.1.1 Chemically strengthened glass

Gorilla Glass with code Gorilla 2320 from Corning Singapore was used for the experiment. The dimensions of the glass specimen are 50mm × 50 mm × 500 μm. The compressive stress at the surface of the glass is greater than 950 MPa with a minimum depth of the compression layer greater than 50 μm.

3.4.1.2 Infrared thermal camera

FLIR® Silver SC5000 Medium Wave Infrared (MWIR) camera has been used for thermography. It has a highly sensitive Indium Antimonide (InSb) focal plane array for IR measurement. The thermal camera can be operated up to 380 Hz at full frame rate. The camera has a 27 mm embedded lens with focal number f/3. For the current experiments, medium wave G3 F/3.0 lens with magnification number 3 ± 5% was employed. The MW G3 lens operates at the spectral band of 3.7 µm to 5.15 µm. The focal point of the lens is 38.8 mm ± 0.01 mm from the objective lens. The resolution at which the camera can be operated using MW G3 lens is 320 × 256 for 30 µm pitch detector and 630 × 512 for 15 µm pitch detector. Thus, small area temperature can be precisely measured with high accuracy.

3.4.1.3 Thermopile power sensor

Coherent's PowerMax-USB model PM-USB PM3, a thermopile sensor, has been employed to measure the laser power as described in section 3.3.1.2 (above).

3.4.1.4 Paint

To increase measurement sensitivity, the surface under observation was painted with PNM400 black paint purchased from RS Components Pte. Ltd, which has an emissivity close to unity.

3.4.2 Experimental setup

A schematic diagram for the direct observation of temperature distribution during laser irradiation on Gorilla Glass 2320 is shown in Figure 3-2.

The glass sample was painted black on the observation edge with PNM400 black paint. The spray-painted edge was left to air dry. During painting, not only the edge was painted, but the lateral surfaces from the edge were also painted. Once the paint was dried, excess paint from the lateral surfaces was removed using ethanol, and the sample was left to air dry. Visual observation was conducted to ensure that the edge was properly painted with no residual paint on the lateral surfaces. The removal with ethanol and air drying was repeated if there was any residual paint on the lateral surfaces.

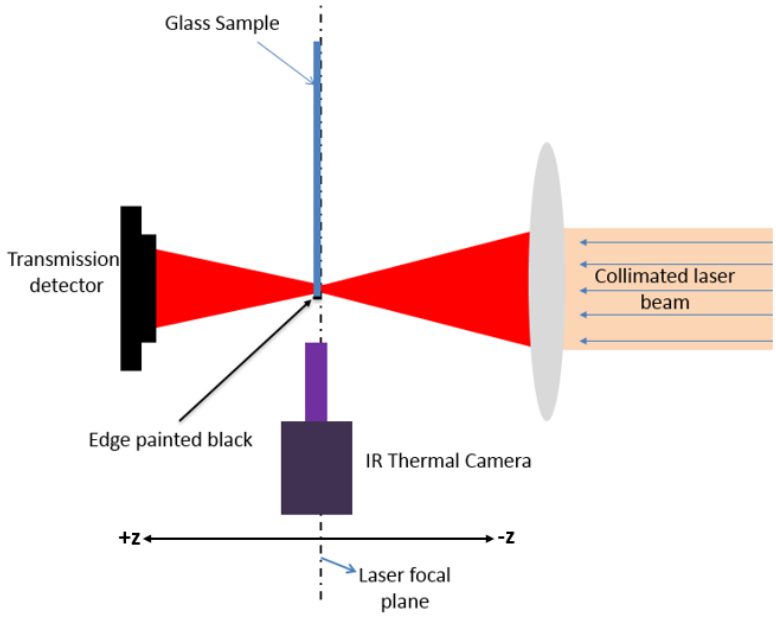

Figure 3-2: Schematic diagram for direct observation of temperature distribution during laser irradiation

Once the edge was painted, the sample was mounted on the sample holder on the XYZ translation stage. The sample was placed on the laser path near the focal plane of the focusing lens. Sample position was adjusted using the XYZ translation stage

in such a way that the centre of the incident radiation was always 2 mm away from the painted edge. Thermopile power sensor was placed behind the sample along the laser axial direction. With the same considerations as outlined in section 3.3.2 (above) for conducting the Z-scan experiment, the thermopile power sensor was placed 100 mm away from the focal plane of the focusing lens; this was to ensure that the thermopile power sensor would not be damaged. FLIR® MWIR SC5000 thermal camera was focused on a point nearest to the laser irradiation site on the black-painted edge.

The experimental procedure is as follow:

1. The laser system was switched on and left idle for at least 30 min for the power to stabilize.
2. Laser power was measured with a thermopile power sensor without the sample. Measurement was conducted three times for 5 seconds each. The average measured power was established as a reference power for the incident radiation.
3. The sample was mounted on the XYZ translation stage using a sample holder. The mounting ensured that the black painted edge was facing the infrared camera to facilitate temperature measurements.
4. The laser beam was focused on the entry surface of the sample. Using the translation stage, the position of the sample was maintained in such a way that the center of laser irradiation was 2 mm away from the black-painted edge. The sample was translated by 250 μm along the z-direction towards the

focusing lens; it ensured that the focal plane of the focusing lens was at the central plane of the glass sample along the thickness direction.

5. Infrared camera FLIR® MWIR SC5000 was focused on the black painted edge. Determination for the position nearest to the laser incident site was done by hit-and-trial method. Spirit level was used to ensure that the thermal camera was perpendicular to the edge under observation.
6. Three observations were made with laser on for 5 seconds each. During this time the transmitted power was collected using the thermopile sensor. Simultaneously, using the FLIR® MWIR SC5000, thermal images were taken 10 seconds at 50 Hz sampling frequency.
7. The z-position of the sample was varied, on both positive and negative directions, and similar observations were conducted. Step 5 and step 6 were repeated at every new z-positions.
8. The power level was again measured without a sample and compared with the initial measurements without the sample to ensure the laser power was stable throughout the experiment.

3.5 Plasma observation with high-speed imaging

High-speed imaging can be used to visually observe different phenomena [108, 109], and has been employed here for the observation of the plasma formation during laser irradiation on Gorilla Glass 2320. Plasma at different z-positions has been observed during Z-scan measurement; this is the first-ever reported plasma observations for

correlation with Z-scan measurements. In this section, the materials and devices employed, experimental setup and experimental procedure will be outlined.

3.5.1 Materials and devices employed

Plasma formation during laser irradiation on Gorilla Glass 2320 was observed using high-speed imaging with Photron's FASTCAM SA5.

3.5.1.1 Photron's FASTCAM SA5

Photron's FASTCAM SA5 is a high-speed video system with complementary metal-oxide semiconductor (CMOS) sensor. It has a 12-bit analog-to-digital converter (ADC) with 20 μm pixel size. FASTCAM SA5 is capable of imaging up to 1,000,000 frames per second at a resolution of 64 × 16 bits with a maximum shutter speed of 369 ns. It is capable of imaging at 7000 fps with a resolution of 1024 × 1024 bits.

In Figure 3-3, the solid line shows the spectral response of the CMOS sensor with a responsive broad spectrum.

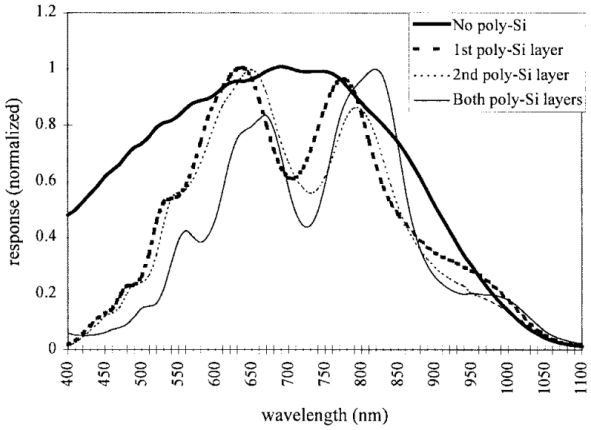

Figure 3-3: Response of CMOS photodiodes with coverings of (a) No polycrystalline silicon, (b) the first polycrystalline silicon layer, (c) the second polycrystalline silicon layer, and (d) both polycrystalline silicon layers [114]

3.5.1.2 Optical filters

Figure 3-3 shows that the CMOS sensor is highly responsive at the laser wavelength of 795 nm, the laser's central wavelength. During imaging, it is highly undesirable to have image saturation because of the high-intensity laser pulse. Moreover, the laser pulse has very high peak power intensity; even a small amount of reflected beam during imaging can be focused onto the sensor damaging it. Therefore, a FESH0750 cut-off filter with a cut-off wavelength of 750 nm, or a FELH0850 cut-on filter with a cut-on wavelength of 850 nm, both from the Thors Lab, were employed. The cut-off and cut-on wavelengths for the filters were selected such that they are as close as possible to the laser wavelength; this ensured that almost all the light during the experiment, either below or above the laser wavelength was captured by the camera. Further discussions are presented in section 5.2.1 (below).

3.5.1.3 Metal halide lamp

During high-speed imaging, the shutter speed is fast, and FASTCAM SA5 can reach up to 1/930,000 sec. As such, ambient light was not sufficient for proper imaging. A metal halide lamp MLDS250-2/DT with a power rating of 250W was employed to increase the illumination. It is equipped with both ultraviolet and infrared cut-off filters.

3.5.2 Experimental setup

A schematic diagram for the observation of plasma formation during laser irradiation with the femtosecond laser on a glass sample is shown in Figure 3-4.

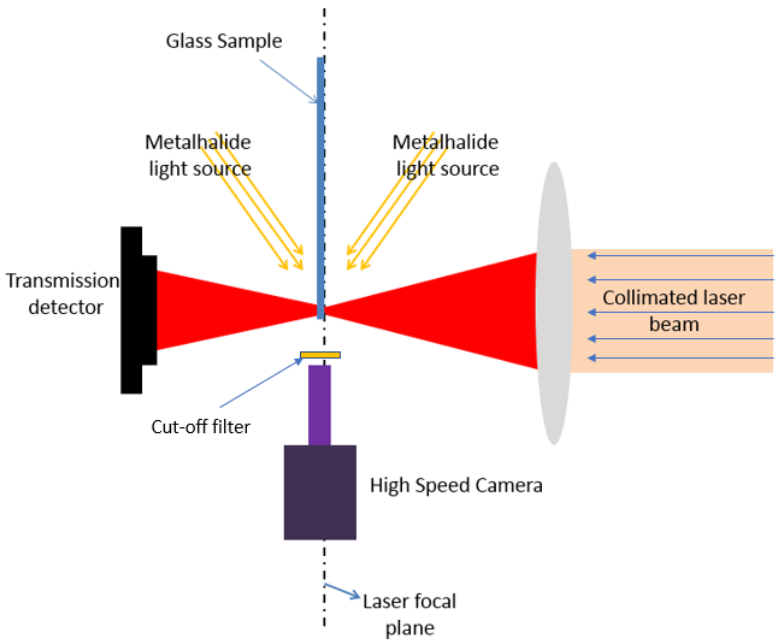

Figure 3-4: Schematic diagram to observe plasma formation during laser irradiation

The experimental setup is similar to the direct observation of temperature distribution using FLIR® Silver SC5000 thermographic camera. However, for high speed imaging, Photron's FASTCAM SA5 high-speed camera has been employed. The sample was placed in a sample holder and was clamped to the XYZ translation stage. The position of the sample was maintained in such a way that the point of irradiation was near an edge of the sample. With the same considerations as outlined in section 3.3.2 (above) for conducting the Z-scan experiment, the thermopile power sensor was placed 100 mm away from the focal plane of the focusing lens; this was to ensure that the thermopile power sensor would not be damaged. Illumination with metal halide lamp was directed at the point of laser irradiation from the opposite location of the high-speed camera. The high-speed camera was oriented in such a way to focus on the site of laser irradiation near the sample's edge.

The experimental procedure is as follow:

1. The laser system was switched on and left idle for at least 30 min for the power to stabilize.
2. Laser power was measured with a thermopile power sensor without a sample. Measurement was done three times for 5 seconds each. The average measured power was established as the reference power for incident radiation.
3. The sample was mounted on the XYZ translation stage using a sample holder.
4. The laser beam was focused on the entry surface of the sample. Using the translation stage, the position of the sample was maintained in such a way

that the center of laser irradiation was 2 mm away from the edge towards the high-speed camera. Subsequently, the sample was translated by 250 μm along the z-direction towards the focusing lens; it ensured that the focal plane of the focusing lens was at the central plane of the glass sample along the thickness direction.

5. Photron's FASTCAM SA5 was focused on the site of laser irradiation. Determination for the site of the laser incident was done by hit-and-trial method. Spirit level was used to ensure that the thermal camera was perpendicular to the edge under observation.
6. Three observations were made with the laser on. During imaging, the following considerations were made:
    a. The frame rate was fixed for each experiment.
    b. Zero-calibration was performed each time the camera setting was changed by closing the shutter.
    c. High-speed images were taken using Photron's FASTCAM SA5 and stored in the computer.
7. Multiple experiments were performed with images taken at frame rates of 60 fps, 1,000 fps, 3,000 fps, 10,000 fps, 50,000 fps, 300,000 fps, and 930,000 fps. For each frame rate, step 6 was repeated. (Note: optical filters FESH0750 and FELH0850 were employed for imaging at 60 fps to establish the appropriate filter choice; subsequently, only FELS0750 was used for all the other observations.)

8. The z-position of the sample was varied, on both positive and negative directions, and similar observations were made for each z-position. Step 5, step 6, and step 7 were repeated at every new z-positions.
9. The power level was again measured without a sample and compared with the initial measurements without the sample to ensure that the laser power was stable throughout the experiment.
10. The experiment was repeated for two power levels. Steps 2 to steps 9 were executed for each power level.

Chapter 4: Optical absorption characterization

4.1 Introduction

For machining of material with laser irradiation, absorption of laser power by the material is a necessity. The material can be opaque or transparent at the given laser wavelength. For an opaque material, linear absorption is the main mode of laser power absorption. In contrast, for a transparent material, nonlinear absorption is the primary mode of laser power absorption. In this investigation, both modes of absorption in a transparent material, Gorilla Glass 2320, will be studied.

For this investigation on laser power absorption, the Z-scan technique has been adopted. As discussed in Chapter 2, Z-scan measurements have been employed by researchers for the characterization of optical properties. These include the study of both thin and thick optical media. Most of the research focuses on thin material; however, in practice, it is always not practical or appropriate to characterize a material using thin approximation. There are only a few investigations on thick materials and they are limited to theoretical analysis with simplified assumptions.

Here a detailed investigation of nonlinear absorption has been conducted with the introduction of a nonlinear absorption threshold. The Z-scan technique with open aperture has been adopted for the study of the nonlinear absorption coefficient of Gorilla 2320, with the associated experimental procedure already discussed in Chapter 3, section 3.3.2 (above). The intensity distribution within the material and the energy absorbed within the material are analysed. The implicit simplified

assumptions of the current Z-scan technique are discussed. Further, a numerical technique has been developed to overcome the limitation of the assumptions. In addition, the existing equation in the literature for describing the coefficient of nonlinear absorption and the characterization of a "thin" or "thick" sample are examining.

4.2 Theoretical analysis

In general, a short pulse laser, with power delivered in timescale less than 1 ps, has very high peak intensity; this results in optical breakdown and thus nonlinear absorption in a transparent material. In this investigation, Quantronix Integra-C 1.0 amplifier laser system with a pulse-width duration of 130 fs and central laser wavelength of 795 nm has been employed for the investigation of the nonlinear absorption coefficient.

Laser fluence is the total laser energy per unit area whereas laser power intensity is defined as the laser power per unit area. Use of laser power intensity instead of laser fluence facilitates ease of accounting for high peak power and instantaneous power. Thus, laser power intensity, instead of laser fluence, has been employed for this study. For the analysis, the following approximations have been adopted:

1. The axis of the laser beam is perpendicular to the surface being irradiated.
2. The incoming laser beam has a standard Gaussian temporal profile i.e.

$$I(t) = I_{ot} exp\left(-\frac{(\mathrm{t} - t_o)^2}{2\sigma_t}\right) \tag{4-1}$$

Where I_{ot} is the peak temporal laser intensity, σ_t is the temporal standard deviation of the laser beam and t_o is a time of central peak location.

3. The incoming laser beam has a standard Gaussian spatial profile i.e.

$$I(r) = I_{or} exp\left(-\frac{r^2}{2\sigma_r}\right) \tag{4-2}$$

Where I_{or} is the peak radial laser intensity, and σ_r is the spatial standard deviation of the laser beam. In the case of the spatial profile, the laser beam has been assumed to have a central peak at the axis of propagation.

4. Thus, at any given time the instantaneous intensity of the incoming laser beam can be described as

$$I_s(r,t) = I_o(z) exp\left(-\frac{r^2}{2\sigma_r^2} - \frac{(\mathrm{t} - t_o)^2}{2\sigma_t^2}\right) \tag{4-3}$$

Where $I_s(r,t)$ is intensity distribution profile of laser beam at the surface of the sample with respect to the radial distance and the time step and $I_o(z)$ is the peak power intensity at the surface when the sample surface is z-distance away from the focal plane.

Equation (4-3) is necessary only for the incoming laser beam at the surface of laser irradiation. It does not, however, means that the beam will maintain a Gaussian profile when the material enters the transparent material. Indeed, the change in laser profile as it propagated into the material is accounted for by the analysis.

5. The Gorilla Glass 2320 is assumed to be isotropic in nature at the given laser wavelength.

With these assumptions (in particular the first three assumptions), the laser irradiation can be and has been treated as an axisymmetric system. All the subsequent formulation will treat the laser irradiation on the Gorilla Glass 2320 as asymmetrical.

The above assumptions are valid for the experimental investigations in this study. Indeed, as a numerical technique has been developed to describe the propagation of the laser beam through the medium, the axisymmetric assumption can be relaxed by having an appropriate equation to describe the incoming laser beam distribution and its relationship with the medium, and a 3D formulation of the numerical procedure.

As mentioned earlier, Z-scan experiments are performed for the determination of coefficients of absorption and nonlinear absorption threshold intensity. It should be noted that the position z = 0 refers to the position of the focal plane. The schematic diagram in Figure 4-1 shows the position of the sample with respect to the focal plane.

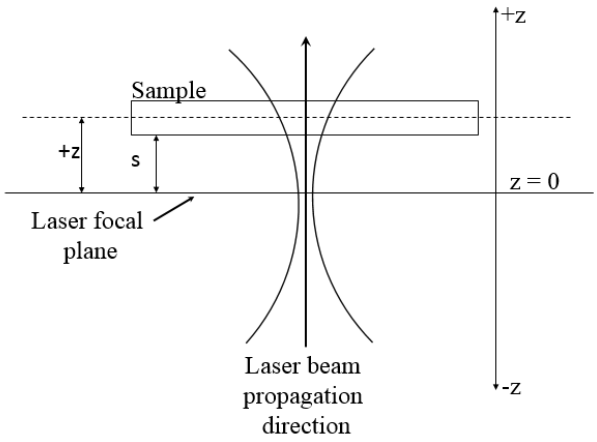

Figure 4-1: Schematic diagram of the laser beam with a sample at z-distance away from the focal plane.

In Figure 4-1, the z-distance is defined as the distance between the central plane along the thickness of the sample and the laser focal plane. If the sample is placed further away from the focal plane, it is considered as having a positive z-distance (as shown in Figure 4-1); conversely, if the sample is placed before the focal plane it is considered as having a negative z-distance. Also, the distance '*s*' is defined as the position of the sample surface facing the laser beam (the entry surface of the laser beam), with respect to the laser focal plane. This distance definitions will be adopted in the subsequent analysis unless otherwise specified.

4.2.1 Nonlinear absorption coefficient formulation

A lot of studies have been conducted for the study of nonlinear optical properties in different materials [14, 15, 19, 20, 22-24, 27-29, 33, 42, 44, 71]. Most of these follow the pioneering work of Mansoor Sheik-Bahae et al. [14, 15] who introduced the Z-scan technique for optical characterization. In these previous studies of the nonlinear

absorption coefficient, the intensity-dependent overall absorption coefficient *α(I)* has been represented as in equation (1-1) in section 1.1(above), Chapter 1 [14, 15]:

$$\alpha(I) = \alpha + \beta I \qquad (1\text{-}1)$$

Where α is the coefficient for linear absorption and β is the coefficient for nonlinear absorption.

Using the Z-scan technique, Mansoor Sheik-Bahae et al. [14, 15] showed that in positions away from the focus there is only linear absorption; when the sample is translated toward the focus, and at a distance sufficiently close to the focus, nonlinearity absorption commences. During the translation of the sample towards the focus, the beam diameter decreases with increasing laser power intensity. As such, there is clearly a threshold intensity beyond which nonlinear absorption commences.

Interestingly, none of the previous work in the literature has reported or utilized this nonlinear absorption threshold intensity. This investigation defines the nonlinearity absorption threshold intensity I_{th} as a laser intensity threshold for the commencement of nonlinear absorption. This study will further demonstrate the importance of having this threshold for proper accounting of absorption in general, and nonlinear absorption in particular.

In addition, in equation (1-1), the coefficients for linear and nonlinear absorptions, i.e. α and β respectively, have different units, namely 1/cm for α and cm/W for β. As both are absorption coefficients, for consistency, they should both have the same

units, and ideally the unit of α. This has been achieved in this study with a theoretical formulation through the incorporation of I_{th}.

The laser power intensity decay may occur dramatically while the laser traverses the thickness of a material because of the nonlinear absorption process. As such, the propagating laser beam may experience a change in the mode of absorption from dominantly nonlinear to linear absorption. Accounting all these scenarios, the overall coefficient of absorption has been reformulated and defined in this study as

$$\alpha = \begin{cases} \alpha_o & \forall\, I(z,r,t) < I_{th} \\ \alpha_o + \alpha_1 \cdot \dfrac{I(z,r,t)}{I_{th}} & \forall\, I(z,r,t) \geq I_{th} \end{cases} \tag{4-4}$$

Where α_o is the coefficient of linear absorption and α_1 is the coefficient of nonlinear absorption, with the same unit as α_o. Equation (4-4) describes explicitly the commencement of nonlinear absorption, and its contribution to the value of the overall absorption coefficient. This transition to nonlinear absorption is accounted for by comparing the instantaneous positional intensity with the nonlinear absorption threshold intensity. By normalizing the instantaneous positional intensity with the threshold intensity in equation (4-4), the coefficient of nonlinear absorption α_1 will have the same, and thus consistent unit as the coefficient of linear absorption α_o.

4.2.2 Formulation of laser energy distribution within the material

For a rigorous study of nonlinear energy absorption within a material, when the laser traverses the material, the energy distribution within the material at any location and

time has to be determined. A mathematical model has been developed for the study of energy distribution as a function of time with respect to a location within the sample thickness.

Let us consider a transparent material of thickness ***l*** is irradiated with a laser beam with intensity distribution described by equation (4-3). Figure 4-2 shows a schematic diagram of laser beam profile focused z_o below the surface with respective intensity distribution profiles.

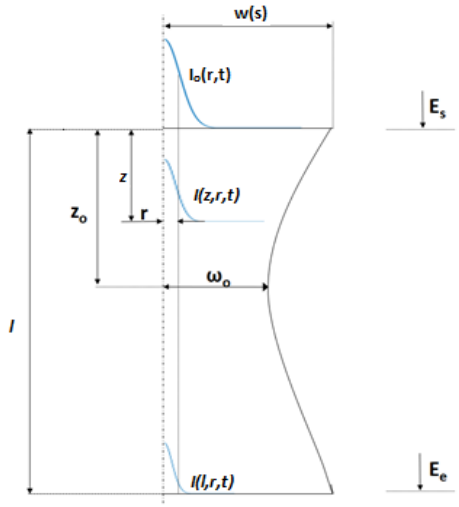

Figure 4-2: Schematic diagram of laser irradiation focused inside the material at distance s below the surface. $I_o(r,t)$ is incoming laser intensity profile at the entry surface of the sample at given values of r and t, $I(z,r,t)$ is intensity at a position '*z*' below the surface of the sample and $I(l,r,t)$ is the intensity profile at the exit surface of the glass. E_s is total energy entering the surface and E_e is total energy exiting the surface

The laser beam profile, $\omega(z)$, with a beam waist radius of ω_o, can be described by equation (3-1) in Chapter 3 section 3.3.2 as [14, 15] :

$$w_z = \sqrt{w_o^2\left(1 + \left(\frac{z}{z_R}\right)^2\right)} \tag{3-1}$$

Where, $\boldsymbol{\lambda}$ is the central laser and z_R is the Rayleigh length.

Let us denote the total laser energy irradiated into the material be E_s, and the energy that exits the material be E_e. The difference between the energy that enters the material and the energy that exits the material is the total energy that is absorbed by the material.

Figure 4-3 represents an elemental area z-distance below the surface of the sample in polar coordinates.

The energy contained in the elemental area ABCD can be written as

$$dE = I(z, r, t) \cdot dA \cdot dt \tag{4-5}$$

For the polar coordinate system,

$$dA = dr \cdot dl \tag{4-6}$$

$$dl = r \cdot d\theta$$

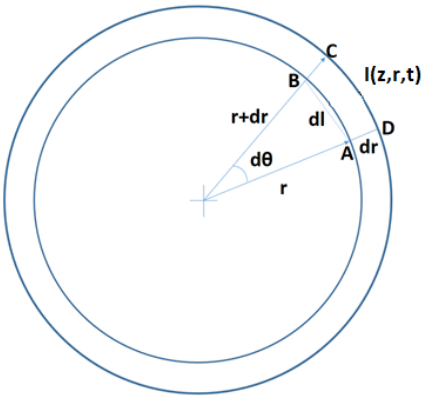

Figure 4-3: Polar representation of a radial system with *dr* elemental radial length and *dθ* elemental revolving angle. *I(z,r,t)* is the fluence at the elemental area ABCD.

Thus, energy contained in elemental area ABCD can be written using equation (4-5) and equation (4-6) as,

$$dE = I(z,r,t) \cdot r \cdot dr \cdot d\theta \cdot dt \tag{4-7}$$

The total energy contained in a plane z-distance below the surface can be determined by integrating equation (4-7) with respect to *r*, *θ,* and *t* as:

$$E(z) = \int_0^{\tau} \int_0^{2\pi} \int_0^{\omega(z)} I(z,r,t) \cdot r \cdot dr \cdot d\theta \cdot dt \tag{4-8}$$

Where τ is the laser pulse duration and $\omega(z)$ is the beam radius at a position z-distance from the surface of the sample. Equation (4-8) can be used to determine the total energy of the laser beam at z-distance below the surface of irradiation.

At the entry surface, the total energy input E_s can be calculated using equation (3-1), equation (4-3) and, equation (4-8) as

$$E_s = \int_0^{\tau}\int_0^{2\pi}\int_0^{\omega(s)} I_o(z)exp\left(\frac{-9r^2}{2[\omega(s)]^2} - \frac{-2.726t^2}{[t_{FWHM}]^2}\right) r \cdot dr \cdot d\theta \cdot dt \quad (4\text{-}9)$$

Where $\omega(s)$ is the beam radius of the income beam at the surface of irradiation, t_{FWHM} is the Full-Width Half-Maximum time of the laser pulse duration.

4.2.3 Volumetric energy absorption formulation

The energy absorbed within the material is to be determined. Let us consider an elemental volume in cylindrical coordinate as shown in Figure 4-4.

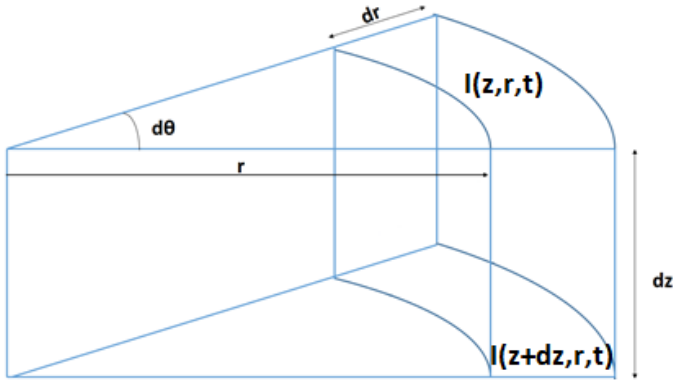

Figure 4-4: Elemental volume in cylindrical coordinate with *dr* as elemental radial length, *dz* as elemental axial length and *dθ* as the elemental revolving angle. *I(z,r,t)* is the laser intensity when it enters the elemental volume at position r distance away from the beam axial position and z-position below the surface at any given time t. *I(z+dz,r,t)* is the laser intensity at the exit of the same elemental volume of thickness dz.

The energy that will be absorbed by an elemental volume can be given as

$$dE = \frac{dI(z,r,t)}{dz} dV.dt \tag{4-10}$$

Where dI/dz is the rate of change of intensity as the laser traverse the elemental volume. Equation (4-10) defines the energy absorbed per unit differential volume. Power absorbed per unit elemental volume is given by [14, 15]

$$\frac{dI(z,r,t)}{dz} = -\alpha \cdot I(z,r,t) \tag{4-11}$$

Where α is the overall absorption coefficient as defined by equation (4-4).

The energy absorbed in an elemental volume can be calculated as,

$$dE = \frac{dI(z,r,t)}{dz} \cdot r \cdot dr \cdot d\theta \cdot dz \cdot dt \tag{4-12}$$

The volume integral with time integral of equation (4-12) will give the total energy absorbed by the system as

$$\int_{E_s}^{Ee} dE = \int\int\int\int \frac{dI(z,r,t)}{dz} \cdot r \cdot dr \cdot d\theta \cdot dz \cdot dt \tag{4-13}$$

Expanding equation (4-13) using equation (4-11) will result in

$$E_e - E_s = -\int_0^{\tau}\int_0^{l}\int_0^{2\pi}\int_0^{w(l)} \alpha \cdot I(z,r,t) \cdot r \cdot dr \cdot d\theta \cdot dz \cdot dt \tag{4-14}$$

α is the overall absorption coefficient as defined in equation (4-4) and E_s is the energy exiting the sample.

For a Gaussian laser beam, the energy that enters the material at the surface of the material has a Gaussian distribution. However, the fluence distribution exiting the material will not be Gaussian due to nonlinear absorption. As the absorption depends on intensity, the higher the intensity the higher will be the absorption. As a result, higher absorption will occur at the centre of the beam while propagating along the axial direction. Thus, the distribution of intensity as the laser beam exits the material will evolved. Indeed, the exit distribution of the laser energy cannot be specified *a priori*.

The total energy exiting the sample may be determined by substituting equation (4-9) into equation (4-14):

$$E_e = \int_0^{\tau}\int_0^{2\pi}\int_0^{\omega(s)} I_o(z)exp\left(\frac{-9r^2}{2[\omega(s)]^2}-\frac{-2.335t^2}{2[t_{FWHM}]^2}\right)r\cdot dr\cdot d\theta\cdot dt \qquad (4\text{-}15)$$

$$-\int_0^{\tau}\int_0^{l}\int_0^{2\pi}\int_0^{w(l)} \alpha\cdot I(z,r,t)\cdot r\cdot dr\cdot d\theta\cdot dz\cdot dt$$

By solving equation (4-15), the total energy exiting the sample can then be obtained.

4.3 Computational procedure

The nonlinear absorption threshold intensity, the linear, nonlinear and overall absorption coefficients are to be determined from experimental data. A mathematical model using the finite difference method has been developed to solve for these

parameters. The boundary conditions and the computational procedure adopted will be outlined in this section.

4.3.1 Nonlinear absorption threshold intensity

For each experiment, the region of linear absorption and the region of nonlinear absorption were determined. An example of a set of experimental data is shown in Figure 4-5. It can be seen from the figure that in the area near the focal plane there is nonlinear absorption and in the regions far away from the focal plane there is only linear absorption. As shown in Figure 4-5, the transition of absorption from linear to nonlinear is rather distinct and could be observed relatively easily.

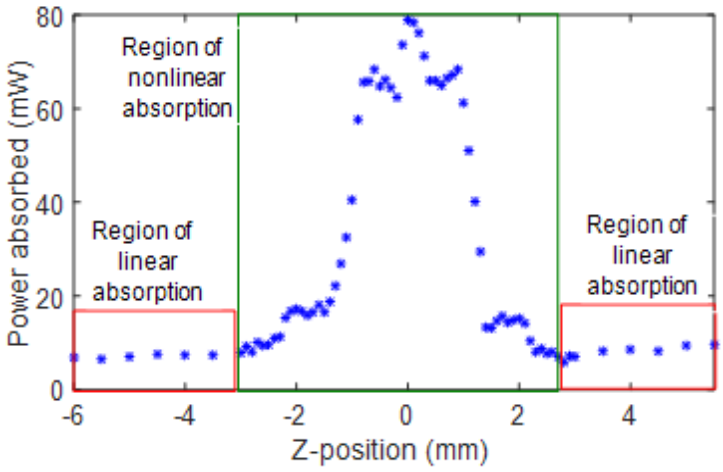

Figure 4-5: Experimental absorption results by 500 μm Gorilla 2320 glass using Z-scan at a laser power of 99.6 mW showing regions of linear and nonlinear absorptions.

To determine the point of transition from linear to nonlinear absorption, the experimental data were numerically differentiated with respect to z-positions (described in Appendix II). Figure 4-6 shows the rate of change of absorption with respect to z-position.

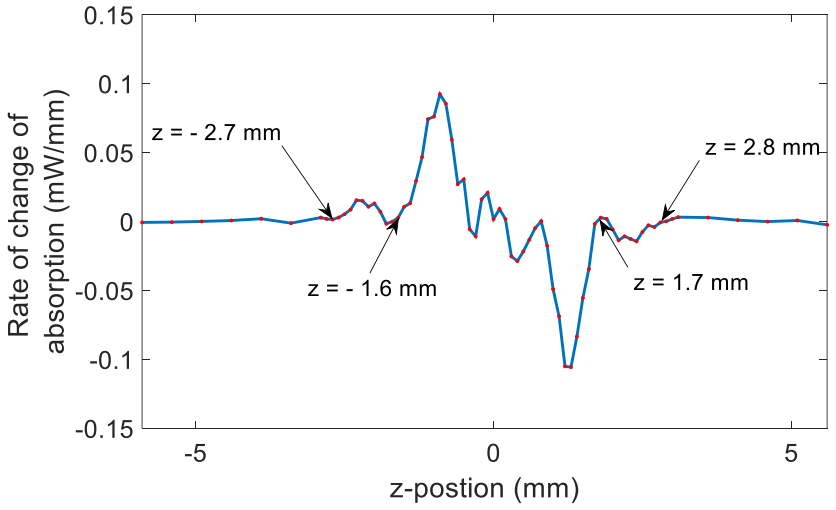

Figure 4-6: Rate of change of absorption with respect to z-position.

From Figure 4-6 it can be observed that at z-positions away from the focal plane, the rate of change of absorption is almost constant and close to zero. In these regions, there is only linear absorption, which is in accordance with the result observed in Figure 4-5. However, as the sample is moved towards the focus from both positive and negative z-directions, the rate of absorption is not constant with respect to z-positions. It can be observed from Figure 4-6 at z = - 2.7 mm and z = 2.8 mm, there is a transition from linear absorption to nonlinear absorption. This can be attributed to the increase in the laser peak intensity as a result of decreasing beam diameter.

The sample experiences laser intensity greater than the nonlinear absorption threshold intensity, resulting in the initiation of nonlinear absorption. As the sample is moved towards the focal plane, between z = -2.8 mm to z = -1.6 mm and z = 2.7 mm to z = 1.7 mm, the rate of change of absorption with respect to z-position is slow. In these regions, the nonlinear absorption results in intensity decay, reducing the intensity to a value less than the nonlinear absorption threshold intensity; as such, most parts of the sample experience linear absorption. However, when the sample is moved even closer to the focal plane, between z > - 1.6 mm and z < 1.7 mm, the rate of absorption with respect to z-position increases, as the peak intensity at the entry surface also increases resulting in high nonlinear absorption. Thus, Figure 4-6 indicates that z = - 2.7 mm and z = 2.8 mm were the points of transition from linear to nonlinear absorption. The peak laser intensity associated with these z-positions were employed as the nonlinear absorption threshold intensity.

The nonlinear absorption threshold intensity can thus be determined using equation (4-9). If 'z' is the location where the transition occurs then the threshold intensity, I_{th} can be defined as

$$I_{th} = \frac{E_s}{\int_0^{\tau}\int_0^{2\pi}\int_0^{\omega(s)} exp\left(\frac{-9r^2}{2[\omega(s)]^2} - \frac{-2.726t^2}{[t_{FWHM}]^2}\right) r \cdot dr \cdot d\theta \cdot dt} \tag{4-16}$$

Where E_s is the pulse energy of the laser, $\omega(s)$is the beam radius at the entry surface of the laser beam which is s-distance away from the focus (s = z – 0.250 mm), which can be calculated using equation (3-1), $t_{FWHM}$is the full-width half-maximum time of the laser which is 130 fs.

Similar calculations were conducted for all other experimental absorption. Table 4-1 tabulates the calculated nonlinear absorption threshold intensities at different power levels.

Table 4-1: Calculated nonlinear absorption threshold intensities at different power levels

S.N.	**Laser power (mW)**	**$I_{th} \times 10^{12}$ (W/cm^2)**	**S.N.**	**Laser power (mW)**	**$I_{th} \times 10^{12}$ (W/cm^2)**
1	21.8	39.22	6	58.2	42.36
2	21.8	45.60	7	99.6	42.62
3	21.8	41.68	8	99.6	41.22
4	58.2	44.24	9	99.6	41.25
5	58.2	41.06			

4.3.2 Determination of the coefficient of linear absorption

For the computation of the coefficient of linear absorption (α_o), z-positions where there is only linear absorption were determined. These points lie in the region of linear absorption which can be seen in Figure 4-5. They have peak laser intensities less than the nonlinear absorption threshold intensity as computed in section 4.3.1 (above). The computational steps for the determination of α_o are:

1. An educated guess of α_o was made which was below the actual value. In the region of linear absorption, there is no nonlinear absorption. Thus the coefficient of nonlinear absorption α_1 was set as 0. As such, the overall

coefficient of absorption, described in equation (4-4), only have the coefficient of linear absorption α_o as the effective coefficient of absorption.

2. For a given experiment, a point is chosen in the region of the linear absorption. The z-position of the point is determined.
3. For numerical calculation, the sample was discretized as elements with respect to the radial direction, thickness direction, and time step. The elemental thickness, the elemental radius, and the elemental time step were defined linearly. An equal number of elements along the thickness direction, the radial direction, and the time step was taken. Initially, the sample was discretized equally into 50 elements along the radial direction (with an elemental size equal to $\omega(z)/50$), the temporal time step (with an elemental time step of 10 fs), and the thickness direction (with an elemental thickness of 10 μm). (Note: the elemental size refinement is subsequently performed using convergence method. Once convergence is obtained, this step can be omitted for the given experiment.)
4. The intensity distribution at the entry surface of the laser beam is determined for the given z-position. This distribution serves as the initial boundary condition for the incoming laser beam.

   For the computation of the intensity distribution of the laser beam at the entry surface, the pulse energy of the incoming laser pulse has to be determined. The pulse energy was determined using the incoming laser power measured during the experiment. Quantranix Integra-C was operated at a pulse

repetition rate of 1 kHz. The laser pulse energy entering the sample surface, E_s, was calculated as

$$E_s = \frac{P}{1000} \tag{4-17}$$

Where P is the average laser power measured during the experiments without the sample.

Based on z-position of the sample surface (distance between the surface sample and the focal plane of the laser beam) in the Z-scan experiment, the radius of the laser beam at the entry surface was calculated using equation (3-1). With the knowledge of the beam radius $\omega(s)$ at the entry surface, the peak intensity $I_o(s)$ of the income laser beam at the surface of the material was calculated by substituting equation (4-17) into equation (4-9).

The intensity distribution at the surface of irradiation using the peak intensity was defined as

$$I(r_j, t_k) = I_o(r,t)exp\left(-\frac{9r_j^2}{2[\omega(s)]^2} - \frac{2.726(t_k^2 - t_o)^2}{[t_{FWHM}]^2}\right) \tag{4-18}$$

Where r_j is the j-th element along the radial direction and t_k is the k-th elemental time step.

5. After the determination of the incoming laser intensity distribution and having an approximation of α_o, intensity distribution within the material was computed using an iterative process. Employing a finite difference method

and using equation (4-11) and equation (4-4), the intensity distribution within the material was computed by solving equation (4-12). The laser intensity within the material, $I(z_i, r_j, t_k)$, was defined as

$$I(z_i, r_j, t_k) = \frac{\mathrm{I}(z_{i-1}, r_j, t_k) \cdot A(z_{i-1}, r_j) - \alpha_o \mathrm{I}(z_{i-1}, r_j, t_k).V(z_i, r_j)}{A(z_{i-1}, r_j)} \quad (4\text{-}19)$$

Where, z_i is the i-th element along the thickness of the sample from the surface, r_j is the j-th element along the radial direction and t_k is the k-th time elemental time step. $I(z_i, r_j, t_k)$ is the intensity associated with z_i, r_j, and t_k; $A(z_i, r_j)$ is an elemental area at position z_i and r_j; and $V(z_i, r_j)$ is the elemental volume at position z_i and r_j. α_o is the coefficient of linear absorption.

6. After the determination of intensities within the sample, the energy exiting the sample was calculated. The energy within the sample at a given z-position within the material can be calculated using equation (4-8). Thus for a sample with 'l' thickness, the total energy exiting the surface can be defined using equation (4-8) as

$$E(l) = \int_0^{\tau} \int_0^{2\pi} \int_0^{\omega(l)} I(z, r, t) \cdot r \cdot dr \cdot d\theta \cdot dt \quad (4\text{-}20)$$

Where $\omega(l)$ is the radius of the beam at *'l'* distance below the surface of irradiation. Integration of equation (4-20) has been performed using a trapezoidal integration method (Appendix III).

7. The absorption was computed as the difference between the incoming laser pulse energy (described by equation (4-17)) and energy calculated at the exit surface in step 6. The computed absorption can be defined as

$$A_c = E_s - E(l) \tag{4-21}$$

Where E_s is the energy at the laser entry surface of the sample and $E(l)$ is the total energy computed at the exit surface of the sample.

8. Steps from 3 to 6 were repeated for all z-positions in the region of linear absorption to determine the absorption at every z-positions in the region of linear absorption. (Note: test of convergence is not necessary for all z-positions; mesh refinement is conducted for selected z-positions, and convergence is verified for these selected z-positions).
9. Five random z-location points in the linear absorption region were selected. For these five points, step 4 to step 8 were repeated, increasing the number of elements along the radial direction, the thickness direction, and the temporal time step. The increment was done by increasing the number of elements by 10.

   The difference in the energy at the entry surface and the energy at the exit surface were monitored at a consecutive increment of the elemental number. Until the difference in the consecutive values at the entry surface and the exit

surface converged to less than 1%, for all five z-locations, the increment by 10 elemental number was continued. If 'n' is the number of elements, the elemental radial distance is determined as $d\omega = \omega(z)/n$, the elemental thickness of the sample is determined as $dz = 500/n\ \mu m$, and elemental temporal time step as $dt = 500/n\ fs$. (Note: if convergence has already been obtained for an experiment there is no need to repeat the convergence test for that experiment. However, while computing for a new experiment, a new convergence test is conducted.)

10. Sum of the squared difference between the experimental absorption result and the computed absorption results for all z-positions in the region of linear absorption was calculated using

$$SD = \sum (A_c - A_e)^2 \tag{4-22}$$

Where A_c is the computed absorption for a given z-position and A_e is the experimentally observed absorption for the z-position.

11. The value of α_o was increased in a small step. Steps 3 through step 10 were then repeated. The increment in the value of α_o was carried out until the sum of the squared difference continually increased. The continual increase in the sum of the squared difference indicated an overestimation of α_o.
12. For the given laser power, the value of α_o with the least sum of the squared difference was determined as the coefficient of linear absorption.

13. Experiments were performed at three power levels, and each power level had 3 experiments. Step 1 through step 12 were repeated for all experimental power values.
14. Mean of all computed values of α_o was defined as the coefficient of linear absorption. The standard deviation of the value of α_o was also calculated.

Table 4-2: Computed coefficients of linear absorption at different power levels

S.N.	**Laser power (mW)**	**α_o (1/cm)**	**S.N.**	**Laser power (mW)**	**α_o (1/cm)**
1	21.8	2.13	6	58.2	1.99
2	21.8	2.02	7	99.6	2.00
3	21.8	2.03	8	99.6	2.06
4	58.2	1.90	9	99.6	2.09
5	58.2	1.91			

4.3.3 Determination of coefficient of nonlinear absorption

In the determination of the coefficient of nonlinear absorption, all the z-position points from the experimental data were used. The nonlinear absorption threshold intensity, determined in section 4.3.1 (above), is employed. The computational procedure for the determination of the coefficient of nonlinear absorption may be summarized as:

1. An educated approximation of the coefficient of nonlinear absorption α_1 was made which was below the actual value.

2. For a given experiment, the nonlinear absorption threshold intensity, determined in section 4.3.1 (above), and the coefficient of linear absorption, determined in section 4.3.2 (above), are first determined. (Note: As there are three experiments each for three power levels, the values of the nonlinear absorption threshold intensity and the coefficient of linear absorption for the respective experiments were employed.)
3. Similar to the determination of the coefficient of linear absorption, for a given experiment, a point is chosen, and its z-position is determined.
4. For numerical calculation, the sample was discretized as elements similar to that described in step 3 in section 4.3.2 (above). Similarly, convergence test was also conducted.
5. The intensity distribution at the entry surface of the laser beam is determined for the chosen z-position. This distribution serves the initial boundary condition for the incoming laser beam. A similar procedure was adopted to determine the intensity distribution at the entry surface as described in step 4 in section 4.3.2 (above).
6. With the previously determined nonlinear absorption threshold intensity and coefficient of linear absorption, and the now determined incoming laser intensity distribution, intensity distribution within the material was computed using an iterative process with an approximation (initial guess) of α_1. Employing a finite difference method, using equation (4-11) and equation (4-4), The intensity distribution within the material was computed by solving

equation (4-12). The laser intensity within the material, $I(z_i, r_j, t_k)$, was defined as

$$I(z_i, r_j, t_k) = \frac{\mathrm{I}(z_{i-1}, r_j, t_k) \cdot A(z_{i-1}, r_j) - \left[\alpha_o + \alpha_1 \cdot \frac{\mathrm{I}(z_{i-1}, r_j, t_k)}{2I_{th}}\right] \mathrm{I}(z_{i-1}, r_j, t_k).V(z_i, r_j)}{A(z_{i-1}, r_j) + \alpha_1 \cdot \frac{\mathrm{I}(z_{i-1}, r_j, t_k)}{2I_{th}}.V(z_i, r_j)} \quad (4\text{-}23)$$

Where, z_i is the i-th element along the thickness of the sample from the surface, r_j is the j-th element along the radial direction and t_k is the k-th elemental time step. $I(z_i, r_j, t_k)$ is the intensity associated with z_i, r_j, and t_k; $A(z_i, r_j)$ is an elemental area at position z_i and r_j; and $V(z_i, r_j)$ is an elemental volume at position z_i and r_j. α_o is the coefficient of linear absorption, α_1 is the coefficient of nonlinear absorption and I_{th} is the nonlinear absorption threshold intensity.

(Note: In equation (4-23), if the value of the coefficient of nonlinear absorption is zero in the region of linear absorption, which will essentially convert equation (4-23) to equation (4-21) for linear absorption region.)

7. After the determination of intensities within the sample, the energy exiting the sample was calculated. The energy exiting the sample can be calculated using step 6 in section 4.3.2 (above).

8. For a given z-position, the total energy absorbed can be determined similarly as described in step 7 in section 4.3.2 (above).
9. Absorptions with respect to all the z-positions were computed using steps 3 to 7 in both regions of linear and nonlinear absorption.
10. For the determination of required elemental sizes, the convergence test was conducted using a procedure similar to that described in step 9 in section 4.3.2 (above).
11. Sum of the squared difference between the computed and the observed experimental data is calculated for the given coefficient of nonlinear absorption α_1, as described in step 10 in section 4.3.2 (above).
12. The value of α_1 was increased in a small step. Step 2 through step 11 were repeated. The increment in the value of α_1 was carried out until the sum of the squared difference continually increased. The continual increase in the sum of the squared difference indicated an overestimation of α_1.
13. For the given laser power, the value of α_1 which resulted in the least sum of the squared difference was determined as the coefficient of nonlinear absorption.
14. Experiments were performed at three power levels, and each power level had 3 experiments. Step 1 through step 11 were repeated for all experimental power values.

The calculated values of the coefficient of nonlinear absorption at different laser power levels are tabulated in Table 4-3.

Table 4-3: Computed coefficients of nonlinear absorption at different power levels

S.N.	Laser power (mW)	α_1 (cm^{-1})	S.N.	Laser power (mW)	α_1 (cm^{-1})
1	21.8	0.00110	6	58.2	0.00110
2	21.8	0.00130	7	99.6	0.00160
3	21.8	0.00130	8	99.6	0.00140
4	58.2	0.00160	9	99.6	0.00140
5	58.2	0.00130			

4.4 Results and discussion

Theoretical and experimental absorptions at different power levels of 21.80 mW, 58.21 mW, and 99.64 mW are shown in Figure 4-7, Figure 4-8 and Figure 4-9 respectively. From the experimental results, it can be observed that the absorption is high near the beam waist (z = 0 mm) with an absorption band increasing with increasing power. Near the focal plane, the laser intensity is high and is above the nonlinear absorption threshold resulting in nonlinear absorption. As the sample is moved away from the focal plane in either direction, nonlinear absorption will decrease with a decrease in laser power intensity. With a sufficient distance from the focal plane, there will only be linear absorption.

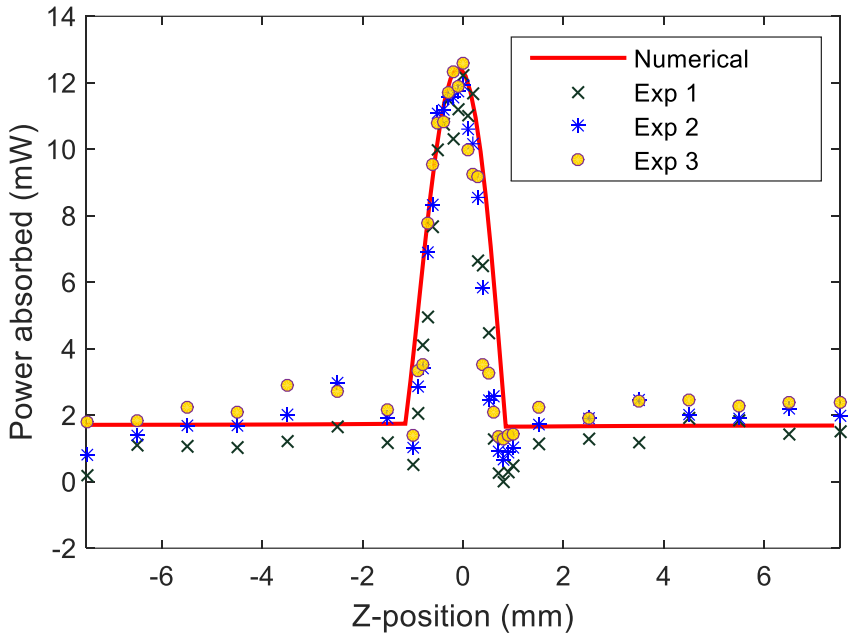

Figure 4-7: Absorption by 500 μm Gorilla 2320 glass using Z-scan at a laser power of 21.8 mW. The peak intensity was 2.13×10^{14} W/cm^2. Exp 1, Exp 2, and Exp 3 are obtained from three different experiments whereas the red solid line is the numerically calculated absorption using average values of the linear and the nonlinear coefficients, and the average value of the nonlinear absorption threshold intensity

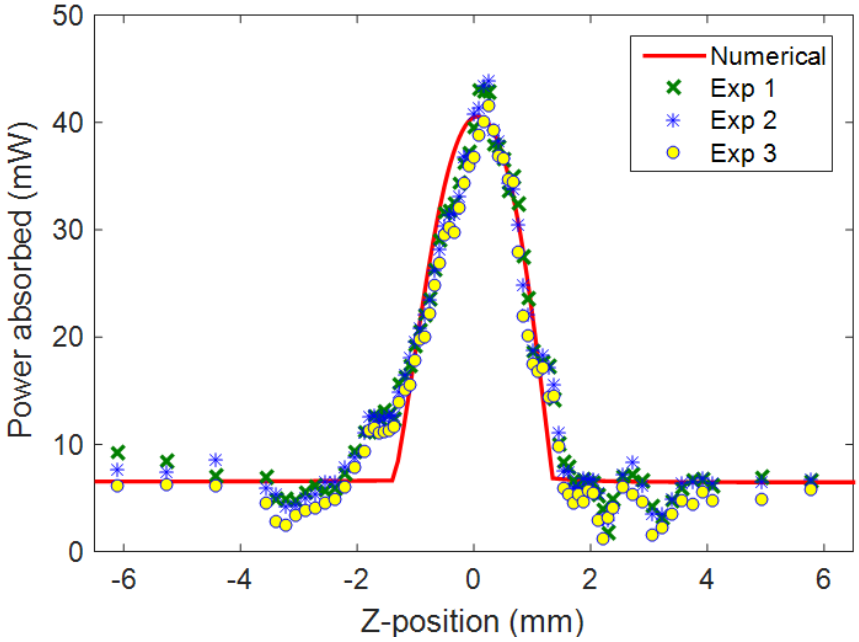

Figure 4-8: Absorption by 500 μm Gorilla 2320 glass using Z-scan at a laser power of 58.2 mW. The peak intensity was 1.34×10^{14} W/cm^2. Exp 1, Exp 2, and Exp 3 are obtained from three different experiments whereas the red solid line is the numerically calculated absorption using average values of the linear and the nonlinear coefficients, and the average value of the nonlinear absorption threshold intensity

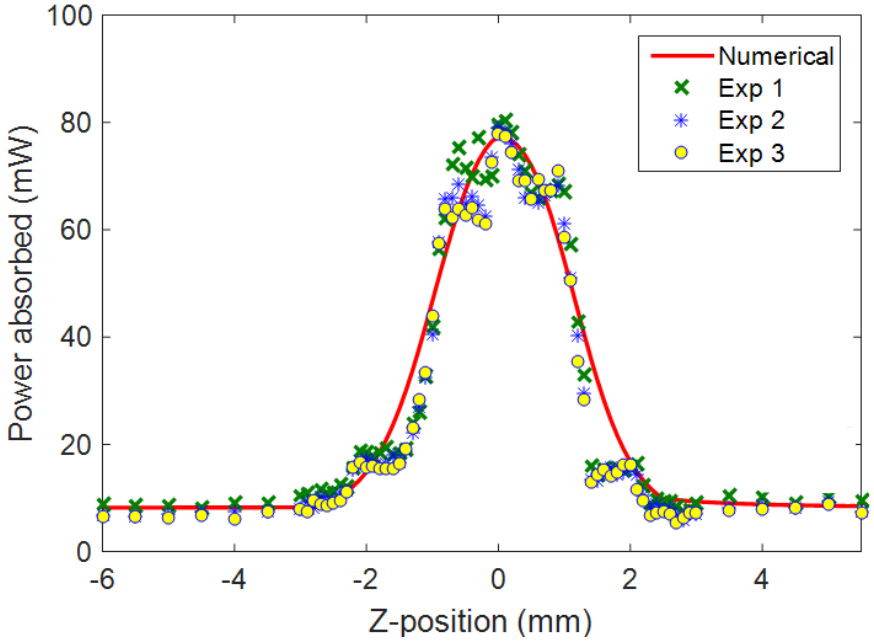

Figure 4-9: Absorption by 500 μm Gorilla 2320 glass using Z-scan at a laser power of 99.6 mW. The peak intensity was 2.13×10^{14} W/cm^2. Exp 1, Exp 2, and Exp 3 are obtained from three different experiments whereas the red solid line is the numerically calculated absorption using average values of the linear and the nonlinear coefficients, and the average value of the nonlinear absorption threshold intensity

Table 4-4 tabulates the calculated values of the linear absorption coefficient, the nonlinear absorption coefficient and the nonlinear absorption threshold intensity of Gorilla Glass 3230 from these set of experiments. From averaging the results obtained from these experiments, the linear absorption coefficient was determined to be 2.01 cm^{-1} ± 0.08 cm^{-1}, the nonlinear absorption threshold intensity was

determined to be 42.1 × 10^{12} W/cm^2 ± 1.89 × 10^{12} W/cm^2 and the coefficient of nonlinear absorption was determined to be 0.0013 cm^{-1} ± 0.0002 cm^{-1}. The uncertainties for linear absorption coefficient and nonlinear absorption threshold intensity are small (less than 5%). The uncertainty of coefficient of nonlinear absorption is larger (15%) but is considered acceptable.

Once the linear and nonlinear absorption coefficients have been computed, the overall absorption coefficient can be obtained as defined by equation (4-4).

Table 4-4: Computed values of the linear absorption coefficient α_o, the nonlinear absorption coefficient α_1, and the nonlinear absorption threshold intensity I_{th}.

S.N.	**Laser Power (mW)**	**α_o (1/cm)**	**α_1(cm^{-1})**	**I_{th} × 10^{12} (W/cm^2)**
1	21.8	2.13	0.00110	39.22
2	21.8	2.02	0.00130	45.60
3	21.8	2.03	0.00130	41.68
4	58.2	1.90	0.00160	44.24
5	58.2	1.91	0.00130	41.06
6	58.2	1.99	0.00110	42.36
7	99.6	2.00	0.00160	42.62
8	99.6	2.06	0.00140	41.22
9	99.6	2.09	0.00140	41.25
Mean		2.01	0.00134	42.14
Standard Deviation		0.08	0.00018	1.88

4.4.1 Existing formulation of absorption coefficient in literature without nonlinear absorption threshold intensity

Existing literature has defined the overall absorption coefficient without considering nonlinear absorption threshold intensity, see equation (1-1) as:

$$\alpha(I) = \alpha + \beta I \tag{1-1}$$

It will be appropriate to examine here if equation (1-1) could equally be utilized to describe the nonlinear absorption phenomenon. This would allow a proper comparison between the proposed absorption coefficient formulation with that in the literature.

A similar procedure is applicable to compute the linear and nonlinear absorption coefficient. The only difference is that (a) the steps for the computation of the nonlinear absorption threshold intensity are no longer necessary, and (b) equation (1-1) will be used for the computation of the overall coefficient of absorption, instead of equation (4-4). For the determination of coefficients of linear and nonlinear absorption as described by equation (1-1), the following steps could be employed:

1. Determination of the coefficient of linear absorption will follow the same procedure as discussed in section 4.3.2 (above). At first, the coefficient of nonlinear absorption is set to be zero, and the computational scheme described in section 4.3.3 (above) is used over the region of linear absorption to determine the value of the coefficient of linear absorption.

2. For the determination of the coefficient of nonlinear absorption, the scheme described in section 4.3.3 (above) will be applicable, apart from one key difference, namely equation (1-1) is used instead of equation (4-4) in the definition of the overall absorption coefficient. As such, the formula for the computation of the intensity distribution within the sample, described in step 5 during the determination of the coefficient of nonlinear absorption, in section 4.3.3 (above), will have to be modified. Using equation (4-11) and equation (1-1), the intensity distribution within the material was computed by solving equation (4-12). As such, the laser intensity within the material, $I(z_i, r_j, t_k)$, will be defined as

$$I(z_i, r_j, t_k) = \frac{\mathrm{I}(z_{i-1}, r_j, t_k) \cdot A(z_{i-1}, r_j) - \left[\alpha + \beta \cdot \frac{\mathrm{I}(z_{i-1}, r_j, t_k)}{2}\right] \mathrm{I}(z_{i-1}, r_j, t_k).V(z_i, r_j)}{A(z_{i-1}, r_j) + \beta \cdot \frac{\mathrm{I}(z_{i-1}, r_j, t_k)}{2}.V(z_i, r_j)} \quad (4\text{-}24)$$

Where, z_i is the i-th element along the thickness of the sample from the surface, r_j is the j-th element along the radial direction and t_k is the k-th time elemental time step. $I(z_i, r_j, t_k)$ is the intensity associated with z_i, r_j, and t_k; $A(z_i, r_j)$ is an elemental area at position z_i and r_j; and $V(z_i, r_j)$ is the elemental volume at position z_i and r_j. α is the coefficient of linear absorption and β is the coefficient of nonlinear absorption.

It should be highlighted that due to the absence of nonlinear absorption threshold intensity, the nonlinear absorption coefficient will be active throughout the calculation, even in the region of linear absorption.

With absorption by 500 μm Gorilla 2320 glass using Z-scan at a laser power of 21.8 mW as an example, Figure 4-10 shows that using equation (1-1) will result in a rather poor agreement in the absorption behaviour between experimental observations and the line of best fit obtained from numerical calculation. Similar poor agreements are obtained for other experimental conditions.

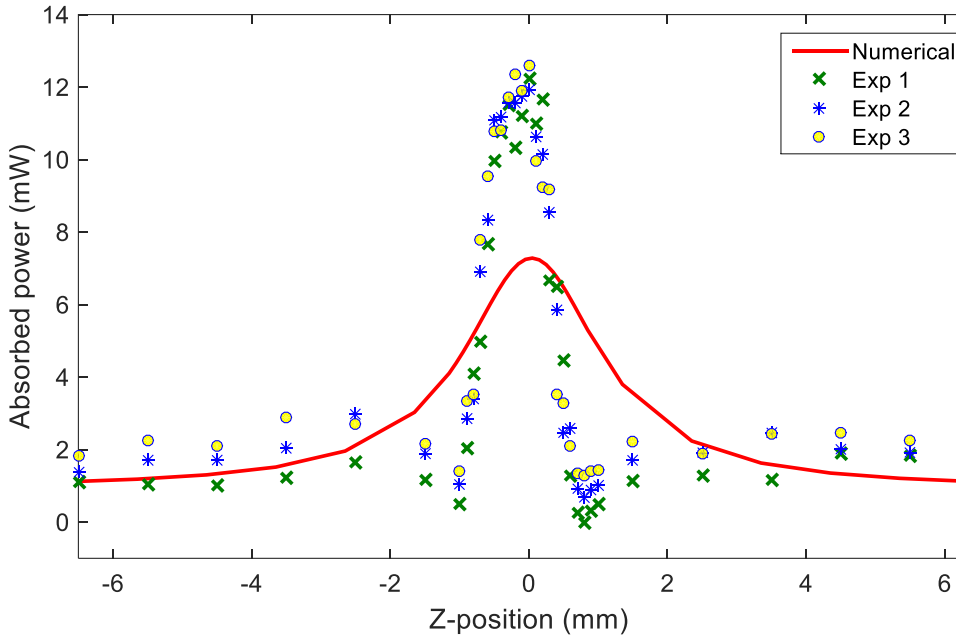

Figure 4-10: Absorption by 500 μm Gorilla 2320 glass using Z-scan at a laser power of 21.6 mW. The peak intensity was 2.13×10^{14} W/cm^2. Exp 1, Exp 2, and Exp 3 are obtained from three different experiments whereas the red solid line is

the numerically calculated absorption (line of best fit) based on equation (1-1) without consideration for nonlinear absorption threshold intensity.

Although both the linear coefficient of absorption α and nonlinear coefficient of absorption β can be determined, namely 2.01 cm^{-1} and 90.1×10^{-9} cm/W respectively, the poor fitting of the line of best fit to the experimental results indicates that these values will describe poorly the actual absorption.

Instead of using the line of best fit, an alternative is to match the maximum absorption value between experimental observations and numerical calculations, see Figure 4-11. Through this matching, the linear coefficient of absorption α and nonlinear coefficient of absorption β can also be determined, namely 2.01 cm^{-1} and 152.3 cm/W respectively. However, similarly to the line of best fit method, the agreement between calculated and experimental values are poor. Thus, the obtained absorption coefficients will poorly describe the experimental absorption.

These results elucidated the deficiencies of the existing formulation for nonlinear absorption. The nonlinear absorption coefficient has a different unit from that of the linear absorption coefficient, and thus there is a lack of consistency. More importantly, without the nonlinear absorption threshold intensity, the equation in the existing literature, namely equation (1-1), indicates that there will always be nonlinear absorption at any laser power intensity; this is not exactly valid at low laser power intensity. Without considering the nonlinear absorption threshold intensity,

the analysis presented here indicates that it is not possible to obtain meaningful absorption coefficients to describe well the experimental observations.

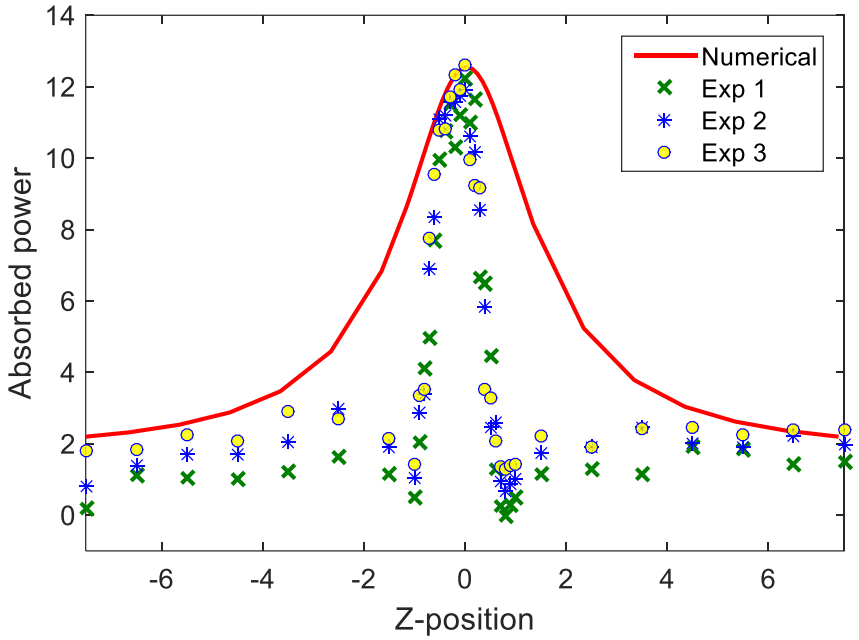

Figure 4-11: Absorption by 500 μm Gorilla 2320 glass using Z-scan at laser power of 21.6 mW. The peak intensity was 2.13×10^{14} W/cm^2. Exp 1, Exp 2, and Exp 3 are obtained from three different experiments whereas the red solid line is the numerically calculated absorption by matching of the maximum absorption values between experimental observations and numerical calculations based on equation (1-1) without consideration for nonlinear absorption threshold intensity.

4.4.2 Rayleigh length and sample thickness

In the literature [10], a sample is considered as a thin sample if its thickness is less than the Rayleigh length. Rayleigh length is given as [1]

$$z_R = \frac{\pi \omega_o^2}{\lambda} \tag{4-25}$$

Where ω_o is the laser beam radius at the focal plane and $\boldsymbol{\lambda}$ is the laser wavelength.

The sample thickness in the experiments is 500 μm, and the system Rayleigh length is calculated to be 890 μm using equation (4-25). As such, the sample will be classified as a thin sample. The associated implicit assumptions are that the laser power profile remains constant as the laser traverse the sample and that only one single value of overall absorption coefficient can be employed for the sample.

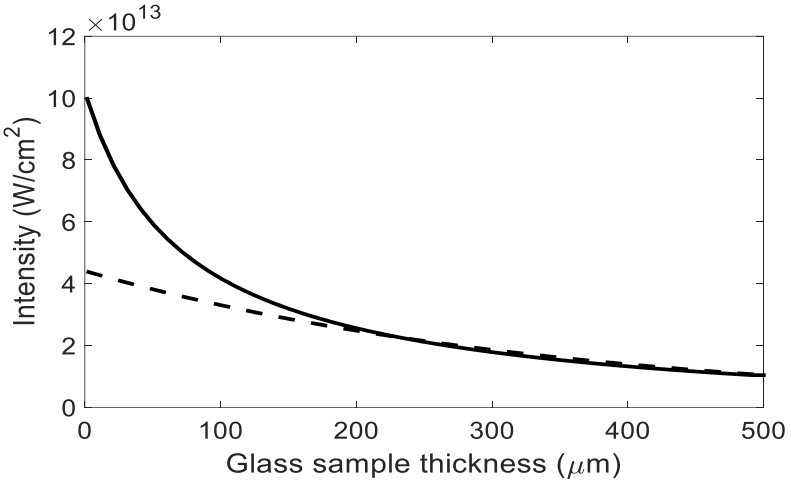

Figure 4-12: Intensity in the axial direction of laser propagation with maximum temporal peak intensity when the laser is focused at the centre of glass (z = 0 mm). Input power is 21.6 mW. The dotted line shows the intensity variation vs thickness for linear absorption only to give the same intensity value at the exit surface of the glass, indicating that there was only linear absorption for thickness greater than 220 μm.

With the proposed formulation here, the solid line in Figure 4-12 shows the intensity profile computed within the sample at the axial line of beam propagation, with the laser beam focused at the centre (interior) of the sample with a laser power of 21.6 mW. There is nonlinear and rapid decay of the laser intensity as the laser propagated through the medium. At a depth of 220 μm from the entry surface, the intensity has already decreased significantly, and is below the nonlinear absorption threshold intensity. Subsequently, as the laser travels further into the medium, there will be linear absorption and without any significant nonlinear absorption. To better elucidate this, the dotted line is the intensity within the sample assuming only linear absorption resulting in the same exit intensity.

This demonstrates that even for this "thin" sample, the absorption at different depths of the sample differs significantly, and one overall absorption coefficient will not be sufficient to describe the absorption phenomenon.

4.4.3 Intensity profiles of the laser beam within the material

The effect of intensity decay within the material on the intensity profile evolution of the laser beam within the material, and thus the change in intensity profile when the laser beam exits the material, has not been studied.

Figure 4-13 shows the temporal and radial profile of the laser beam at the entry surface and at the exit surface of the sample. The initial laser intensity distribution

profile was Gaussian in both radial direction and temporal time step, and thus the laser intensity distribution profile at the entry surface will be Gaussian.

However, the intensity distribution profile at the exit surface, because of absorption, will not have a Gaussian distribution. A Gaussian fit, with the least square method, has been computed for the exit intensity distribution profile. Figure 4-14 compares the intensity distribution profile at the exit surface with the Gaussian fit. The intensity distribution profile was observed not to follow a Gaussian distribution in both radial direction and temporal time step.

Figure 4-14 shows that the actual intensity distribution has a lower peak than that for a Gaussian distribution. This can be attributed to nonlinear absorption. When the laser is propagating through the sample, there is high nonlinear absorption for high laser power intensity exceeding the nonlinear absorption threshold intensity. Around the peak intensity, the laser power intensity is the greatest, and thus the highest power absorption. With this higher absorption at the centre as compared to radial distance further away from the peak, the peak intensity will be depressed much faster. Thus, the exit profile laser intensity will have a lower peak intensity compared to the assumed Gaussian distribution.

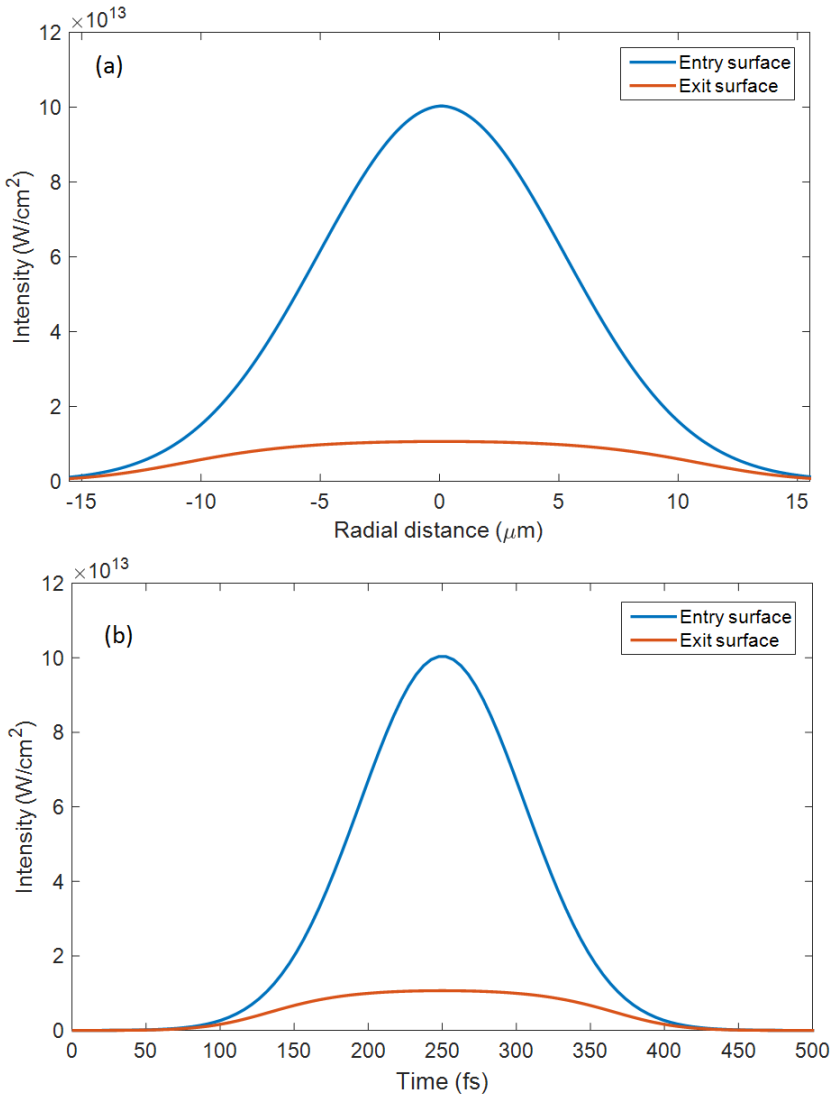

Figure 4-13: Intensity distribution profile of the laser beam at the entry surface and the exit surface of the laser beam (a) radial direction (b) temporal time step

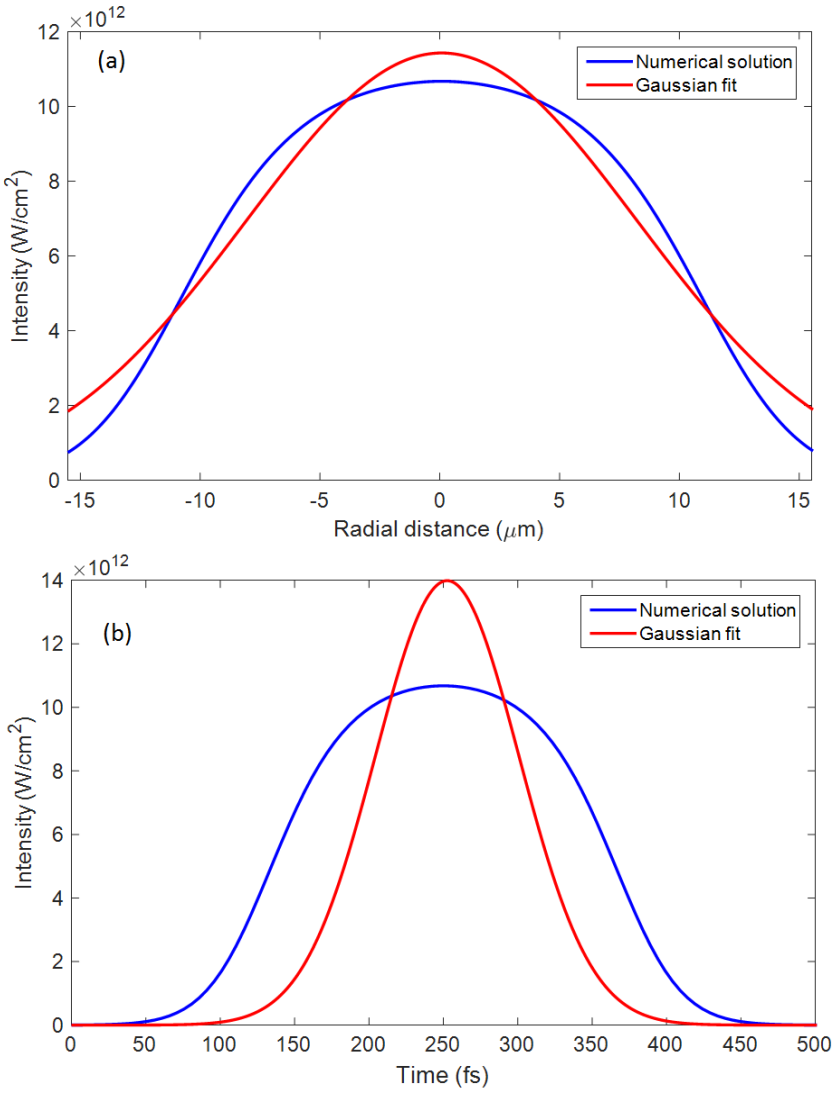

Figure 4-14: Intensity distribution profile of the laser beam at the exit surface of the laser beam with Gaussian fits (a) radial direction (b) temporal time step

As such, these analyses demonstrate that it is rather inappropriate to classify the sample as “thin” or “thick” based on Rayleigh length, with the associated different behaviours assumed between “thin” and “thick” samples. Even for a “thin” sample

investigated here, one overall absorption coefficient is not sufficient to describe the absorption behaviour; in addition, the laser intensity profile will evolve and will not remain constant (as assumed for a "thin" sample") as the laser beam traverse the medium.

4.5 Summary

In this chapter, the nonlinear absorption of Gorilla Glass 2320 was theoretically and experimentally studied. A new absorption equation has been formulated, with the introduction of a nonlinear absorption threshold intensity to take into consideration the transition from linear to nonlinear absorption. With this formulation, both linear and non-linear coefficients of absorption will have the same and consistent unit.

Subsequently, by correlation with experimental results, the linear coefficient of absorption, the nonlinear coefficient of absorption and the nonlinear absorption threshold intensity were determined. It is further elucidated that without the nonlinear absorption threshold intensity, the existing absorption coefficient formulation will not be able to describe the non-linear absorption behaviour.

In addition, it is demonfstrated that the Rayleigh length for the classification of a "thin" or "thick" sample is rather inappropriate. The samples used in this investigation are "thin" as it is less than the Rayleigh length. However, absorption behaviour at different thickness locations of the sample is rather different, and that most of the energy of the laser beam is absorbed near the entry surface. In addition,

the laser power distribution changes as it traverses the sample, and the initial Gaussian distribution of the laser power will not remain as Gaussian.

Chapter 5: Laser-induced plasma during femtosecond laser irradiation

5.1 Introduction

The short-pulsed lasers have high peak intensities. The high intensity leads to the ablation of material. The ejected material will interact with the incoming laser beam with high intensity or electromagnetic strength to create plasma. As discussed in the literature in section 2.6 (above), plasma can be induced by a nanosecond laser, a picosecond laser, or a femtosecond laser. For a nanosecond or picosecond laser pulse, the interaction is complex [75] as the laser-induced plasma has enough time to grow. However, a femtosecond laser pulse has very little time to the plasma to grow. Due to the shorter pulse duration of a femtosecond laser compared to other lasers, a femtosecond laser has higher efficiency of turning ejected fumes into plasma [76]. This leads to the formation of well-defined plasma even with lower pulse energy. The femtosecond laser-induced plasma is well-defined although it has very little time to grow.

Different studies on the laser-induced plasma in aluminium (at λ = 780 nm) [76], silicon (at λ = 616 nm) [105], lithium manganese oxide ($LiMn_2O_4$) (at λ = 248 nm) [106], and copper (at λ = 800 nm) [107] have been reported in the literature. Spectrometric plasma analysis on metals has been presented in [115]. These materials were opaque for the laser wavelength used. However, the study on laser-induced plasma in a transparent material through direct observation, in particular the effect of the laser-induced plasma during the Z-scan analysis, seems to be lacking.

In this investigation, the laser-induced plasma during the laser irradiation by Quantronix Integra-C 1.0 laser amplifier system on Gorilla Glass 2320 will be studied. Investigations has been conducted at a laser wavelength of 795 nm. At 795 nm, Gorilla Glass 2320 is transparent. High-speed imaging has been employed for the investigation of the laser induced plasma on Gorilla Glass 2320. Investigation of plasma formation for Gorilla Glass 2320 would provide insight into laser material interaction with a transparent material. Moreover, plasma formation at different Z-positions in the Z-scan technique has been studied. This would give insight into the effect of the laser-plasma on the Z-scan analysis. Study on the plasma time duration has been conducted.

5.2 Plasma imaging

During femtosecond laser irradiation, well-defined plasma with high energy electrons and ions is formed. The laser-induced plasma can be visually observed during femtosecond laser irradiation. Quantronix Integra-C 1.0 laser amplifier system at a central frequency of 795 nm with a repetition rate of 1 kHz has been employed for laser irradiation. In this section, the method employed for the observation of plasma during femtosecond laser irradiation will be discussed.

The high-speed camera deployed for the observation of plasma, Photron SA5, uses a complementary metal-oxide semiconductor (CMOS) as a photosensor. The spectral response of the CMOS sensor is shown in Figure 3-3. The solid black line in Figure 3-3 is the spectral response of the sensor over the spectral range from 400

nm to 1100 nm. Figure 3-3shows that the CMOS sensor is highly sensitive around the central wavelength of the laser system, i.e. λ = 795 nm.

Figure 5-1 shows six consecutive images, captured by the high-speed camera at a frame rate of 60 frames per second (fps) with a shutter speed of 1/60 second. The occurrence of laser illumination is indicated by the presence of glare. It is first observed in Figure 5-1(b) at 16.667 ms, and subsequently from Figure 5-1 (c) – (f). The glare is due to the scattering of the laser beam which is then captured by the camera. The images were taken without any optical filters. As the laser beam is of high peak intensity, even a small fraction of the reflected laser beam when focused on the photosensor can permanently damage the pixels array of the sensor. To avoid damaging the CMOS sensor, an optical filter has been employed.

5.2.1 Optical filter selection

From Figure 5-1, it was observed that the images obtained were not sharp due to laser beam scattering, with the possibility of damage to the CMOS sensor without the use of a filter. As there are different filters for different spectral cut-off, cut-on or band-pass operations, the choice of the type of filter and the spectral band to be filtered should be considered carefully. Ideally, the filter should only filter out the laser wavelength and would allow other wavelengths of light to pass through. In doing so, the possibility of damage to the CMOS sensor will be mitigated and a clear image of plasma can be obtained without the interference of the laser beam.

For the choice of filter, the following considerations were made:

1. The optical filter should block any wavelength close to the central laser wavelength.
2. All the other wavelengths other than the wavelengths around the central laser wavelength should pass through the filter.
3. The spectral transmission response of the filter beyond the central laser wavelength should be good.

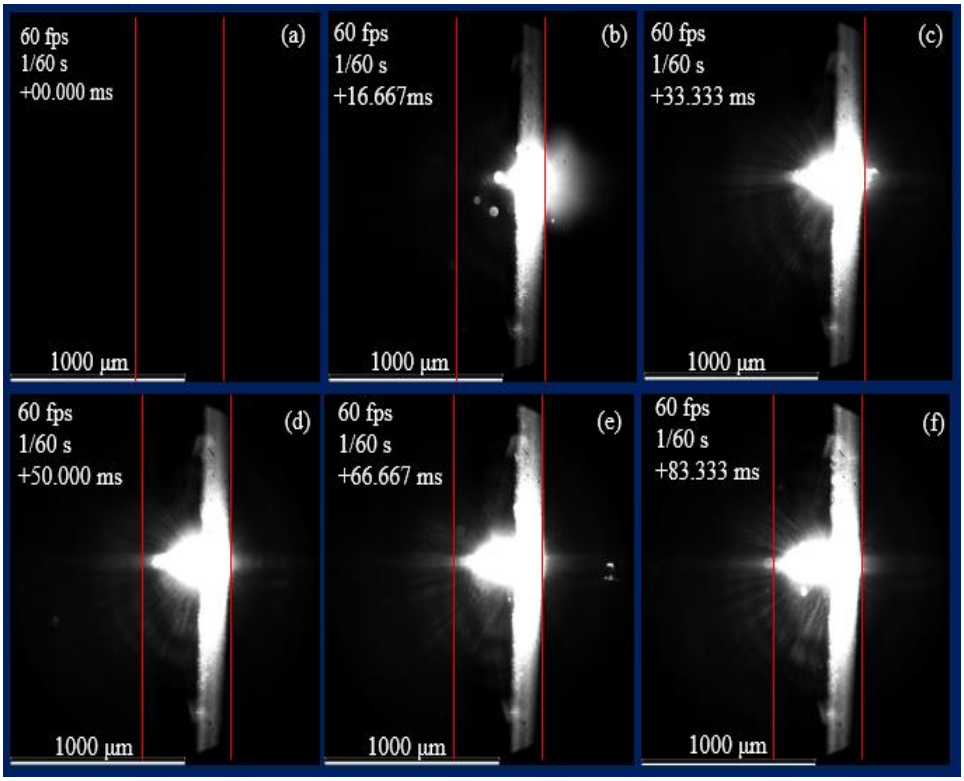

Figure 5-1: Consecutive images of laser irradiation captured at a frame rate of 60 fps and shutter speed of 1/60 s without any optical filter. The laser is operated at a repetition rate of 1kHz with an average power of 102.05 mW. First laser irradiation is observed in time 16.667 ms in frame (b). Red-line denotes the sample surfaces. The laser is irradiated from the surface on the right.

It was difficult to have a filter that would satisfy all the above-mentioned considerations. Indeed, it is a challenge to find a filter which will only filter out the wavelengths around the laser central wavelength. A compromise is to conduct (a) an experiment with a cut-on filter that filter out the central wavelength and all wavelengths below it, and (b) then repeat the same experiment with a cut-off filter that filter out the central wavelength and all wavelengths above it. These two separate experiments in combination will provide the necessary information on plasma formation.

Thus, for the experiments, two separate filters were chosen; one cut-off filter and one cut-on filter. The choice of cut-off wavelength and cut-on wavelength for the filters were made such that the cut-on/cut-off wavelengths were as close to the central laser wavelength as possible. This ensured that for the cut-off filter, almost all the light below the central laser wavelength during the experiment will be captured by the high-speed camera. Similarly, for a cut-on filter, this will ensured that almost all the light above the central laser wavelength during the experiment will be captured. Thus, a cut-off filter with a cut-off wavelength of 750 nm (Thorlabs part number FESH0750) and a cut-on filter with a cut-on wavelength of 850 nm (Thorlabs part number FELH0850) were employed.

Figure 5-2(a) the spectral response of the cut-on filter, FELH0850 and, Figure 5-2(b) shows the spectral response of the cut-off filter, FESH0750. It can be observed from the figure that the cut-off and the cut-on characteristics of the filters are sharp at the cut-off and the cut-on wavelengths, with almost 100% transmission in the

transmission region. The cut-on wavelength of FELH0850 and the cut-off wavelength of FESH0750 are close to the laser central wavelength of 795 nm (55 nm and 45 nm from the laser's central wavelength respectively).

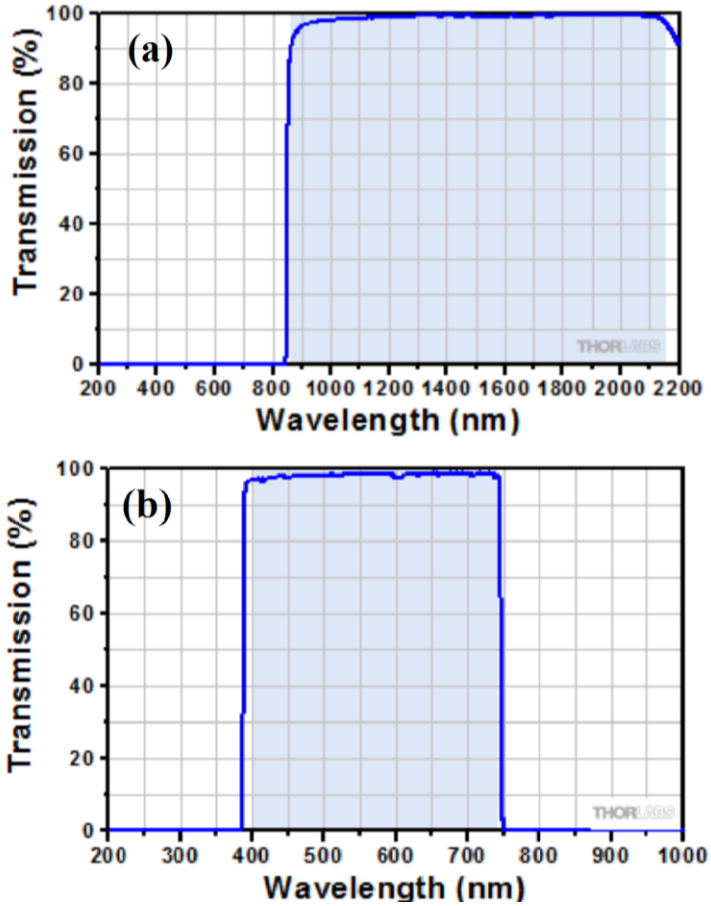

Figure 5-2: Spectral response of (a) FELH0850 (cut-on filter with cut-on wavelength at 850 nm) (b) FLSH0750 (cut-off filter with a cut-off wavelength of 750 nm) (as provided by the supplier)

However, if during plasma formation, photons of a wavelength which lie between the 750 nm to 850 nm are emitted, the information will be lost. As it is a narrow bandwidth, this trade-off should be acceptable.

Figure 5-3 shows the consecutive images obtained during laser illumination using FELH0850 cut-on filter. The average laser power during irradiation was 102.05 mW with a repetition rate of 1 kHz. Other than employing the cut-on filter, the images in Figure 5-3 were obtained with the same condition as imaging without the filter (as shown in Figure 5-1), only in this case. The images in Figure 5-3 are images captured during active laser irradiation. It can be observed that no image is produced using the cut-on filter. This signifies that there are insufficient (and thus negligible) photon energy to form a captured image above the 850 nm wavelength during laser irradiation.

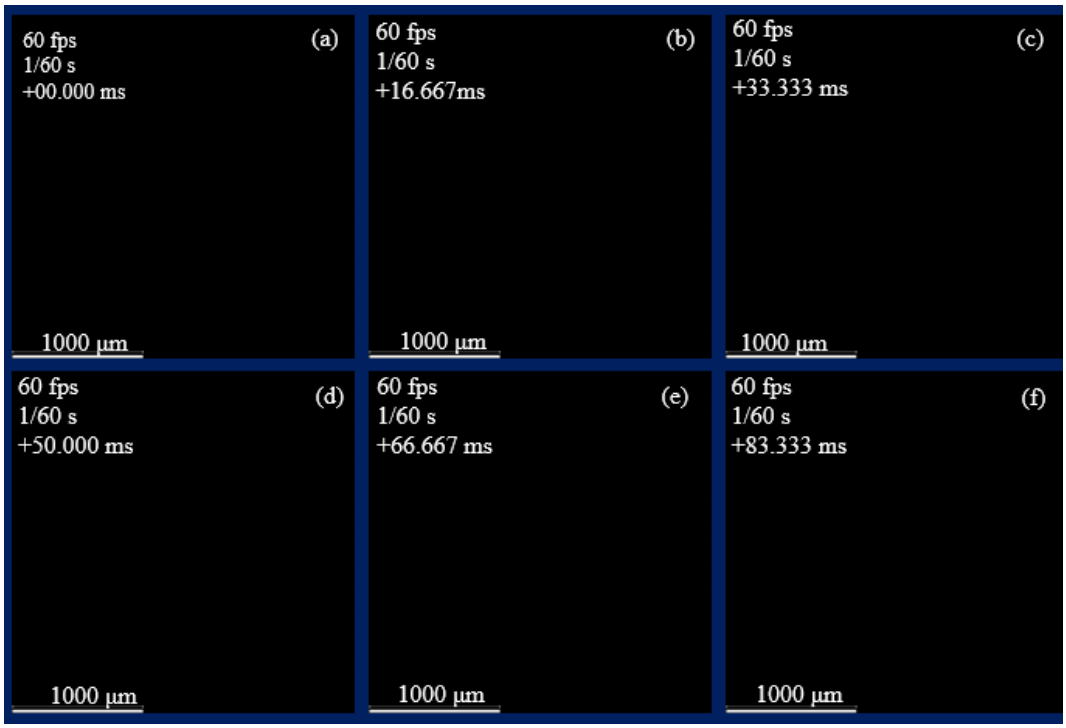

Figure 5-3: Consecutive images of laser irradiation captured at a frame rate of 60 fps and shutter speed of 1/60 s using FELH0850 (cut-on filter with cut-on wavelength at 850 nm). The laser is operated at a repetition rate of 1kHz with an average power of 102.05 mW.

Figure 5-4 shows the consecutive images obtained during laser illumination using FESH0750 cut-off filter. The average laser power of the laser beam was 102.05 mW with a repetition rate of 1 kHz, the same conditions used in previous imaging. The images are captured at 60 fps with a shutter speed of 1/60 s.

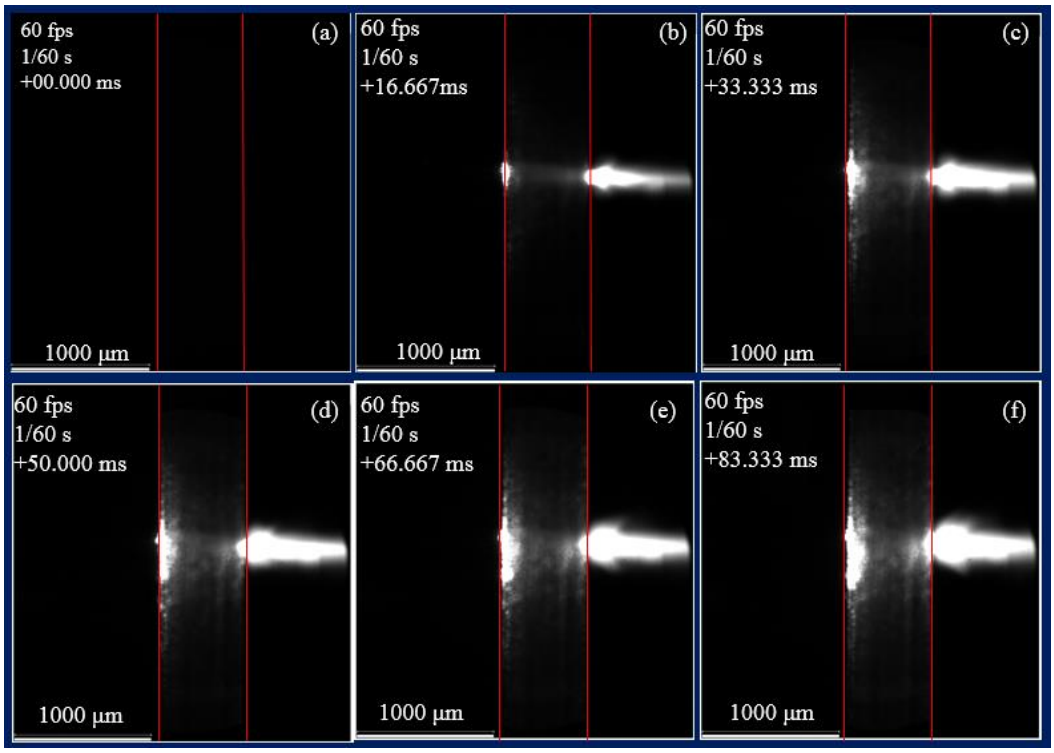

Figure 5-4: Consecutive images of laser irradiation captured at a frame rate of 60 fps and shutter speed of 1/60 s using FLSH0750 (cut-off filter with a cut-off wavelength of 750 nm). The laser is operated at a repetition rate of 1kHz with an average power of 102.05 mW. Red-line indicates the sample surfaces. The laser is irradiated from the surface on the right.

Figure 5-4 indicates that with the cut-off filter, the glare observed during imaging without any filter (as in Figure 5-1) was eliminated. Absence of glare means that no photons of wavelength close to the laser central wavelength are passing through the filter. It assures the protection of the high-speed camera's sensor. In addition, without the scattering photon energy of the laser beam, much sharper images were obtained.

More importantly, Figure 5-3 and Figure 5-4 indicate that predominantly, the photon energy generated during laser irradiation was below the laser central wavelength. As plasma is of high energy, this is an expected result as lower wavelength means higher energy. As such, with this observation, all subsequent experiments will only be conducted using the FESH0750 cut-off filter. No further experiments will be conducted using the FELH0850 cut-on filter.

In Figure 5-4, the laser is irradiated from the surface on the right. It can be observed that a trail of plasma can be observed on the right side of the images. In the left surface, at the exit surface of the laser beam, a glow can be observed in images (b) through (f). This glow can be attributed to light scattering from the edge of the glass sample produced during plasma formation. The glow is not the plasma itself.

5.2.2 Plasma observation

In Figure 5-1 and Figure 5-4, images were taken at 60 fps with a shutter speed of 1/60 s. As the repetition rate of the laser is 1 kHz, multiple pulses were captured in a single image.

To have a deduction on the duration of plasma formation, during laser irradiation, images of plasma will be captured by the high-speed camera at different frame rate and different shutter speed. Similarly, FLSH0750 (cut-off filter with a cut-off wavelength of 750 nm) will be used during the high-speed imaging. The laser was focused at the centre of the glass (i.e. z = 0 mm).

Figure 5-5 shows the images captured during laser irradiation on Gorilla Glass 2320 at a camera frame rate of 1000 fps and shutter speed of 1/1000 s. The laser-induced

plasma during laser irradiation can be observed in the figure. The other experimental conditions were the same for the images shown in Figure 5-4.

It can be observed that images of the laser-induced plasma are more prominent in Figure 5-4 compared to images in Figure 5-5. This can be attributed to the repetition rate of the laser and the camera frame rate. As the laser is operated at 1 kHz, while imaging with 60 fps, as in Figure 5-4, on average about 17 pulses are captured for a shutter speed of 1/60 s. However, laser-induced plasma images in Figure 5-5 were capture for an individual pulse as the shutter speed is 1/1,000 s. It should be noted here that once the laser was turn on, all the frames captured images of laser-induced plasma because of the shutter speed matches the laser repetition rate.

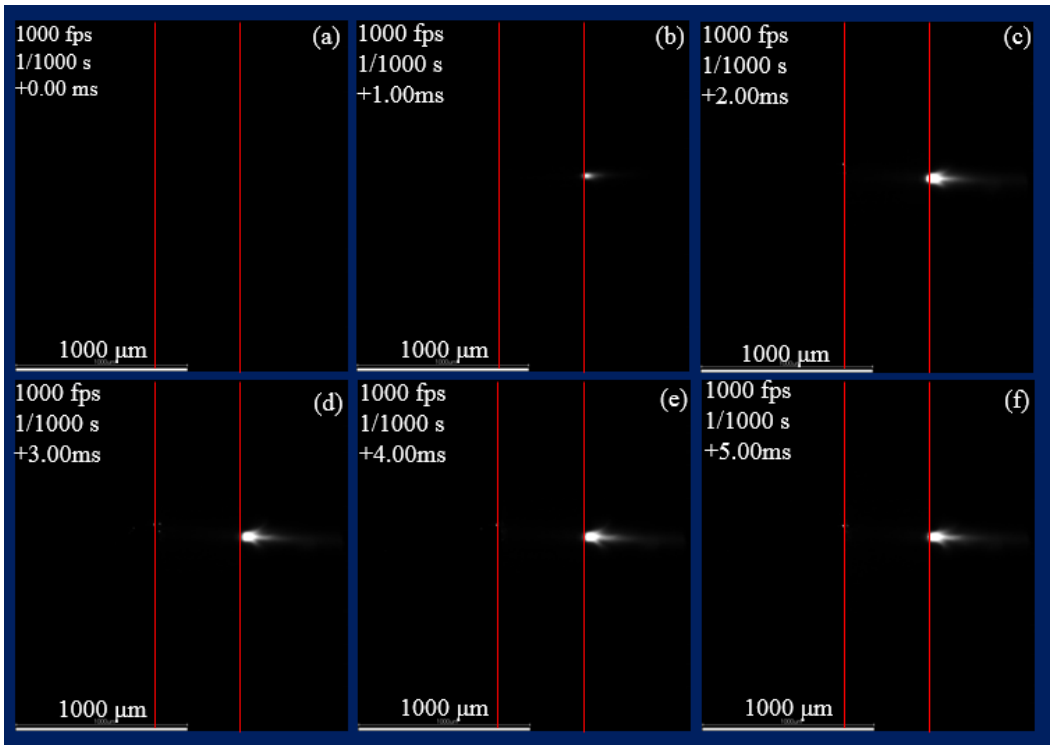

Figure 5-5: Consecutive images of laser irradiation captured at a frame rate of 1000 fps and shutter speed of 1/1000 s using FLSH0750 (cut-off filter with a cut-off wavelength of 750 nm). The laser is operated at a repetition rate of 1kHz with an average power of 102.05 mW. Red-line indicates the sample surfaces. The laser is irradiated from the surface on the right.

In Figure 5-6, high-speed images of the laser-induced plasma were taken at a frame rate of 3,000 fps with a shutter speed of 1/3,000 s. Unlike images in Figure 5-5, images of the laser-induced plasma were not observed in all captured images in Figure 5-6; rather, the plasma can be observed in every third frame because the shutter speed is three times the repetition rate of the laser. As such, laser-induced

plasma is shown in every three consecutive images. This indicates that a single pulse laser at this power has sufficient energy to induce the plasma. However, as plasma cannot be observed in any two consecutive frames, this implies that the plasma decays fast and the laser-induced plasma does not interfere with the next incoming laser pulse (note: 1 frame here is 1/3 the duration between 2 pulses at this frame rate).

It will be of interest to explore the speed of decay of this laser-induced plasma decay. For this purpose, more images of the laser irradiation were captured at a higher frame rates and faster shutter speed.

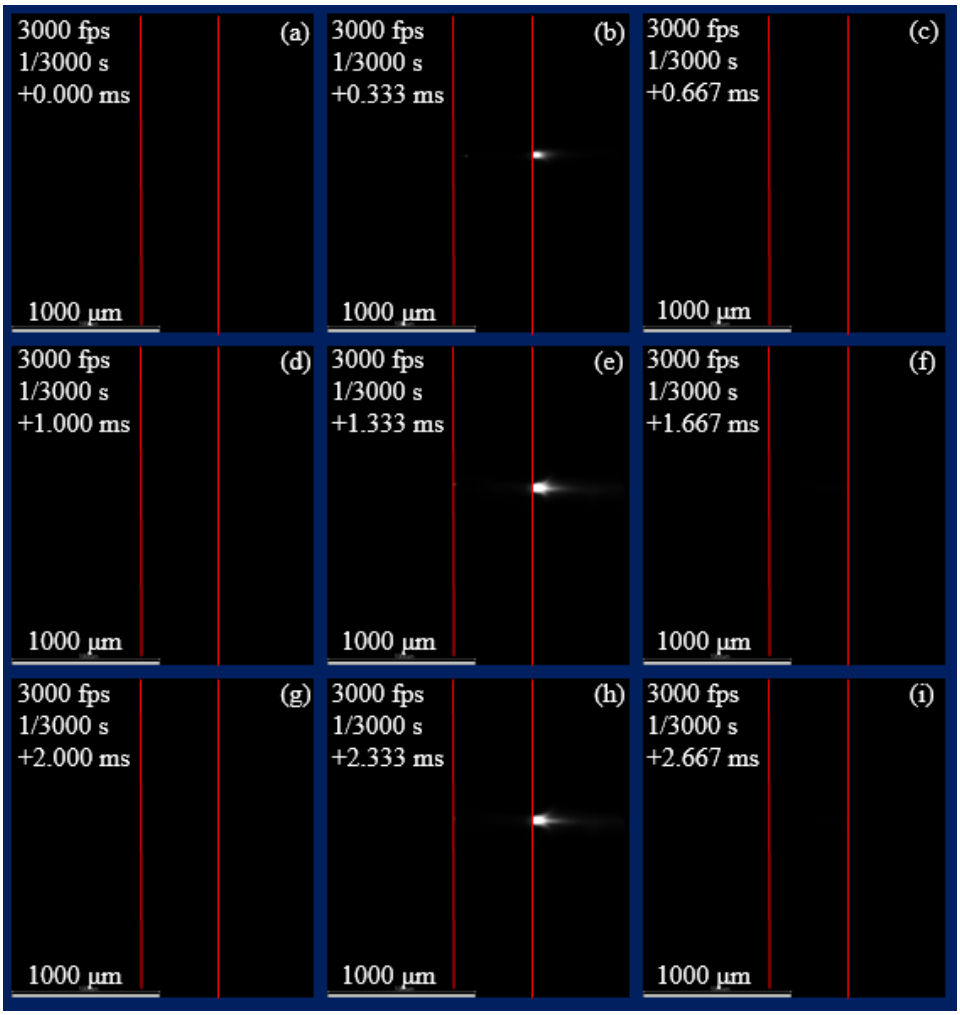

Figure 5-6: Consecutive images of laser irradiation captured at a frame rate of 3,000 fps and shutter speed of 1/3,000 s using FLSH0750 (cut-off filter with a cut-off wavelength of 750 nm). The laser is operated at a repetition rate of 1kHz with an average power of 102.05 mW. Red-line indicates the sample surfaces. The laser is irradiated from the surface on the right.

Figure 5-7 shows the images of the laser-induced plasma in Gorilla Glass 2320 captured at a frame rate of 10,000 fps and shutter speed of 1/10,000 s. As the frame

rate is increased, the number of images captured per pulse increases. Thus, it will not be practical to show all consecutive images. Instead, only consecutive images that provide useful information will be shown in Figure 5-7.

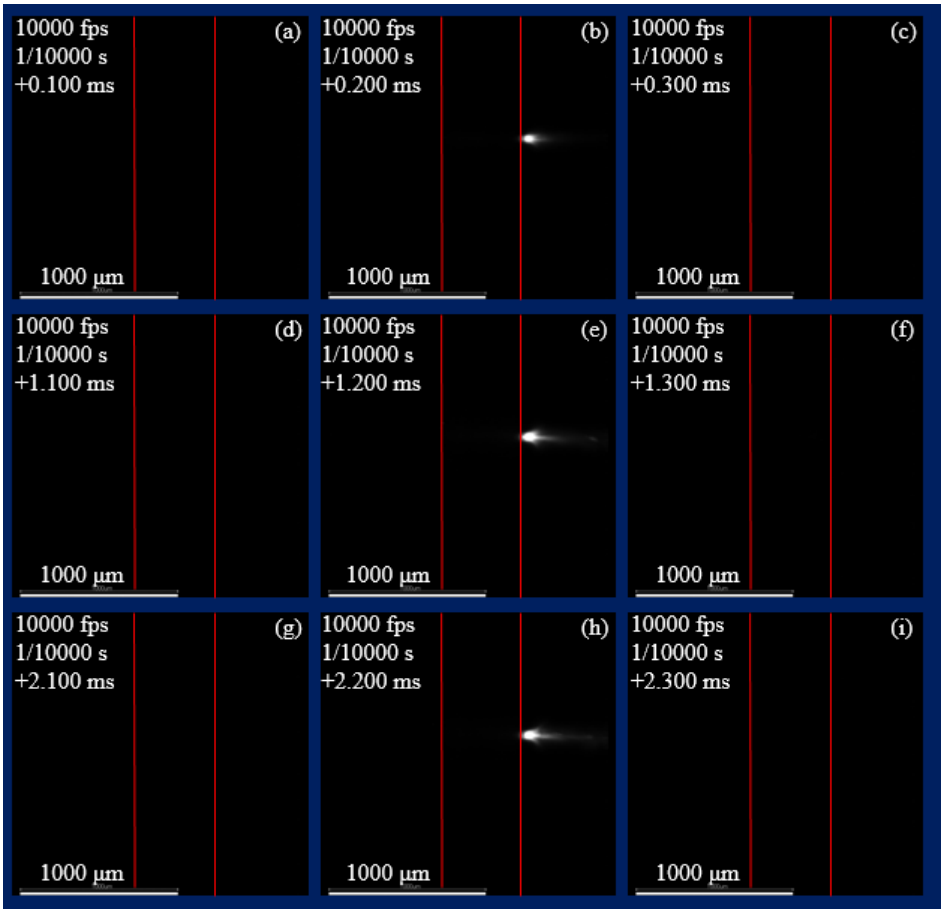

Figure 5-7: Images of laser irradiation captured at a frame rate of 10,000 fps and shutter speed of 1/10,000 s using FLSH0750 (cut-off filter with a cut-off wavelength of 750 nm). The laser is operated at a repetition rate of 1kHz with an average power of 102.05 mW. Red-line indicates the sample surfaces. The laser is irradiated from the surface on the right. (Note: - not all images shown are consecutive.)

For 10,000 fps frame rate, the laser-induced plasma can be observed only once in every tenth frame. Thus, consecutive frames before and after the occurrence of the laser-induced plasma are shown, as the primary concern of this investigation is to determine the plasma decay time. In Figure 5-7, (a), (b) and (c) are consecutive, (d), (e), and (f) are consecutive, and (g), (h) and (i) are consecutive images. If the plasma decay time is to be observed and deduced, it will be observed within the consecutive frames at the occurrence of the laser-induced plasma. However, even with a frame rate of 10,000 fps and a shutter speed of 1/10,000 s, the occurrence of the laser-induced plasma was observed in only one frame per 10 frames.

To further investigate the laser-induced plasma decay, high-speed imaging was carried out for frame rates of 50,000 fps, 300,000 fps and 930,000 fps with their corresponding shutter speed of 1/50,000 s, 1/300,000 s, and 1/930,000 s. Figure 5-8, Figure 5-9 and, Figure 5-10 show the high-speed imaging at frame rates (and shutter speed) of 50,000 fps (1/50,000 s), 300,000 fps (1/300,000s) and 930,000 fps (1/930,000 s). Similar to Figure 5-7, all the images in Figure 5-8, Figure 5-9 and, Figure 5-10 are not consecutive. Only the images before and after the occurrence of the laser-induce plasma are shown.

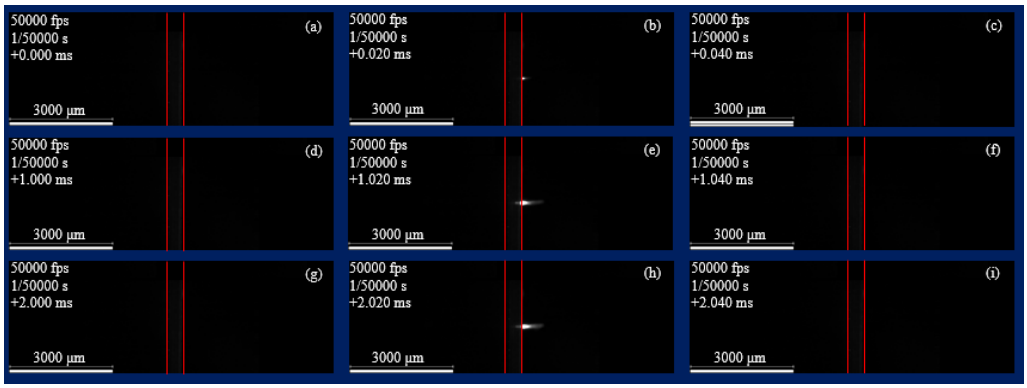

Figure 5-8: Images of laser irradiation captured at a frame rate of 50,000 fps and shutter speed of 1/50,000 s using FLSH0750 (cut-off filter with a cut-off wavelength of 750 nm). The laser is operated at a repetition rate of 1kHz with an average power of 102.05 mW. Red-line indicates the sample surfaces. The laser is irradiated from the surface on the right. Here in this figure, the images are not consecutive.

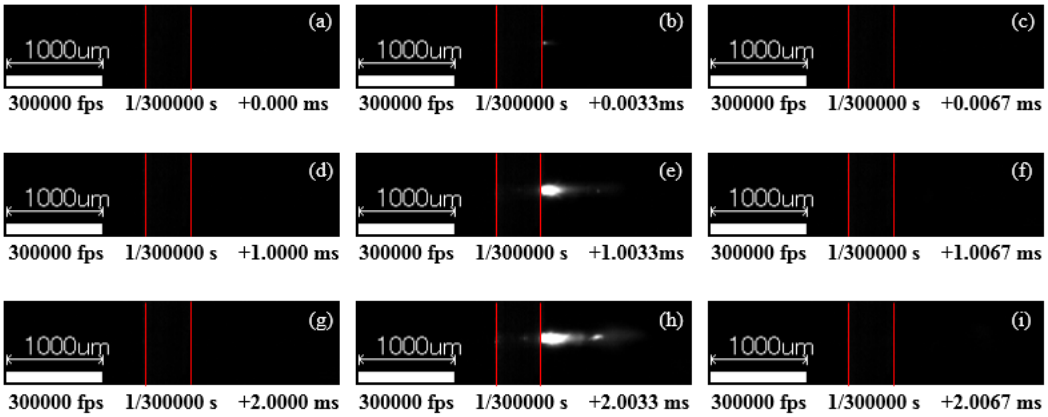

Figure 5-9: Images of laser irradiation captured at a frame rate of 300,000 fps and shutter speed of 1/300,000 s using FLSH0750 (cut-off filter with a cut-on wavelength of 750 nm) The laser is operated at a repetition rate of 1kHz with an average power of 102.05 mW. Red-line indicates the sample surfaces. The laser is irradiated from the surface on the right. (Note: - not all images shown are consecutive.)

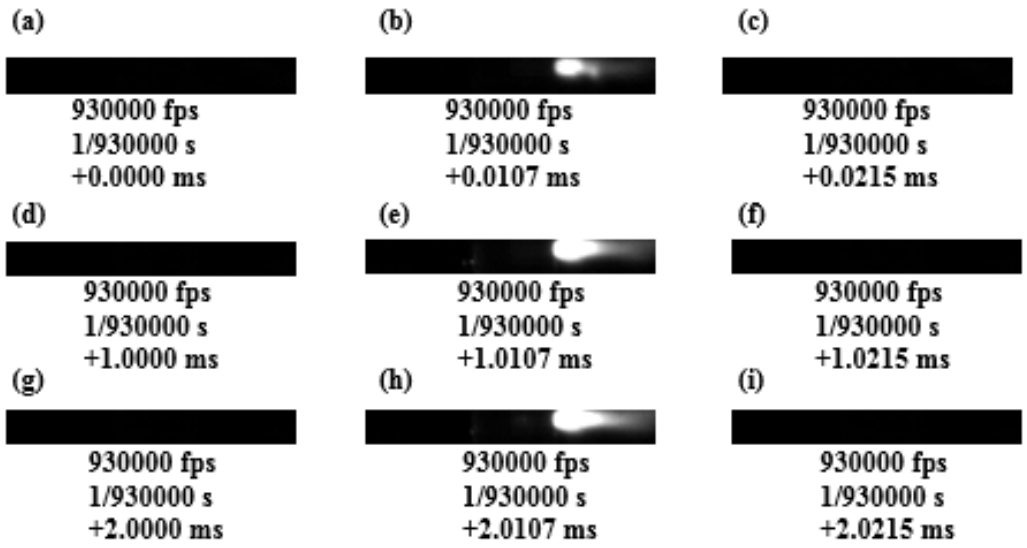

Figure 5-10: Images of laser irradiation captured at a frame rate of 930,000 fps and shutter speed of 1/930,000 s using FLSH0750 (cut-off filter with a cut-off wavelength of 750 nm). The laser is operated at a repetition rate of 1kHz with an average power of 102.05 mW. Red-line indicates the sample surfaces. The laser is irradiated from the surface on the right. (Note: - not all images shown are consecutive.)

From Figure 5-8, Figure 5-9 and, Figure 5-10, it can be observed that even at rather high-speed imaging, the laser induced-plasma cannot be observed in any two consecutive frames. Even for the highest frame rate used, i.e. of 930,000 fps and shutter speed of 1/930,000 s, the laser-induced plasma is observed only once in every 930 frames. From this, it may be deduced that the plasma decay time is less than 1/930 ms. The rather short plasma decay time is reasonable as the energy of the

femtosecond laser is delivered in time less than 1 ps, and plasma is able to sustain only in the presence of a strong electric field.

As such, it may be concluded that the incoming laser beam is not shielded by the plasma generated by the previous pulse. There is this possibility of plasma shielding by the laser-induced plasma occurring within the same given pulse. If plasma is instantaneously induced as soon as the laser beam is irradiated in the material, the tail-end of the incoming pulse might experience plasma shielding. However, with the available experimental set-up, it is not possible to rule out this possibility.

5.3 Plasma formation during Z-scan measurement

Previous section indicates that the laser-induced plasma, if visible, can be observed with any frame rate and shutter speed. To match the laser's repetition rate, the study of laser-induced plasma during the Z-scan measurement was conducted with a frame rate of 1000 fps and a shutter speed of 1/1000 s. This would allow the capturing of an image of the plasma induced by an individual laser pulse.

Two different average power levels were employed to study plasma formation, namely 20.57 mW and 101.65 mW. The z-positions used for the experiments were z = 0 mm (laser beam focused at centre of glass), z = - 0.25 mm (laser beam focused at entry surface), z = 1 mm, (sample's centre 1 mm away from the focus) and z = 2 mm (sample's centre 2 mm away from the focus). Figure 5-11, Figure 5-12, Figure

5-13 and, Figure 5-14 show the high-speed images captured at these various z positions.

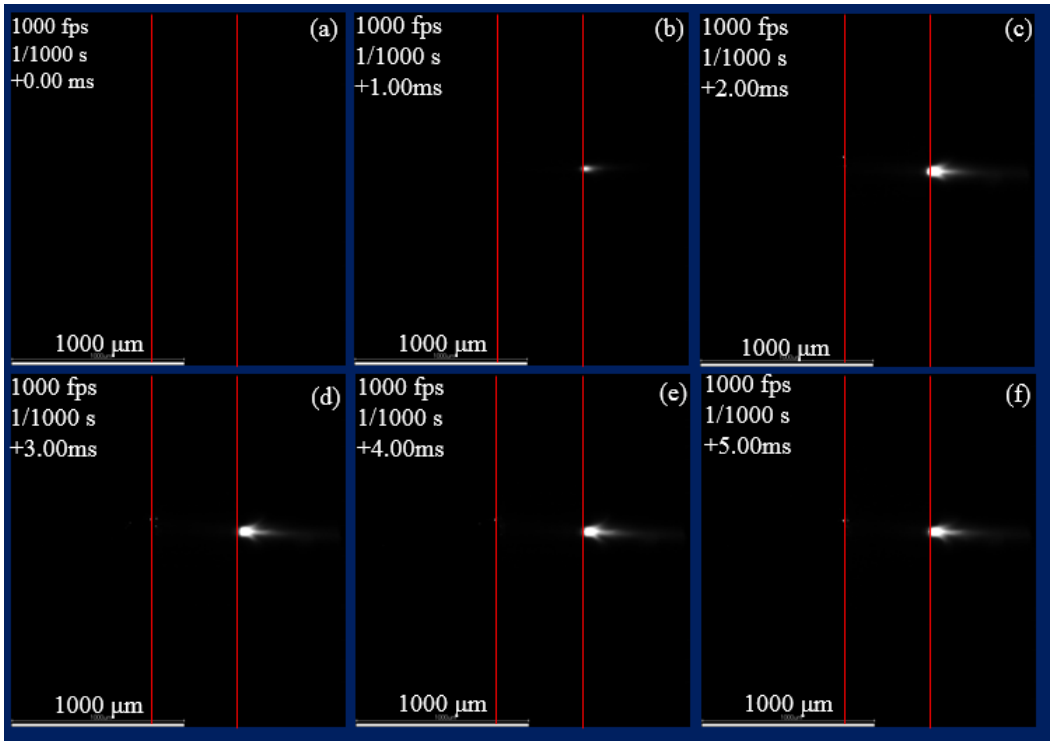

Figure 5-11: Consecutive images of laser irradiation captured at a frame rate of 1,000 fps and shutter speed of 1/1,000 s using FLSH0750 (cut-off filter with a cut-off wavelength of 750 nm) with laser beam focused at the centre of the glass (i.e. z = 0 mm). The laser is operated at a repetition rate of 1kHz with an average power of 101.65 mW. Red-line indicates the sample surfaces. The laser is irradiated from the surface on the right.

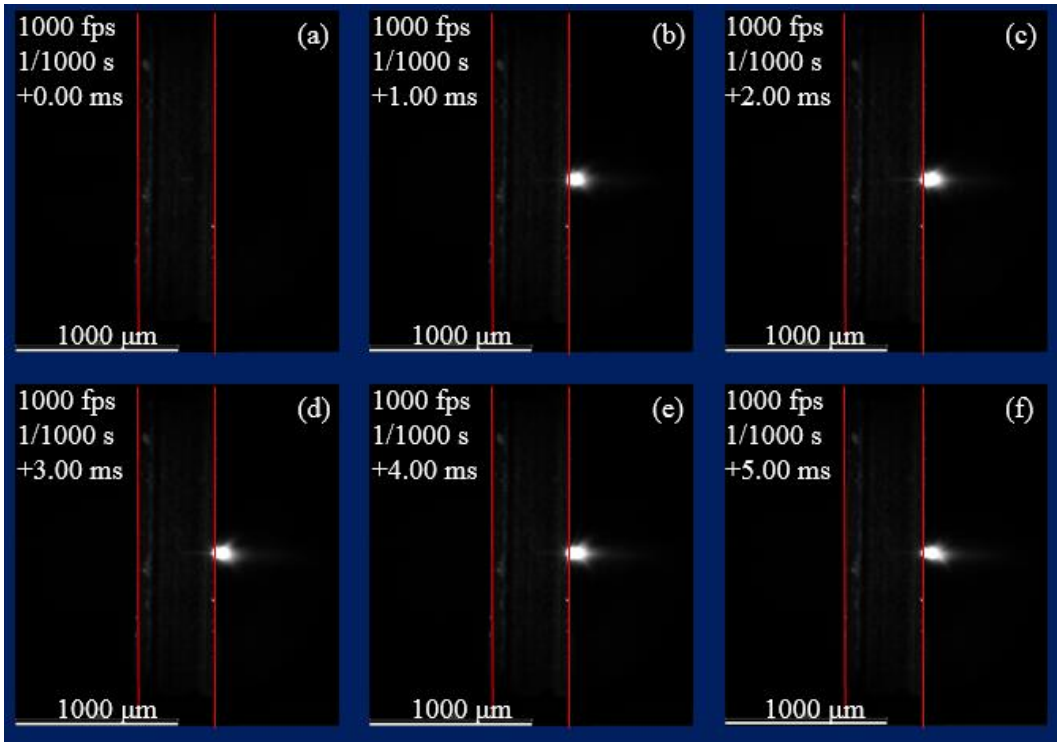

Figure 5-12: Consecutive images of laser irradiation captured at a frame rate of 1,000 fps and shutter speed of 1/1,000 s using FLSH0750 (cut-off filter with a cut-off wavelength of 750 nm) with laser beam focused at the entry surface of the sample (i.e. z = -0.250 mm). The laser is operated at a repetition rate of 1kHz with an average power of 101.65 mW. Red-line indicates the sample surfaces. The laser is irradiated from the surface on the right.

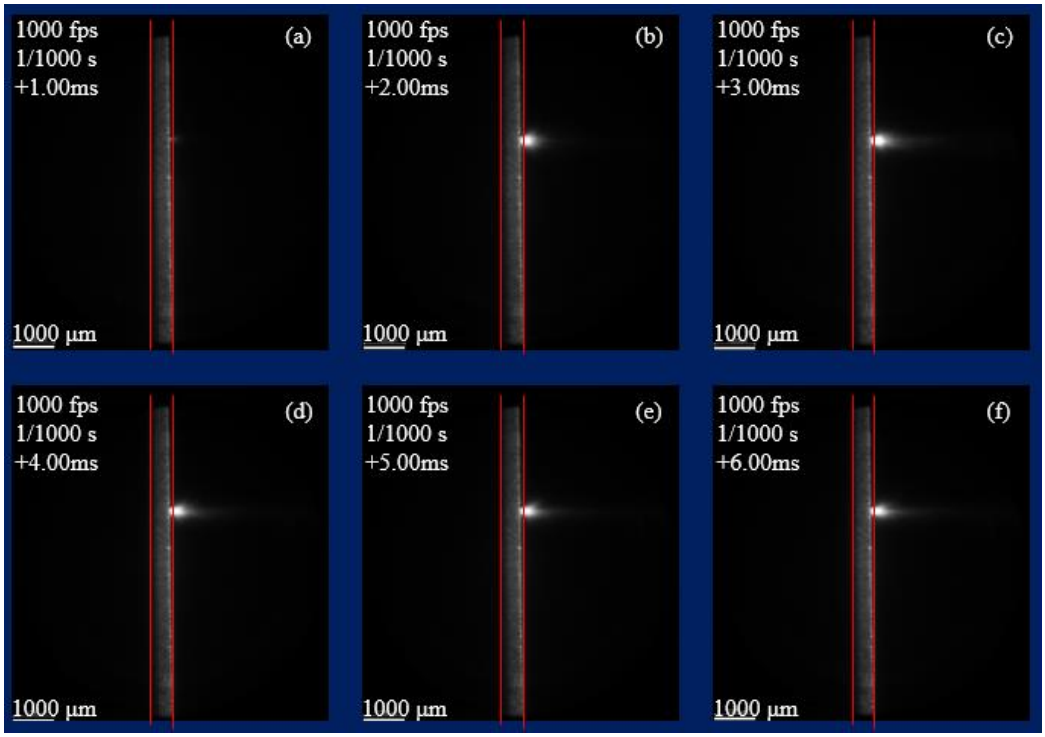

Figure 5-13: Consecutive images of laser irradiation captured at a frame rate of 1,000 fps and shutter speed of 1/1,000 s using FLSH0750 (cut-off filter with a cut-off wavelength of 750 nm) with laser beam focused at z = 1 mm). The laser is operated at a repetition rate of 1kHz with an average power of 101.65 mW. Red-line indicates the sample surfaces. The laser is irradiated from the surface on the right.

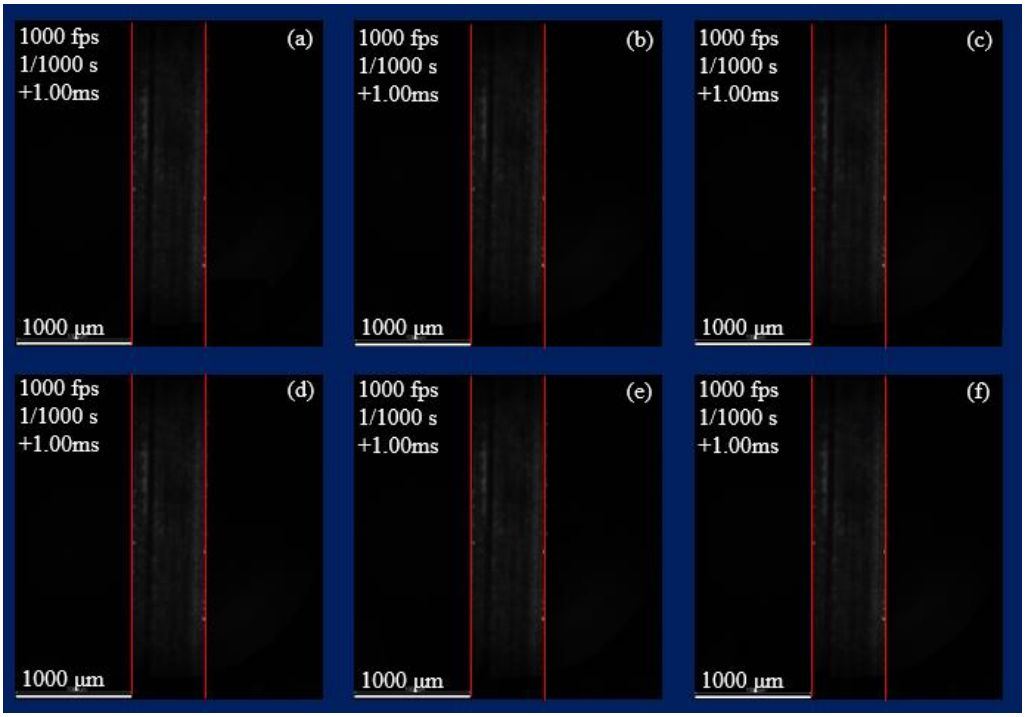

Figure 5-14: Consecutive images of laser irradiation captured at a frame rate of 1,000 fps and shutter speed of 1/1,000 s using FLSH0750 (cut-off filter with a cut-off wavelength of 750 nm) with laser beam focused at z = 2 mm The laser is operated at a repetition rate of 1kHz with an average power of 101.65 mW. Red-line indicates the sample surfaces. The laser is irradiated from the surface on the right.

In Figure 5-11, Figure 5-12 and, Figure 5-13 , laser-induced plasma can be observed. This implies that at z = 0 mm, z = - 0.250 mm and z = 1 mm, the intensity of the laser beam is high enough to ablate the material and the ablated plume is transformed into plasma. However, at z = 2 mm, Figure 5-14 indicates that the laser-induced plasma cannot be observed. In Chapter 4, section 4.4 (above), it was observed that

for laser power level around 100 mW, there is nonlinear absorption; however, the laser power absorbed is not sufficient to ablate the material. Without the ablation of material, there will not be formation of laser-induced plasma.

The same high-speed imaging was carried out for an average laser power of 20.57 mW for the same z-locations. However, there was no evidence of any laser-induced plasma at the given average power level in any of the z-locations. This implies that at an average laser power level of 20.57 mW, the intensity of the incoming laser beam is not sufficient for the ablation of the material and thus the formation of plasma at any z-positions.

5.4 Summary

The laser-induced plasma during femtosecond laser irradiation of Gorilla Glass 2320 was observed using high-speed imaging. To our knowledge, this is the first attempt on direct observation of the laser-induced plasma in a transparent material, Gorilla Glass 2320. Moreover, the effect of the laser-induced plasma during the Z-scan analysis has never been analysed. This investigation is the first attempt to study the effect of the laser-induced plasma during the Z-scan analysis. For the investigation, images of the laser-induced plasma were taken at different frame rates and shutter speeds, using different optical filters.

Two different optical filters, one cut-on and another cut-off, were employed during the high-speed imaging. The cut-on filter has a cut-on wavelength of 850 nm. With

this filter, no laser-induced plasma could be imaged. In contrast, with a cut-off filter with a cut-off wavelength of 750 nm, laser-induced plasma could be observed. This signifies that the photon energy of the laser-induced plasma is below 750 nm, indicating that the plasma is of high energy as expected.

Using the cut-off filter, high-speed images at different frame rates and shutter speeds were taken. It was observed that the laser-induce plasma decays rapidly. Although the exact time of plasma decay could not be ascertained, it was determined to be less than 1/930 ms. Therefore, it can be concluded that for a laser repetition rate of 1 kHz, the laser-induced plasma will not interact with the subsequent incoming laser pulse, and thus no plasma shielding of the subsequent pulse. However, plasma shielding within the same given pulse could not be ruled out.

The laser-induced plasma at different z-locations in Z-scan experiments was observed through high-speed imaging. At high laser power, the laser-induced plasma was observed when the sample was placed near the focal plane of the laser beam. As the sample is moved away from the focal plane, even though the sample is within the nonlinear absorption region, the peak intensity of the laser beam at the sample surface is reduced. This reduced intensity is not sufficient to ablate the material, and thus plasma formation. In contrast, at low laser power, the laser could not induce plasma at any z-locations. This is because at low laser power, the laser beam could not ablate the material. This indicates that the Z-scan experiments for nonlinear characterization would produce more accurate results at lower laser power. The reason is that at low laser power, the losses due to plasma shielding and ablation will

not occur, resulting in more accurate determination of the coefficients of linear and nonlinear absorption.

Chapter 6: Thermal characterization of material during laser irradiation

6.1 Introduction

During laser irradiation of a material, significant energy is absorbed by the material. The total percentage of the incident laser power that was deposited into material had been studied by Tran et al. [77-79]. In copper, silicon and steel, more than 50%, 66.7% and 67% respectively of the total incident laser energy was deposited into the material [77-79]. All the materials investigated were opaque for the central wavelength of the laser used (λ=775 nm).

Ever since the pioneering work of Mansoor Sheik-Bahae et al. [14, 15], the Z-scan technique has been used to characterize the nonlinear characteristics of different materials [25, 28, 30, 33-35, 38-40, 43]. In the study reported in chapter 4, a new method for the computation of the linear and nonlinear absorption coefficients has been proposed with the introduction of the nonlinear absorption threshold intensity. Although verification of the obtained coefficients of absorption was carried out in Chapter 4 using the Z-scan technique, it will be of interest to verify the results obtained independently. This can be achieved by correlating the observed temperature fields to that predicted as a result of the absorbed laser energy during laser irradiation. This will allow an evaluation of the accuracy of the determined values of coefficients of absorption and the nonlinear absorption threshold intensity.

In this investigation, the energy absorbed during laser irradiation by Gorilla Glass 2320, which is transparent at the central laser's wavelength of 795 nm, will be studied through thermal characterization. The thermal energy deposited into the material will be observed using a thermal camera, FLIR® Silver SC5000 Medium Wave Infrared (MWIR). The temperature profile at the surface of the sample at different z-positions was observed during laser irradiation by the Quantranix Integra-C 1.0 laser amplifier system. The experimental procedure for this observation has been discussed previously in section 3.4.2 (above).

A theoretical mathematical model for laser heat absorption and thermal transport as a results of laser irradiation has been developed. The mathematical model was solved using finite element software, COMSOL Multiphysics. Conclusion can be drawn from the comparisons between the observed temperature fields and the simulated temperature fields. The allows an independent evaluation of the determined nonlinear absorption threshold intensity, the coefficient of linear absorption, and the coefficient of nonlinear absorption calculated in chapter 4 (above).

6.2 Theoretical analysis

The mathematical model is modelled using the laser intensity. Followings are the assumptions employed during the analysis:

1. The axis of the laser beam is perpendicular to the surface being irradiated.

2. Thermal properties of Gorilla Glass 2320 are assumed constant, i.e. they do not vary with temperature. All the material properties are as reported at ambient air condition of 25 ^{o}C.
3. The incoming laser beam has Gaussian temporal profile and Gaussian spatial profile, the same assumption as previously reported in section 4.2 (above). The intensity profile of the incoming laser beam irradiated at the surface can be written as described in equation (4-3) as:

$$I_s(r,t) = I_o(z)exp\left(-\frac{r^2}{2\sigma_r^2} - \frac{(\mathrm{t}-t_o)^2}{2\sigma_t^2}\right) \tag{4-3}$$

4. The investigation has been conducted at low average laser power with no ablation and plasma formation as observed in Chapter 5 section 5.3 (above). Thus, phase change and material ablation during laser irradiation can be neglected.

In this chapter, the same z-location approximations have been used as described in section 4-(above) unless specified otherwise.

6.2.1 Governing equation

The second-order parabolic partial differential is used to describe the conductive heat transfer temperature distribution:

$$\rho c_p \frac{\partial T}{\partial t} + \nabla.(-k\,\nabla T) = Q \tag{6-1}$$

Where ρ is the density of the material, c_p is the specific heat capacity of the material at constant pressure, *k* is the thermal conductivity of the material, *T* is the temperature as a function of time, and *Q* is the net heat deposited on the material.

6.2.2 Heat source

The heat source can be approximated as a volumetric heat source:

$$Q = \frac{\partial I}{\partial z} = -\alpha I \tag{6-2}$$

Equation (6-2) is a first-order decay equation which dictates how the intensity (*I*) decreases along the z-direction. The decrease in intensity depends on α, which is the overall absorption coefficient of the material. The overall absorption coefficient of absorption is previously described in section 4.2.1 (above) by equation (4-4) as:

$$\alpha = \begin{cases} \alpha_o & \forall\, I(z,r,t) < I_{th} \\ \alpha_o + \alpha_1 \cdot \dfrac{I(z,r,t)}{I_{th}} & \forall\, I(z,r,t) \geq I_{th} \end{cases} \tag{4-4}$$

Where α_o is the coefficient of linear absorption, α_1 is the coefficient of nonlinear absorption, with the same unit as α_o, and I_{th} is the nonlinear absorption threshold intensity.

As the laser propagates through the material, the laser energy is absorbed by the material. The amount of energy absorbed per elementary volume is defined by equation (6-2). This absorbed energy acts as the heat source for laser heating. It is further noted that the laser beam is a focused laser beam. As such the beam profile

within the material can be modelled using equation (3-1) described in section 3.3.2 (above).

6.2.3 Boundary conditions

The experimental procedure for the direct observation of the laser beam irradiation on Gorilla Glass 2320 is described in Chapter 3, section 3.4.2 (above). As shown in Figure 6-1, the laser is irradiated on surface 5 (shown by the arrow in Figure 6-1), and is 1 mm away from the surface 2 for observing temperature distribution for different z-locations, see section 3.4.2 (above) . The model is constructed to account for these boundary conditions.

In the experiment, the sample geometry is symmetrical about a vertical plane along the propagation direction of the laser beam. The model can be simplified by applying symmetrical boundary conditions to reduce computational time and resources. The symmetrical boundary condition is shown as surface 4 in Figure 6-1.

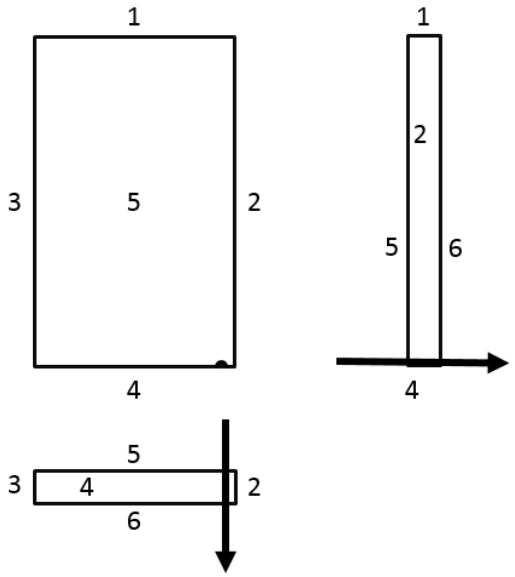

Figure 6-1: Orientation of the sample during laser-material interaction simulation. Numbers provide the references to the specific surfaces. Arrow indicates the location and direction of the laser beam.

As the sample is heated up by laser beam, there is heat exchange between the sample and the environment. There are two significant modes of heat exchanges between the material and the environment, namely radiative heat transfer and convective heat transfer. These two modes of heat transfer are responsible for the loss of energy from the system to the environment. They can be described by:

$$-k\nabla T = \varepsilon\sigma(T_{amb}^4 - T^4) \tag{6-3}$$

$$-k\nabla T = \mathrm{h}(\mathrm{T}_{amb} - \mathrm{T}) \tag{6-4}$$

Equation (6-3) and equation (6-4) describe respectively the radiative and convective heat transfers, where k is the thermal conductivity of the material, $\boldsymbol{\varepsilon}$ is the radiative emissivity of material, σ is the Stefan's Boltzmann Stefan's constant equals to 5.67×10^{-8} W/(m^2 K^4) [111], h is the convective heat coefficient (discussed in Appendix IV), and T_{amb} is the ambient room temperature which is set at 21°C.

For surface 4, there is no heat flux across the surface as it is a plane of symmetry and is internal to the material. As laser irradiation time was short (5 s), there will be hardly any temperature change for surfaces 1 and 3, as they are far away from the laser irradiation location. Most to the heat loss will be through surfaces 5 and 6 due to its large surface areas and proximity to the laser beam. Although there is less heat loss through surface 2 due to its small surface area, at the vicinity of the laser irradiation location, there will be significant temperature increase. Indeed, the temperature profile of surface 2 is to be monitored experimentally by the thermal camera.

As such, for boundary conditions, radiative and the convective heat transfers are applied to 3 surfaces, namely surfaces 2, 5 and 6; constant ambient room temperature (21°C) boundary condition is applied to surfaces 1 and 3.

6.2.4 Meshing and computational time steps

The sample was discretized into elements. 99027 triangular prism elements were used for the discretization of the sample of 5 mm × 2.5 mm × 0.25 mm sample. At the vicinity of the laser irradiation location, much finer mesh was employed, with a maximum elemental size less than 1 μm.

Two computational time steps were used for each pulse repetition, i.e. over a duration of 1 ms. They are (a) 100 time steps of 10 fs each (total duration of 1,000 fs). At 500s, it is at the peak power intensity of the laser pulse. As the femtosecond laser has a single pulse duration of 130fs, these fine time steps will fully encompass the active lasing duration when rapid temperature changes can be expected, and (b) 5 time-steps between 1 ps to 1 ms during passive lasing when rapid temperature changes are not expected. These time steps are repeated over a period of 5 s, i.e. the total laser irradiation time.

6.3 Experimental observations of thermal profiles

The direct observation of the temperature field during laser irradiation was conducted as described in Chapter 3 in section 3.4.2 (above). A schematic diagram of the experimental setup for the observation is shown in Figure 3-2. Experiments were conducted at an average laser power of 20.06 mW. At this laser power, there is no ablation and plasma shielding, as previously discussed in Chapter 5, section 5.3.2 (above). This avoids the complication introduced by energy losses associated with ablation and plasma shielding.

6.3.1 Spatial temperature distribution

The temperature observations were taken in different z-locations. Figure 6-2 shows the temperature distribution at the surface of the glass

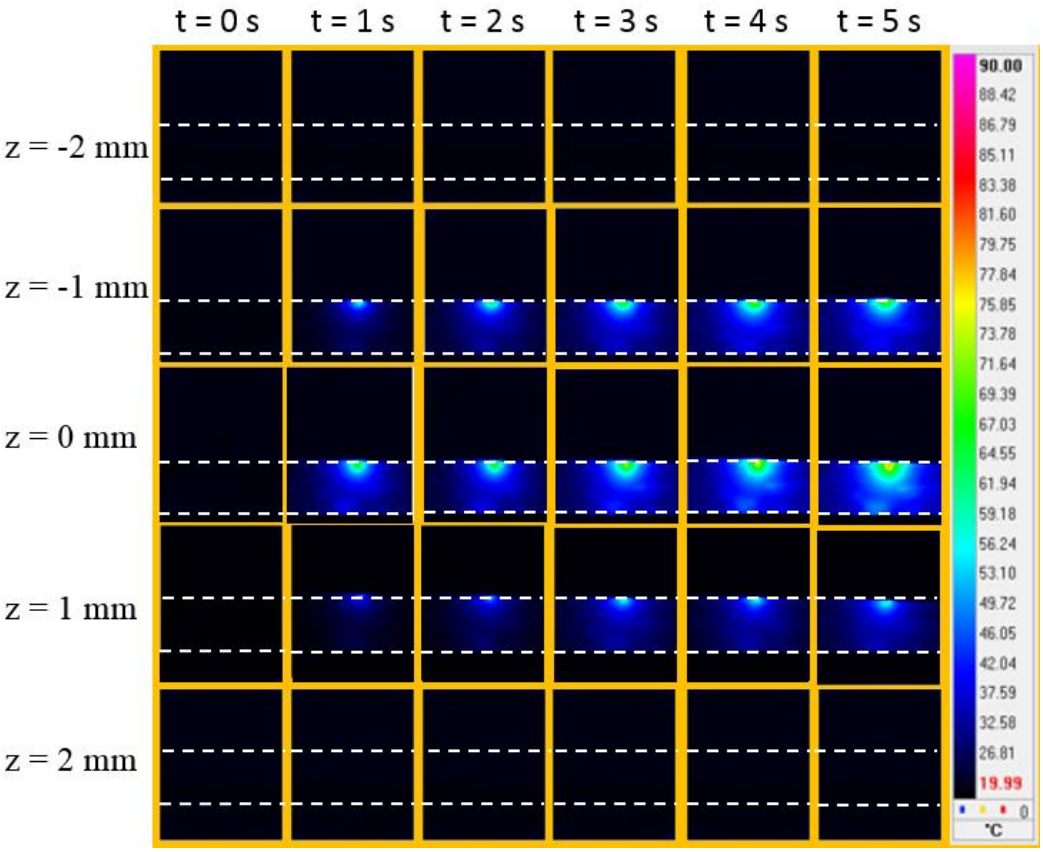

Figure 6-2: Temperature profile distribution at the surface of the glass with z-distance varied from - 2 mm to 2 mm, at 1 s time intervals. The dotted white line shows two surfaces of the glass.

The results in Figure 6-2 are consistent with the results observed on laser power absorption shown in Figure 4-7), indicating that z = - 1 mm, z = 0 mm and z = 1 mm

lie in the region of nonlinear absorption. As a result of nonlinear absorption, these z-locations had higher absorption and thus significant heating of the glass. In contrast, z = - 2 mm and z = 2 mm lie in the region of linear absorption. There was no significant heat absorbed by the material, and thus the lack of thermal footprint at z = - 2 mm and z = 2 mm in Figure 6-2.

For nonlinear absorption, Figure 6-2 indicates that laser heating is similar to a heating source close to the surface. This is consistent with our earlier finding shown in Figure 4-12, that most of the energy is absorbed near the surface of entry of the laser beam. When the high-intensity laser beam experiences nonlinear absorption by the material, its intensity decays quickly. Once the intensity of the laser beam is below the nonlinear absorption threshold intensity, it can only undergo linear absorption, with little heat absorbed and thus little heating.

6.3.2 Temporal temperature distribution

For the analysis of temperature distribution during laser irradiation, four points were chosen on the sample surface, and Figure 6-3 shows a sample result. In Figure 6-3, the points B, C and D are 100 μm away from the centre of the laser irradiation point A. Subsequent analysis of the temporal temperature profile will be carried out using the sample acquired from these four locations.

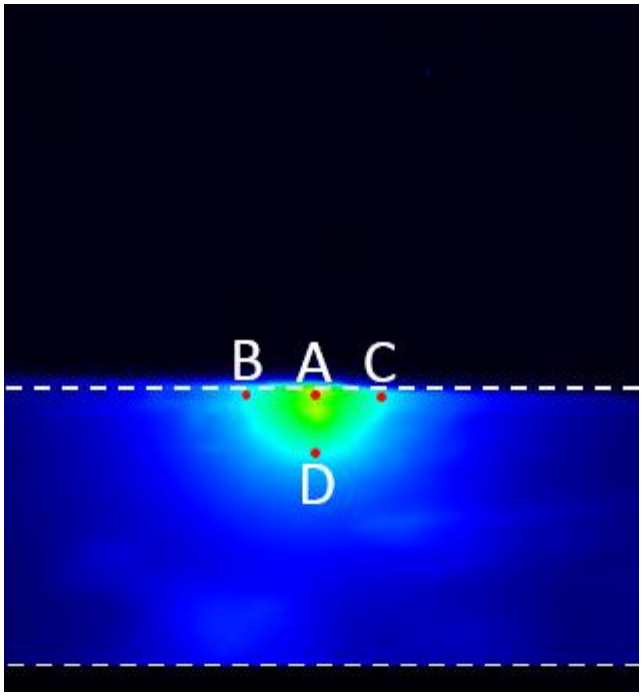

Figure 6-3: The sampling locations for the analysis of temporal temperature profile.

The temporal temperature distribution curve for the aforementioned sampling points was obtained, see Figure 6-4. Figure 6-4 shows that the observed maximum temperature increase is at z = 0 mm. The maximum temperature observed of 68.97 ^{o}C for z = 0 mm is at position A. It should be noted that point A was not the location of the laser irradiation, which was 1 mm away from point A in the direction perpendicular to the plane of the paper. At z = 0 mm, the laser focal plane matches with the central plane of the glass, as such the intensity of the irradiated laser beam is at its maximum. With high-intensity irradiation, there is high absorption as a result of the nonlinear absorption. The absorbed energy is subsequently conducted into the

material as heat, raising its temperature. The temperature readings that can be measured in points A, B, C, and D are in fact the result of the conducted heat from the site of laser irradiation.

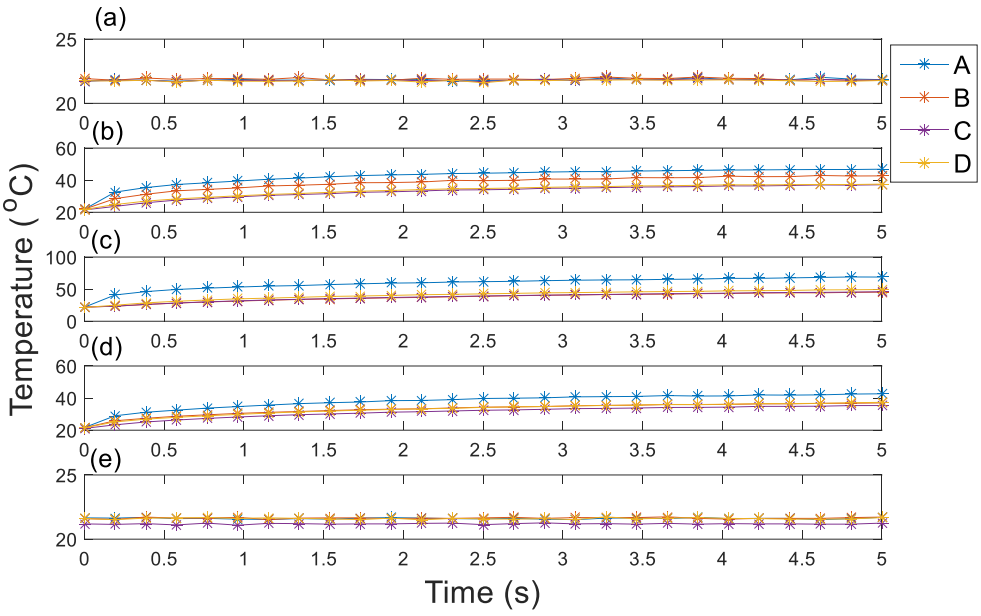

Figure 6-4: Temporal temperature distribution at the surface perpendicular to the surface of laser irradiation for (a) z = - 2 mm, (b) z = - 1 mm (c) z = 0 mm, (d) z = 1 mm and (e) z = 2 mm

A similar rise in the temperature can be observed at these four sampling points at z = -1 mm and at z = 1 mm, see Figure 6-4. The maximum temperature of 44.35 °C and 43.68 °C were observed at the sampling location A for z = - 1 mm and z = 1 mm respectively. The rise in temperature at these z-locations is less than that observed at z = 0 mm. At z = - 1 mm and z = 1 mm, the sample's central plane is ± 1 mm away

from the focal plane of the laser. Comparing to the diameter of the laser beam entering the surface at z = 0 mm, the diameter of the laser beam entering the surface at these z-locations is larger. This results in a decrease in laser intensity at the entry surface. With a decrease in laser intensity, the efficiency of nonlinear absorption decreases. As a result, the heat absorption decreases with an associated decrease in heat conduction into the material. This explains the smaller temperature increase observed at z = - 1 mm and z = 1 mm than at z = 0 mm.

As the z-position is moved further away from the focal plane, i.e. at z = - 2 mm and z = 2 mm in Figure 6-4, no temperature rise can be observed. This is consistent with the observation that as the distance between the sample and the laser focal plane increases, the diameter of the incoming laser beam at the surface of irradiation increases. With an increase in diameter, the intensity decreases. At z = - 2 mm and z = 2 mm, the intensity of the incoming laser beam was less than the nonlinear absorption threshold intensity; this means that there was no nonlinear absorption of the laser beam energy. As such, the only mode of absorption is linear absorption which results in insignificant energy absorption, and negligible temperature rise as shown in Figure 6-4 at z = - 2 mm and z = 2 mm.

All the temporal temperature distributions are consistent with the results obtained in Chapter 4 section 4.4 (above). The temperature distributions obtained at these z-locations confirms that there exists region of linear and region of dominant nonlinear absorption. For the sample presented, in the region of linear absorption, there is insignificant change in temperature within the material. In contrast, in region of

dominant nonlinear absorption, there is a significant increase in temperature. This reaffirms that there exists a threshold intensity below which there is only linear absorption, and above which there is both linear and nonlinear absorption. The temperature profiles observed experimentally provide the justification for the proposed nonlinear absorption intensity threshold.

6.3.3 Simulation of thermal profiles

To simulate the observed temperature profile, numerical simulations were conducted with COMSOL Multiphysics, a finite element software. The mathematical model described in section 6.2 (above) was employed for the computation of the temperature field during laser irradiation. The simulations were carried out for the same average laser power of 20.06 mW for the experimental observations.

For the simulations, the average values of the coefficient of linear absorption, the coefficient of nonlinear absorption, and the nonlinear absorption threshold intensity as calculated in section 4.4 (above) were used, namely α_o = 2.01 cm^{-1}, α_1 = 0.0013 cm^{-1}, and I_{th} = 42.1 × 10^{12} W/cm^2. The absorbed laser power calculated at the various locations is assumed to be the heating source at the corresponding locations. The simulated and corresponding experimental temperature results at different z-locations are presented in Figure 6-5 through Figure 6-9.

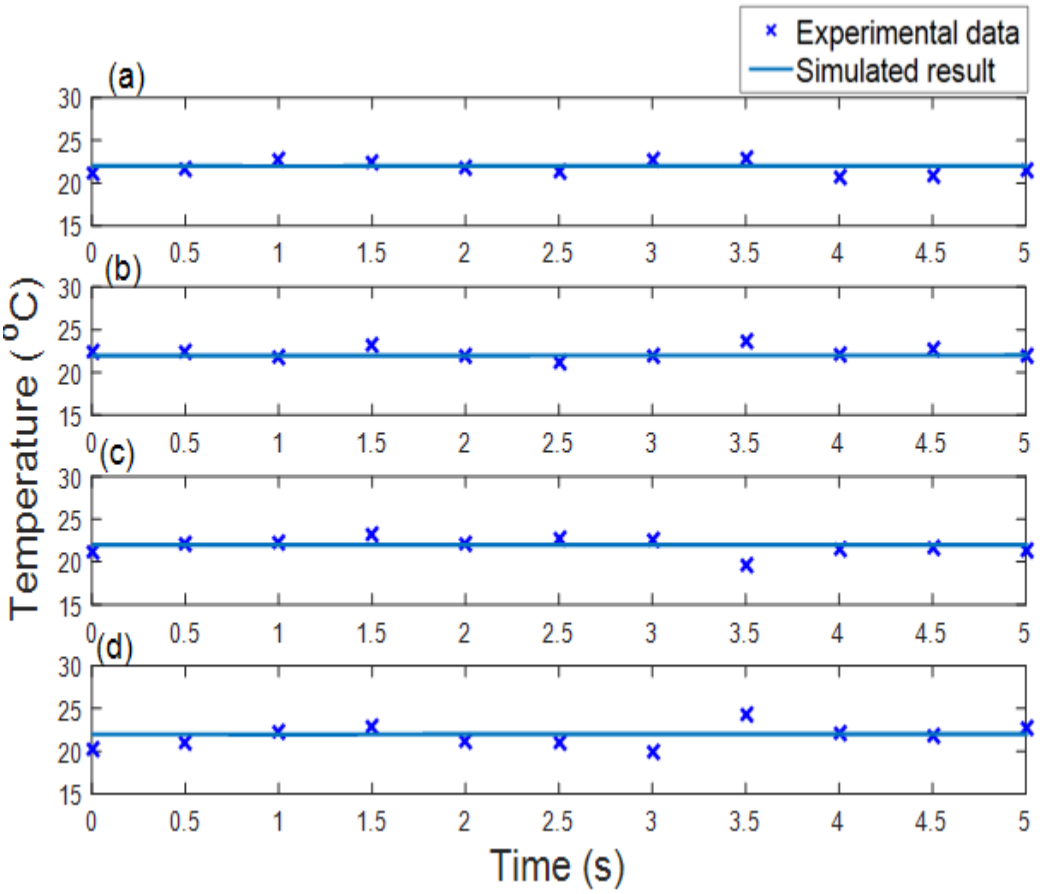

Figure 6-5: Simulated and experimental temporal thermal profiles at z = - 2 mm at sampling locations (a) A, (b) B, (c) C, and (d) D(see Figure 6-3)

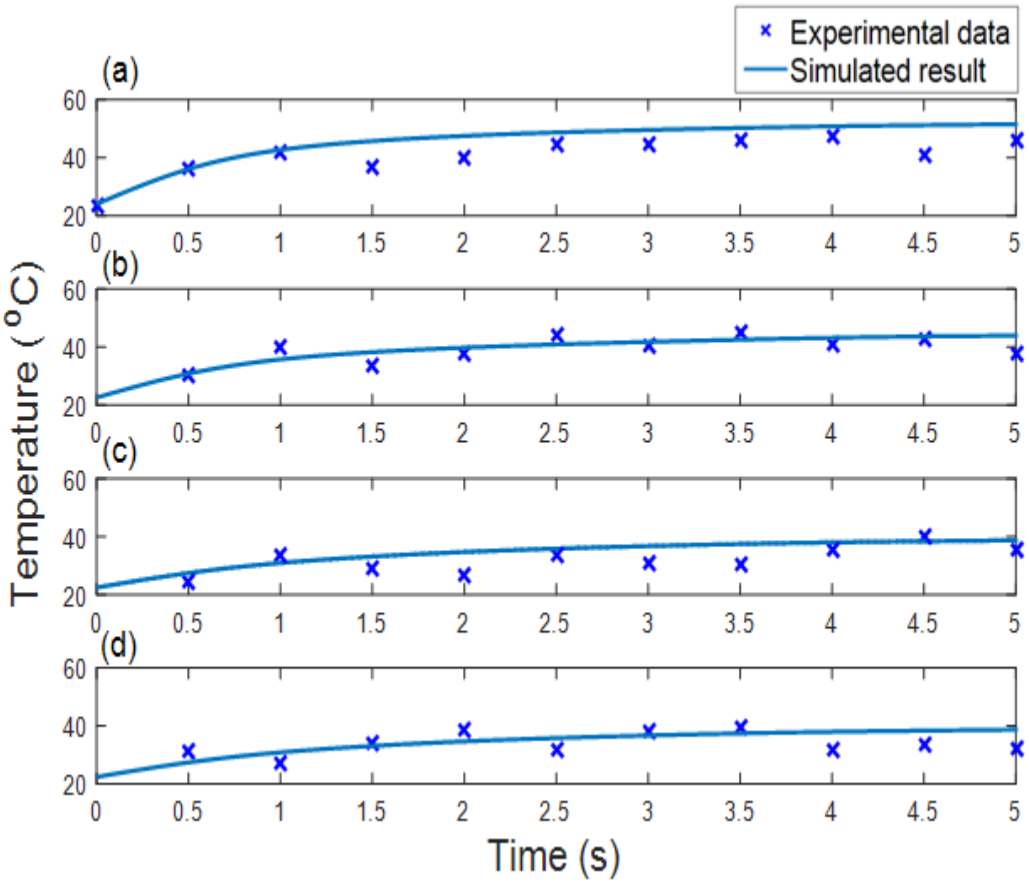

Figure 6-6: Simulated and experimental temporal thermal profiles at z = - 1 mm at sampling locations (a) A, (b) B, (c) C, and (d) D(see Figure 6-3)

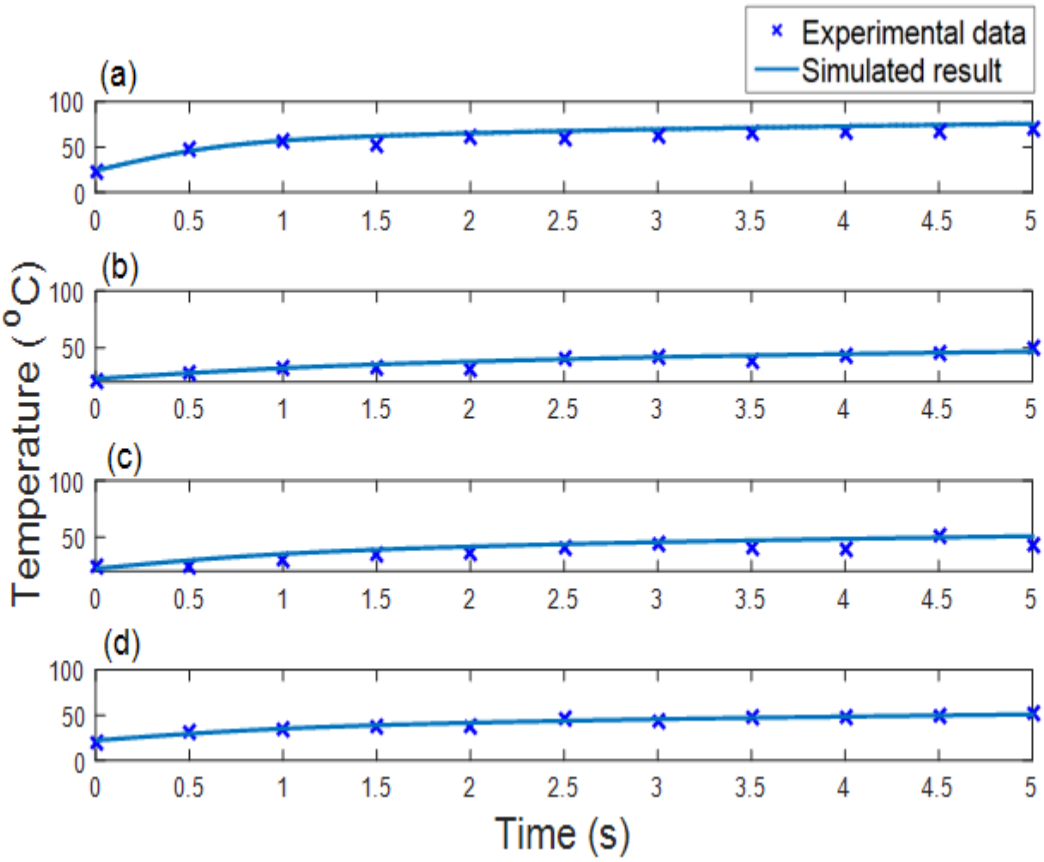

Figure 6-7: Simulated and experimental temporal thermal profiles at z = 0 mm at sampling locations (a) A, (b) B, (c) C, and (d) D (see Figure 6-3)

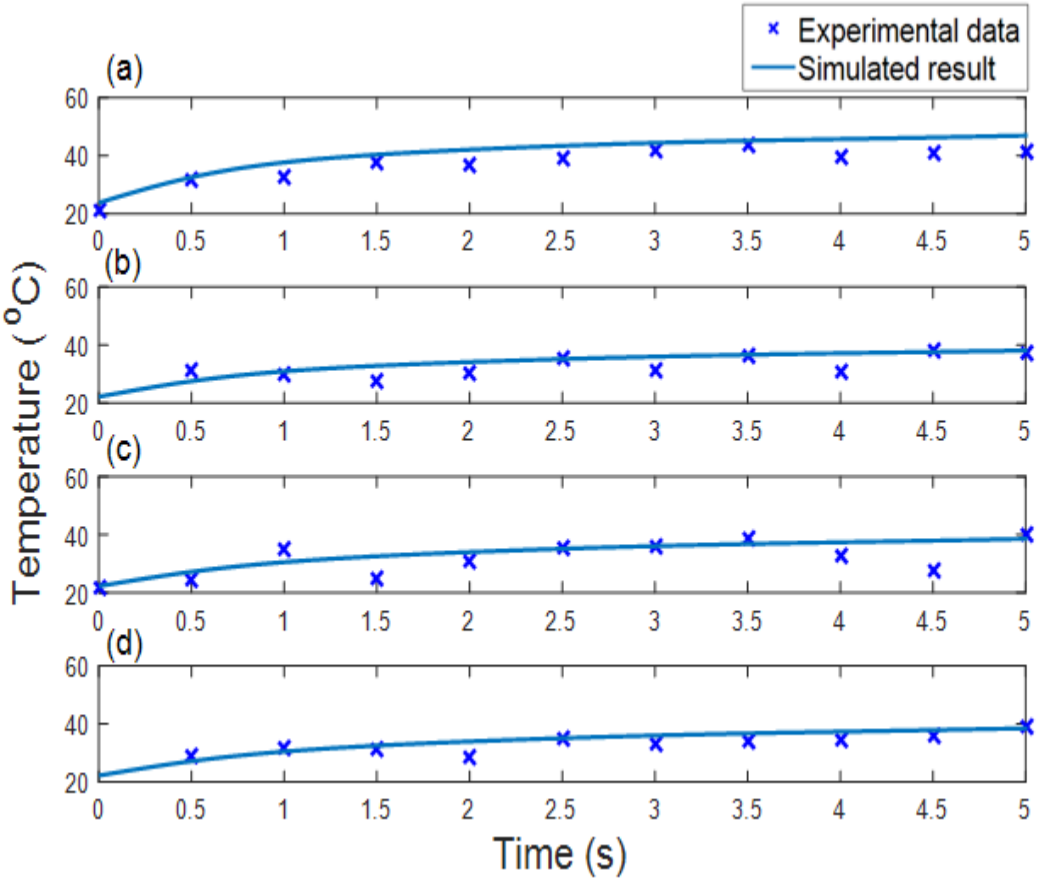

Figure 6-8: Simulated and experimental temporal thermal profiles at z = 1 mm at sampling locations (a) A, (b) B, (c) C, and (d) D(see Figure 6-3)

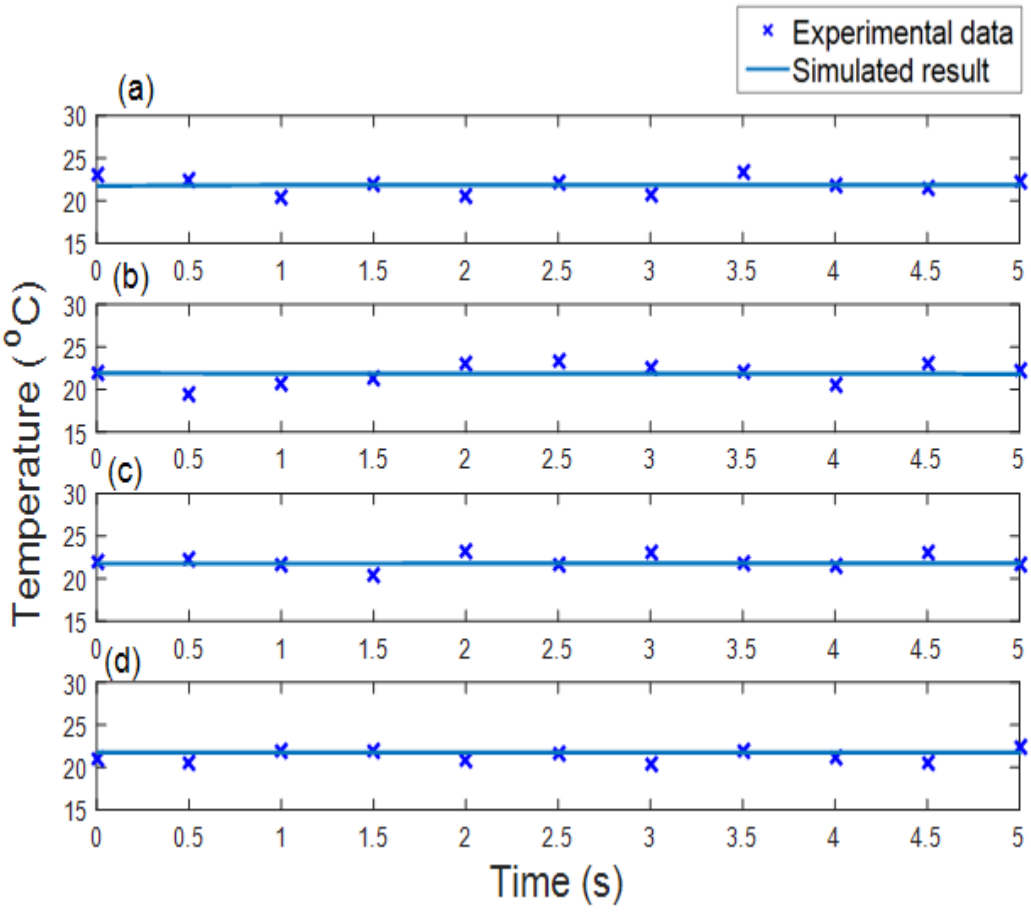

Figure 6-9: Simulated and experimental temporal thermal profiles at z = 2 mm at sampling locations (a) A, (b) B, (c) C, and (d) D(see Figure 6-3)

The simulated results are in excellent agreement with the experimental results. Similar to the experimental results, it was observed that with the employed values of the coefficients of absorption and the nonlinear absorption threshold intensity, the linear and the nonlinear regime can be distinguished. At z = 0 mm, the simulated result yielded the maximum rise in temperature in the sample as there was maximum

nonlinear absorption. At z = - 1 mm and z = 1 mm, nonlinear absorption remained and thus there were noticeable temperature increase. Consistent with experimental observations, at z = - 2 mm and z = 2 mm, there were negligible temperature rise in the sample as there was only linear absorption.

From the excellent agreement between the predicted and experimentally observed temperature profiles presented in Figure 6-5 through Figure 6-9, it can be reaffirmed that the coefficient of linear absorption, the coefficient of nonlinear absorption and the nonlinear absorption threshold intensity calculated in section 4.4 (above) in Chapter 4 are excellent approximations of the actual values.

6.3.4 Summary

The temperature distribution on the sample surface during laser irradiation by a femtosecond laser (Quantronix Integra-C 1.0 amplifier system) on Gorilla Glass 2320 was studied at different z-locations. Subsequently, a mathematical model for heat transfer to account for the laser energy absorbed during laser irradiation was developed. The developed model was solved using COMSOL Multiphysics, a finite element software.

During laser irradiation, the laser energy is absorbed by the material as heat. The absorbed heat is then transferred to the material increasing its temperature. This process of heat transfer during laser irradiation was directly observed using a thermal camera, FLIR MWIR SC5000. From the temperature distributions obtained, it was observed that at and around the focal plane of the laser beam, the temperature rise of the sample was high; however, as the sample is moved away from the focal plane no

significant temperature rise was observed. This can be attributed to high laser intensity around the focal plane which leads to nonlinear absorption. In contrast, away from the focal plane, there is low laser intensity which cannot initiate nonlinear absorption, but only linear absorption. From the observed temperature profiles, regions of linear and nonlinear absorption can be deduced. This provides the justification of having a nonlinear absorption threshold intensity for the describing of the overall absorption coefficient.

The observed spatial distribution of temperature along the sample surface indicated that the majority of the total laser energy is absorbed near the entry surface of the sample. The absorption occurs along the thickness in the laser propagation direction. Due to nonlinear absorption, the laser power intensity decays quickly. This rapid decay results in a change in the mode of absorption from nonlinear to linear, resulting in little energy absorbed. This reaffirms the findings obtained in Chapter 4, section 4.4.2 (above), in that the laser intensity within the material decays quickly, within 220 μm into the material.

A mathematical model was developed for modelling the thermal heat transfer into the material during laser irradiation. The laser heating source was first calculated as power absorbed by the materials as dictated by the values of the coefficients of absorption and the nonlinear absorption threshold intensity obtained in Chapter 4 section 4.4. The excellent agreements between the simulated and the experimental results indicate that the values of the coefficients of absorption and the nonlinear

absorption threshold intensity previously determined are good approximation of the true values.

Chapter 7: Conclusions and future work

7.1 Conclusions

Ever since the development of Q-switching and mode-locking techniques, the ultrashort pulsed laser has been used in material processing and research. The ultrashort pulsed laser-material interaction is a complicated process, and an in-depth study is required. Over the years, studies have been conducted to understand ultrashort pulsed laser-material interaction; however, there are still outstanding issues to be addressed. These include:

(a) effects of the linear and non-linear coefficients of absorption and the proposed nonlinear absorption threshold intensity for the quantification of laser power absorption during ultrashort pulsed laser irradiation, in particular for a transparent or semi-transparent material;

(b) the necessity or appropriateness of employing the concept of "thick" or "thin" material classification based on Rayleigh length, especially during Z-scan analysis, and the associated beam intensity distribution within the transparent material during ultrashort pulsed laser irradiation;

(c) the effects of laser-induced plasma during ultrashort pulsed laser irradiation;

(d) the thermal effect induced by the ultrashort pulsed laser on a transparent or semi-transparent material and the subsequent heat conduction after laser power absorption in the material.

To address these outstanding issues, a femtosecond laser (Quantronix Integra C-1.0 laser amplifier system) with a pulse width duration of 130 fs (FWHM), central laser wavelength of 795 nm, and repetition rate of 1 kHz, has been employed as the ultrashort pulsed laser for the investigation. Gorilla Glass 2320 of thickness 500 μm has been chosen as the sample as it is not totally transparent at the central laser wavelength of Quantronix Integra C-1.0. This allows the investigation to focus on nonlinear absorption, but with contribution from linear absorption.

The outcomes of the investigation may be summarized as:

(a) Proper representation of the coefficients of linear and nonlinear absorption and the proposed nonlinear absorption threshold intensity for the quantification of laser power absorption during femtosecond laser irradiation in a transparent material at a given laser wavelength.

Hitherto, the overall coefficient of absorption has been conventionally expressed as:

$$\alpha(I) = \alpha + \beta I \tag{1-1}$$

As discussed, equation (1-1) has deficiencies in that (a) nonlinear absorption always exists, even in the linear absorption region, and (b) there is no consistency between the units of the absorption coefficients, with different units between the linear coefficient of absorption α and the nonlinear coefficient of absorption β.

To address these deficiencies, in this study, the overall coefficient of absorption has been expressed as:

$$\alpha = \begin{cases} \alpha_o & \forall\, I(z,r,t) < I_{th} \\ \alpha_o + \alpha_1 \cdot \dfrac{I(z,r,t)}{I_{th}} & \forall\, I(z,r,t) \geq I_{th} \end{cases} \quad (4\text{-}4)$$

In contrast to the previous studies, the nonlinear absorption threshold intensity I_{th} has been introduced in the overall absorption coefficient description. This is an important departure with the existing approach as with the introduction of I_{th}, it allows the delineation and identification of the region of linear absorption from the region of nonlinear absorption.

In addition, through the introduction of I_{th}, the inconsistency in unit is resolved in that both the linear coefficient of absorption α_o and nonlinear coefficient of absorption α_1 have the same unit.

Indeed, this investigation reveals that without the introduction of nonlinear absorption threshold intensity I_{th}, the conventional approach will not result in any meaningful linear and nonlinear coefficients of absorption which can describe well the experimental observations. This is because without I_{th}, the equation in the existing literature, namely equation (1-1), indicates that there will always be nonlinear absorption at any laser power intensity; this is not exactly valid at low laser power intensity.

This new formulation for absorption coefficients forms the foundation for this investigation to quantify simultaneously the coefficient of linear

absorption, the coefficient of nonlinear absorption, and the nonlinear absorption threshold intensity of a materiel, in particular Gorilla Glass 2320. Without the new formulation, it will be impossible to investigate the interplay between linear and nonlinear absorption, in particular the nonlinear absorption threshold intensity.

For the experimental investigation, the Z-scan technique was employed for the study of laser power absorption during laser irradiation. The investigation was carried out at three laser power levels of 21.80 mW, 58.21 mW, and 99.64 mW. The linear and nonlinear absorption coefficients were determined respectively to be 2.01 $cm^{-1} \pm 0.08\ cm^{-1}$ (uncertainty less than 5%) and 0.0013 $cm^{-1} \pm 0.0002\ cm^{-1}$ (uncertainty less than 15%), and the coefficient of nonlinear absorption threshold intensity to be $42.1 \times 10^{12}\ W/cm^2 \pm 1.89 \times 10^{12}\ W/cm^2$ (uncertainty less than 5%).

With the computed values of the coefficient of linear absorption, the coefficient of nonlinear absorption, and the nonlinear absorption threshold intensity, excellent agreement was obtained between the calculated absorption and the experimentally observed absorption.

(b) *The necessity or appropriateness of employing the concept of "thick" or "thin" material classification based on Rayleigh length, especially during Z-scan analysis, and the associated beam intensity distribution within the transparent material.*

In Chapter 4, section 4.4.2, Rayleigh length is given as [14, 15]

$$z_R = \frac{\pi \omega_o^2}{\lambda} \tag{4-25}$$

In the literature, any sample with thickness less or greater than the Rayleigh length is classified as a thin or thick sample respectively. Different analyses of laser power absorption are applicable depending if the sample is "thin" or "thick". In a thin sample, it is believed that the material undergoes nonlinear absorption throughout the thickness when the sample is very close to the focal plane of the laser beam, with the implicit assumption that the laser beam profile remains constant as it traverses the sample.

However, the justification of using the Rayleigh length to classify the sample "thickness" with the associated different analyses has not been spelt out. Indeed, Rayleigh length is related to the laser beam profile, and its application to sample "thickness" is not obvious or appropriate.

For the current investigation, the Rayleigh length of the laser beam is 889 μm; the 500 μm thick Gorilla Glass sample will be considered as a "thin" sample. At z = 0 mm with an average laser power of 21.6 mW, laser power intensity decay along the axial line of beam propagation within the glass sample was studied. There was nonlinear and rapid decay of the laser intensity as the laser beam propagated through the medium. At a depth of 220 μm from the entry surface, the intensity had already decreased significantly and was below the nonlinear absorption threshold intensity. Thus, when the

laser beam travelled further into the medium, there would be linear absorption and without any significant nonlinear absorption. This indicates that even for a so called "thin" sample, the mode of absorption at a different thickness location can be different. This study also indicates that the laser beam profile will not remain constant. It evolves as it travels through the thickness of the "thin" sample due to nonlinear absorption. Thus, it can be concluded that the classification of the "thickness" of the material based on Rayleigh length is not appropriate. Rather, to gain a good insight, it is necessary to take into consideration the unique characteristics of nonlinear absorption for all sample thickness.

Avoiding the pitfall of having the Rayleigh length to classify the sample thickness and the associated analytical methods, this investigation formulates and develops a universal analytical framework with the associated numerical procedures which is applicable to any sample thickness.

(c) Plasma formation and plasma shielding during femtosecond laser irradiation

During short-pulsed laser irradiation of a material, laser-induced plasma is formed. As a femtosecond laser has very high-power intensity, the efficiency of inducing a plasma is high. Hitherto there is no direct observation of the laser-induced plasma in glass, and the effect of the laser-induced plasma during femtosecond laser irradiation has yet to be studied.

In this investigation, direct observation of the laser-induced plasma on Gorilla Glass 2320 has been studied using a high-speed camera Photron SA5, with a cut-on filter or a cut-off filter. Well-defined plasma images could be observed with a FESH0750 filter (a cut-off filter with a cut-off wavelength of 750 nm), and no plasma images could be observed with a FELH0850 filter (a cut-on filter with a cut-on wavelength of 850 nm). This indicates that the plasma photon energy generated during laser irradiation was below 750 nm but not above 850 nm. This is an expected result, as plasma is of high energy, and lower wavelength means higher energy.

To explore if the plasma formation has any effect on the laser power absorption behavior, an attempt was made to study the laser-induced plasma decay time. However, despite of employing a rather high imaging frame rate of 930,000 fps, the laser-induced plasma could not be observed in any two consecutive frames. As such, with the experimental set-up in this investigation, it is not possible to deduce the plasma decay time. Instead, it can be concluded that the plasma generated has a rapid decay, and that the plasma generated by one pulse will not interact with the next incoming pulse at a pulse repetition rate of 1kHz. Thus, there will not be any plasma shielding on the next incoming pulse.

The laser-induced plasma was observed for different sample z-locations in the Z-scan experimental setup at low and high average laser powers. For high laser power, plasma could only be observed when the sample was placed at or near the laser focal plane, but not when it was away from the focal plane

even when there was nonlinear absorption. For low laser power, plasma could not be observed even when the sample was at the focal plane. This indicates that the laser power intensity must be sufficiently high to ablate the material for plasma formation to occur, and that nonlinear absorption alone is not a sufficient condition to ensure plasma formation.

(d) Thermal effect induced by the femtosecond laser and subsequent heat conduction after laser power absorption in the transparent material.

The laser power absorbed by the material during laser irradiation is subsequently dissipated into the bulk of the material as heat, raising its temperature. A thermal camera was employed for the direct observation of the temperature field during laser irradiation. Thermal images were taken during laser irradiation at an average laser power of 20.06 mW at different z-locations.

Simultaneously, the absorbed laser power was computed using the determined coefficients of absorption. This computed absorbed laser power was used as the heat source for the prediction of the temperature profile of the samples for the corresponding experimental conditions. Excellent agreements were obtained between the predicted and experimentally observed temperature profiles. This provides an independent assessment of the good approximation of the previously determined linear and nonlinear coefficients of absorption, and the nonlinear absorption threshold intensity.

7.2 Future work

For further studies and investigations, the following are recommended:

1. Nonlinear absorption properties of Gorilla Glass 2320 have been studied in this investigation. As a new formulation for the nonlinear absorption coefficient has been proposed, similar investigations of nonlinear absorption on other transparent, semi-transparent, and non-transparent materials could be carried out to verify the general applicability of this proposed methodology.
2. In this investigation, the power level was chosen in such a way to avoid ablation and plasma shielding such as not to introduce complications in the determination and verification of the absorption coefficients. Investigations at higher laser power with ablation and plasma formation should be conducted to further verify the accuracy of the determined absorption coefficients.
3. The model developed can account for varying laser beam diameter of a focused beam. As the thickness of the sample used was 500 μm, it was assumed that the change in beam diameter due to self-focusing or self-defocusing is negligible. It will be of interest to investigate the effect of changes in beam diameter as a result of a material's nonlinear refractive index.

4. As Gorilla Glass 2320 is a chemically strengthened glass, it has compressive stress at the surface and tensile stress in its interior. The interaction between the thermal stress generated during laser irradiation and the residual compressive/tensile stress may be studied.

References

1. Liu, X., D. Du, and G. Mourou, *Laser ablation and micromachining with ultrashort laser pulses.* Quantum Electronics, IEEE Journal of, 1997. **33**(10): p. 1706-1716.
2. Kawamura, Y., K. Toyoda, and S. Namba, *Effective deep ultraviolet photoetching of polymethyl methacrylate by an excimer laser.* Applied Physics Letters, 1982. **40**(5): p. 374-375.
3. Terzaki, K. and M. Farsari, *Polymer Processing Through Multiphoton Absorption*, in *Polymer and Photonic Materials Towards Biomedical Breakthroughs*. 2018, Springer. p. 49-69.
4. Khaing, M., J. Fuh, and L. Lu, *Direct metal laser sintering for rapid tooling: processing and characterisation of EOS parts.* Journal of Materials Processing Technology, 2001. **113**(1): p. 269-272.
5. Santos, E.C., et al., *Rapid manufacturing of metal components by laser forming.* International Journal of Machine Tools and Manufacture, 2006. **46**(12): p. 1459-1468.
6. Kumar, K.K., G. Samuel, and M. Shunmugam, *Theoretical and experimental investigations of ultra-short pulse laser interaction on Ti6Al4V alloy.* Journal of Materials Processing Technology, 2019. **263**: p. 266-275.
7. Nikumb, S., et al., *Precision glass machining, drilling and profile cutting by short pulse lasers.* Thin Solid Films, 2005. **477**(1): p. 216-221.
8. Sugioka, K. and Y. Cheng, *Ultrafast lasers—reliable tools for advanced materials processing.* Light: Science & Applications, 2014. **3**(4): p. e149.
9. Fleischer, A. and N. Moiseyev, *Attosecond laser pulse synthesis using bichromatic high-order harmonic generation.* Physical Review A, 2006. **74**(5): p. 053806.
10. Kozlowski, M. and J. Marciak-Kozlowska, *Thermal processes using attosecond laser pulses: When Time Matters*. Vol. 121. 2006: Springer.
11. Osellame, R., G. Cerullo, and R. Ramponi, *Femtosecond Laser Micromachining: Photonic and Microfluidic Devices in Transparent Materials*. Vol. 123. 2012: Springer Science & Business Media.
12. Sundaram, S. and E. Mazur, *Inducing and probing non-thermal transitions in semiconductors using femtosecond laser pulses.* Nature materials, 2002. **1**(4): p. 217.
13. Von der Linde, D. and H. Schüler, *Breakdown threshold and plasma formation in femtosecond laser–solid interaction.* JOSA B, 1996. **13**(1): p. 216-222.

14. Sheik-Bahae, M., A.A. Said, and E.W. Van Stryland, *High-sensitivity, single-beam n 2 measurements.* Optics letters, 1989. **14**(17): p. 955-957.

15. Sheik-Bahae, M., et al., *Sensitive measurement of optical nonlinearities using a single beam.* IEEE journal of quantum electronics, 1990. **26**(4): p. 760-769.

16. de Araújo, C.B., A.S. Gomes, and G. Boudebs, *Techniques for nonlinear optical characterization of materials: a review.* Reports on Progress in Physics, 2016. **79**(3): p. 036401.

17. Kozich, V., F. Hernandez, and J. Castillo, *Dual-beam time-resolved Z-scan in liquids to study heating due to linear and nonlinear light absorption.* Applied spectroscopy, 1994. **48**(12): p. 1506-1512.

18. Zhao, W. and P. Palffy‐Muhoray, *Z‐scan technique using top‐hat beams.* Applied physics letters, 1993. **63**(12): p. 1613-1615.

19. Qi, P., et al., *Optical nonlinearities of alcoholic liquids under high-repetition-rate femtosecond lasers by single beam time-resolved eclipsed Z-scan.* Optics & Laser Technology, 2019. **109**: p. 643-647.

20. Nóvoa-López, J.A., et al., *Nonlinear absorption in ionic liquids with transition metallic atoms in the anion.* Optical Materials, 2016. **52**: p. 144-149.

21. Noskovicova, E., et al., *Femtosecond Kerr index of cyclic olefin co/polymers for THz nonlinear optics.* Optical Materials, 2016. **60**: p. 559-563.

22. Heberle, J., T. Häfner, and M. Schmidt, *Nonlinear absorption measurements of intraocular lens polymers by integrating Z-scan.* Journal of Laser Applications, 2016. **28**(2): p. 022604.

23. Jin, Z., et al., *Nonlinear optical properties of some polymer/multi-walled carbon nanotube composites.* Chemical Physics Letters, 2000. **318**(6): p. 505-510.

24. Cassano, T., et al., *Substituent-dependence of the optical nonlinearities in poly (2, 5-dialkoxy-p-phenylenevinylene) polymers investigated by the Z-scan technique.* Chemical Physics, 2001. **272**(1): p. 111-118.

25. Lam, S., M. Chan, and D. Lo, *Z-scan measurements of the nonlinear absorption and refractive index for fluorescein 548-doped organically modified sol–gel silica films.* Optical materials, 2001. **18**(2): p. 235-241.

26. Zheng, X., et al., *Enhanced nonlinear optical properties of nonzero-bandgap graphene materials in glass matrices.* Journal of Materials Chemistry C, 2014. **2**(21): p. 4121-4125.

27. Smektala, F., et al., *Non-linear optical properties of chalcogenide glasses measured by Z-scan.* Journal of non-crystalline solids, 2000. **274**(1-3): p. 232-237.

28. Hashimoto, T., et al., *Optical non-linearity of TiO2-containing glasses measured by Z-scan technique.* Journal of non-crystalline solids, 1999. **253**(1-3): p. 30-36.

29. Wang, T., et al., *Systematic z-scan measurements of the third order nonlinearity of chalcogenide glasses.* Optical Materials Express, 2014. **4**(5): p. 1011-1022.

30. Hasegawa, T., T. Nagashima, and N. Sugimoto, *Z-scan study of third-order optical nonlinearities in bismuth-based glasses.* Optics communications, 2005. **250**(4-6): p. 411-415.

31. Dehghani, Z., et al., *Synthesis and investigation of nonlinear optical properties of semiconductor ZnS nanoparticles.* Journal of Physics and Chemistry of Solids, 2011. **72**(9): p. 1008-1010.

32. Ganeev, R. and A. Ryasnyansky, *Reflection z‐scan measurements of opaque semiconductor thin films.* physica status solidi (a), 2005. **202**(1): p. 120-125.

33. Quarterman, A., M. Tyrk, and K. Wilcox, *Z-scan measurements of the nonlinear refractive index of a pumped semiconductor disk laser gain medium.* Applied Physics Letters, 2015. **106**(1): p. 011105.

34. Tamgadge, Y., G. Muley, and R. Ganorkar, *Z-scan studies of Sn doped CuO nano-colloidal suspension.* Optical Materials, 2019. **89**: p. 591-597.

35. Ali, Q.M. and P. Palanisamy, *Z-scan determination of the third-order optical nonlinearity of organic dye nile blue chloride.* Modern Physics Letters B, 2006. **20**(11): p. 623-632.

36. Sinha, S., A. Ray, and K. Dasgupta, *Solvent dependent nonlinear refraction in organic dye solution.* Journal of Applied Physics, 2000. **87**(7): p. 3222-3226.

37. Kumar, R.S.S., et al., *Femtosecond and nanosecond nonlinear optical properties of alkyl phthalocyanines studied using Z-scan technique.* Chemical physics letters, 2007. **447**(4-6): p. 274-278.

38. Gu, B., et al., *Z-scan technique for characterizing third-order optical nonlinearity by use of quasi-one-dimensional slit beams.* JOSA B, 2004. **21**(5): p. 968-972.

39. Chapple, P., J. Staromlynska, and R. McDuff, *Z-scan studies in the thin-and the thick-sample limits.* JOSA B, 1994. **11**(6): p. 975-982.

40. Xia, T., et al., *Z-scan and EZ-scan measurements of optical nonlinearities.* International Journal of Nonlinear Optical Physics, 1994. **3**(04): p. 489-500.

41. Hughes, S. and J.M. Burzler, *Theory of Z-scan measurements using Gaussian-Bessel beams.* Physical Review A, 1997. **56**(2): p. R1103.

42. Chapple, P., et al., *Single-Beam Z-Scan:. Measurement Techniques and Analysis.* Journal of Nonlinear Optical Physics and Materials, 1997. **6**: p. 251-293.

43. Petrov, D., A. Gomes, and C.B. De Araújo, *Reflection Z‐scan technique for measurements of optical properties of surfaces.* Applied physics letters, 1994. **65**(9): p. 1067-1069.

44. Ma, H., A. Gomes, and C.B. de Araújo, *Measurements of nondegenerate optical nonlinearity using a two‐color single beam method.* Applied physics letters, 1991. **59**(21): p. 2666-2668.

45. Xia, T., et al., *Eclipsing Z-scan measurement of λ/10 4 wave-front distortion.* Optics letters, 1994. **19**(5): p. 317-319.

46. Zang, W.-P., et al., *Analytic solutions to Z-scan characteristics of thick media with nonlinear refraction and nonlinear absorption.* JOSA B, 2004. **21**(1): p. 63-66.

47. Zheng, X., et al., *Characterization of nonlinear properties of black phosphorus nanoplatelets with femtosecond pulsed Z-scan measurements.* Optics letters, 2015. **40**(15): p. 3480-3483.

48. Zheng, X., et al., *Z-scan measurement of the nonlinear refractive index of monolayer WS 2.* Optics express, 2015. **23**(12): p. 15616-15623.

49. Gattass, R.R. and E. Mazur, *Femtosecond laser micromachining in transparent materials.* Nature photonics, 2008. **2**(4): p. 219.

50. Liu, X., D. Du, and G. Mourou, *Laser ablation and micromachining with ultrashort laser pulses.* IEEE journal of quantum electronics, 1997. **33**(10): p. 1706-1716.

51. Varel, H., et al., *Micromachining of quartz with ultrashort laser pulses.* Applied Physics A: Materials Science & Processing, 1997. **65**(4): p. 367-373.

52. Chien, C. and M. Gupta, *Pulse width effect in ultrafast laser processing of materials.* Applied Physics A, 2005. **81**(6): p. 1257-1263.

53. Arai, A.Y., et al., *Transparent material processing with an ultrashort pulse laser*. 2015, Google Patents.

54. Neev, J., et al., *Ultrashort pulse high repetition rate laser system for biological tissue processing*. 1998, Google Patents.

55. Bonse, J., et al., *Ultrashort-pulse laser ablation of indium phosphide in air.* Applied Physics A, 2001. **72**(1): p. 89-94.

56. Shishkovskii, I., I. Yadroitsev, and I.Y. Smurov, *Selective laser sintering/melting of nitinol–hydroxyapatite composite for medical applications.* Powder Metallurgy and Metal Ceramics, 2011. **50**(5-6): p. 275.

57. Li, R., et al., *Effects of processing parameters on the temperature field of selective laser melting metal powder.* Powder Metallurgy and Metal Ceramics, 2009. **48**(3-4): p. 186-195.

58. Balla, V.K., S. Bose, and A. Bandyopadhyay, *Processing of bulk alumina ceramics using laser engineered net shaping.* International Journal of Applied Ceramic Technology, 2008. **5**(3): p. 234-242.

59. Samant, A.N. and N.B. Dahotre, *Laser machining of structural ceramics—A review.* Journal of the European ceramic society, 2009. **29**(6): p. 969-993.

60. Jervis, T.R., et al., *Excimer laser surface processing of ceramics: process and properties.* Journal of the American Ceramic Society, 1993. **76**(2): p. 350-355.

61. Baudach, S., et al., *Ultrashort pulse laser ablation of polycarbonate and polymethylmethacrylate.* Applied surface science, 2000. **154**: p. 555-560.

62. Heberle, J., T. Haefner, and M. Schmidt, *Efficient and damage-free ultrashort pulsed laser cutting of polymer intraocular lens implants.* CIRP Annals, 2018. **67**(1): p. 197-200.

63. Wang, B., et al., *Thermal effect of femtosecond laser polystyrene processing.* Optics & Laser Technology, 2019. **117**: p. 244-250.

64. Watanabe, W., Y. Li, and K. Itoh, *Ultrafast laser micro-processing of transparent material.* Optics & Laser Technology, 2016. **78**: p. 52-61.

65. Bulgakova, N.M., et al., *How to optimize ultrashort pulse laser interaction with glass surfaces in cutting regimes?* Applied Surface Science, 2015. **336**: p. 364-374.

66. Mishchik, K., et al., *Ultrashort pulse laser cutting of glass by controlled fracture propagation.* 2016.

67. Le Harzic, R., et al., *Comparison of heat-affected zones due to nanosecond and femtosecond laser pulses using transmission electronic microscopy.* Applied Physics Letters, 2002. **80**(21): p. 3886-3888.

68. Kaden, L., et al., *Selective laser melting of copper using ultrashort laser pulses.* Applied Physics A, 2017. **123**(9): p. 596.

69. Bonse, J., et al., *Femtosecond laser texturing of surfaces for tribological applications.* Materials, 2018. **11**(5): p. 801.

70. Krüger, J. and W. Kautek, *Ultrashort pulse laser interaction with dielectrics and polymers*, in *polymers and light*. 2004, Springer. p. 247-290.

71. Jagannath, G., et al., *Linear and nonlinear optical properties of gold nanoparticles doped borate glasses.* Journal of Non-Crystalline Solids, 2018. **482**: p. 160-169.

72. Tian, J.-G., et al., *Analysis of beam propagation in thick nonlinear media.* Applied optics, 1995. **34**(21): p. 4331-4336.

73. Hermann, J. and R. McDuff, *Analysis of spatial scanning with thick optically nonlinear media.* JOSA B, 1993. **10**(11): p. 2056-2064.

74. Wang, B., et al., *Femtosecond Laser-Induced Nonlinear Absorption in Thick Polystyrene.* Lasers in Manufacturing and Materials Processing, 2019: p. 1-8.

75. Fedosejevs, R., et al., *Absorption of femtosecond laser pulses in high-density plasma.* Physical review letters, 1990. **64**(11): p. 1250.

76. Zhang, Z., et al., *Multi-diagnostic comparison of femtosecond and nanosecond pulsed laser plasmas.* Journal of applied physics, 2002. **92**(5): p. 2867-2874.

77. Lam, Y., D. Tran, and H. Zheng, *A study of substrate temperature distribution during ultrashort laser ablation of bulk copper.* Laser and Particle Beams, 2007. **25**(1): p. 155-159.

78. Tran, D., et al., *Quantification of thermal energy deposited in silicon by multiple femtosecond laser pulses.* Optics express, 2006. **14**(20): p. 9261-9268.

79. Tran, D., et al., *Direct observation of the temperature field during ablation of materials by multiple femtosecond laser pulses.* Applied surface science, 2007. **253**(17): p. 7290-7294.

80. Sugioka, K., M. Meunier, and A. Piqué, *Laser precision microfabrication*. 2010: Springer.

81. Smith, W.L., *Laser-induced breakdown in optical materials.* Optical Engineering, 1978. **17**(5): p. 175489-175489-.

82. Boyd, R.W., *Nonlinear optics*. 2003: Academic press.

83. Li, C., *Polarization Theory of Nonlinear Medium*, in *Nonlinear Optics*. 2017, Springer. p. 23-50.

84. Butcher, P.N. and D. Cotter, *The elements of nonlinear optics*. Vol. 9. 1991: Cambridge university press.

85. Fisher, R.A., *Optical phase conjugation*. 2012: Academic Press.

86. Acioli, L., et al., *Ultrafast chi/sup (3)/-related processes in semiconductor doped glasses.* IEEE Journal of Quantum Electronics, 1990. **26**(7): p. 1277-1284.

87. Dolgaleva, K., H. Shin, and R.W. Boyd, *Observation of a microscopic cascaded contribution to the fifth-order nonlinear susceptibility.* Physical review letters, 2009. **103**(11): p. 113902.

88. Zhong, Q. and J.T. Fourkas, *Optical Kerr effect spectroscopy of simple liquids.* The Journal of Physical Chemistry B, 2008. **112**(49): p. 15529-15539.

89. Ho, P. and R. Alfano, *Optical Kerr effect in liquids.* Physical Review A, 1979. **20**(5): p. 2170.

90. Righini, R., *Ultrafast optical Kerr effect in liquids and solids.* Science, 1993. **262**(5138): p. 1386-1390.

91. Stolen, R. and A. Ashkin, *Optical Kerr effect in glass waveguide.* Applied Physics Letters, 1973. **22**(6): p. 294-296.

92. Sheik-Bahae, M., J. Wang, and E. Van Stryland, *Nondegenerate optical Kerr effect in semiconductors.* IEEE journal of quantum electronics, 1994. **30**(2): p. 249-255.

93. Arzhantsev, S. and M. Maroncelli, *Design and characterization of a femtosecond fluorescence spectrometer based on optical Kerr gating.* Applied spectroscopy, 2005. **59**(2): p. 206-220.

94. Prasad, P.N. and D.J. Williams, *Introduction to nonlinear optical effects in molecules and polymers*. Vol. 1. 1991: Wiley New York etc.

95. Levenson, M., *Introduction to Nonlinear Laser Spectroscopy 2e*. 2012: Elsevier.

96. Chemla, D., *Non-linear optical properties of condensed matter.* Reports on Progress in Physics, 1980. **43**(10): p. 1191.

97. Jain, R. and M. Klein, *Degenerate four‐wave mixing near the band gap of semiconductors.* Applied Physics Letters, 1979. **35**(6): p. 454-456.

98. Lehr, L. and P. Hering, *Quantitative nonlinear spectroscopy: a direct comparison of degenerate four-wave mixing with cavity ring-down spectroscopy applied to NaH.* IEEE journal of quantum electronics, 1997. **33**(9): p. 1465-1473.

99. Nolte, S., et al., *Ablation of metals by ultrashort laser pulses.* JOSA B, 1997. **14**(10): p. 2716-2722.

100. Cheng, J., et al., *A review of ultrafast laser materials micromachining.* Optics & Laser Technology, 2013. **46**: p. 88-102.

101. Cheng, J., et al., *Single-pulse drilling study on Au, Al and Ti alloy by using a picosecond laser.* Applied Physics A, 2009. **95**(3): p. 739-746.

102. Ostendorf, A., et al. *Ablation of metals and semiconductors with ultrashort pulsed lasers: improving surface qualities of microcuts and grooves*. in *Commercial and biomedical applications of ultrafast lasers IV*. 2004. International Society for Optics and Photonics.

103. Simon, P. and J. Ihlemann, *Machining of submicron structures on metals and semiconductors by ultrashort UV-laser pulses.* Applied Physics A, 1996. **63**(5): p. 505-508.

104. Krueger, J., et al. *Structuring of dielectric and metallic materials with ultrashort laser pulses between 20 fs and 3 ps*. in *Laser Applications in Microelectronic and Optoelectronic Manufacturing II*. 1997. International Society for Optics and Photonics.

105. Murnane, M.M., et al., *Ultrafast x-ray pulses from laser-produced plasmas.* Science, 1991. **251**(4993): p. 531-536.

106. Canulescu, S., et al., *Mechanisms of the laser plume expansion during the ablation of LiMn 2 O 4.* Journal of Applied Physics, 2009. **105**(6): p. 063107.

107. Chen, Z. and S.S. Mao, *Femtosecond laser-induced electronic plasma at metal surface.* Applied Physics Letters, 2008. **93**(5): p. 051506.

108. Colombo, V., et al., *High-speed imaging in plasma arc cutting: a review and new developments.* Plasma sources science and technology, 2009. **18**(2): p. 023001.

109. Sick, V., *High speed imaging in fundamental and applied combustion research.* Proceedings of the Combustion Institute, 2013. **34**(2): p. 3509-3530.

110. Vollmer, M. and K.-P. Möllmann, *Infrared thermal imaging: fundamentals, research and applications*. 2010: John Wiley & Sons.

111. Bergman, T.L., F.P. Incropera, and A.S. Lavine, *Fundamentals of heat and mass transfer*. 2011: John Wiley & Sons.

112. Yang, C., W. Wang, and X. Mei. *Study on the thermal effects of femtosecond laser ablation on Ti-6A1–4V*. in *2012 IEEE International Conference on Mechatronics and Automation*. 2012. IEEE.

113. Le Harzic, R., et al. *TEM investigations of thermal effects on material structure induced by femtosecond and nanosecond laser processing*. in *Photon Processing in Microelectronics and Photonics*. 2002. International Society for Optics and Photonics.

114. Simpson, M., et al., *Application specific spectral response with CMOS compatible photodiodes.* IEEE Transactions on Electron Devices, 1999. **46**: p. 905-913.

115. Vadillo, J.M. and J.J. Laserna, *Laser-induced plasma spectrometry: truly a surface analytical tool.* Spectrochimica Acta Part B: Atomic Spectroscopy, 2004. **59**(2): p. 147-161.

116. Planinsic, G., *Infrared thermal imaging: fundamentals, research and applications.* 2011, IOP Publishing.

Appendix I

Thermal camera calibration

During thermography, the camera receives radiance from the object under observation, atmospheric thermal radiation, reflected thermal radiation of the surrounding objects and camera's internal thermal radiation due to its own internal temperature, see Figure . The internal thermal radiation of a camera is normally compensated by the camera software itself [116].

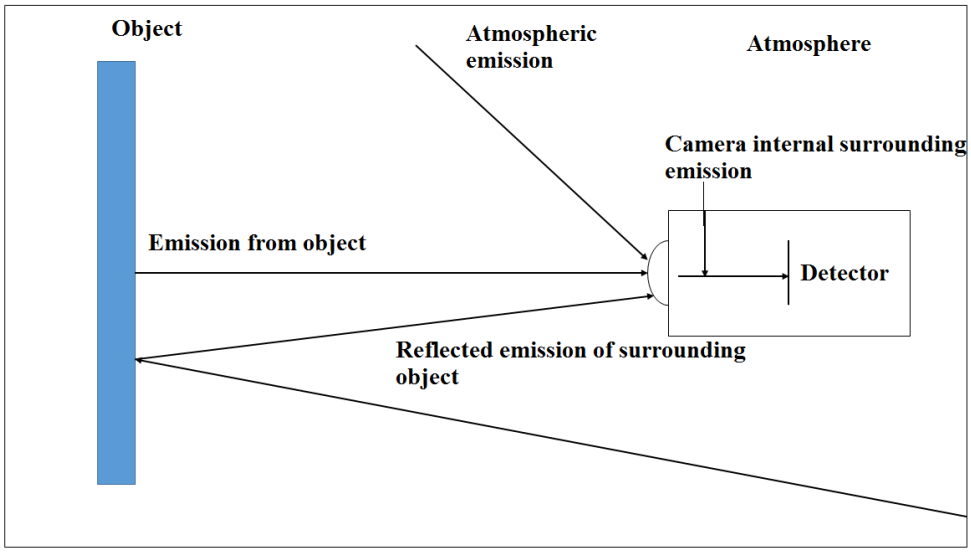

Figure A1-1: Various sources of infrared received by the infrared camera during thermography. It shows the attenuation of the infrared signal from an object due to optical path's absorption, reflected emission of surrounding objects, internal camera surrounding, and atmospheric emission.

The most significant noise is from the surrounding objects, for example, gas and moisture in the atmosphere. For any incident radiation, there will be reflection,

diffusion, scattering, and absorption. Therefore, to compensate for the attenuation loss, the scattering or absorption in the surrounding should be examined.

In addition, to minimize the effect of reflected thermal radiation from the surrounding object, an experiment is best to be conducted in an enclosure (closed system). The walls of the enclosure are painted black to minimize any reflectance of the objects in the closed system.

With these considerations, the radiation received by a thermal camera can be summarized as:

$$R'_T = \varepsilon R_T + R_{bg} \quad \text{(A1-1)}$$

Where R'_T is radiation received by the camera, $\boldsymbol{\varepsilon}$ is the emissivity of the object under observation, R_T is the radiation of black body at the temperature of the object under observation, and R_{bg} is background radiation which includes all the parameters affecting the camera's radiance reading. With the camera operated in medium-wave infrared, the attenuation from the surrounding is negligible and the atmospheric attenuation can be neglected [110]. The reflected radiance from the surrounding can also be neglected as the closed system is painted black. The radiance from the internal temperature of the camera is autocorrected by the thermal camera software. Thus, the term R_{bg} in equation A1-1 can be neglected.

To further minimize the error, the surface of the object under observation was painted black with PNM400 black paint from RS to approximate a black body, which has an emissivity close to unity, i.e. $\boldsymbol{\varepsilon} \sim 1$. Hence, equation (A1-1) can be written as

$$R'_T \approx R_T \quad \text{(A1-2)}$$

Calibration of thermal camera

For accurate temperature readings, the thermal camera must be properly calibrated. The temperature calibration was performed with thermocouples.

Materials and devices employed

For the calibration experiment, an infrared thermal camera, thermocouples, a thermometer, thermal epoxy glue, chemically strengthened glass, and black paint have been used.

Chemically strengthened glass

Gorilla Glass with code Gorilla 2320 from Corning Inc. was used for the experiment.

Infrared Thermal Camera

FLIR® Silver SC5000 Medium Wave Infrared (MWIR) camera has been employed for thermography. It has a highly sensitive Indium Antimonide (InSb) focal plane array for IR measurement. The thermal camera can be operated up to 380 Hz at full frame rate. The camera has a 27 mm embedded lens with focal number f/3. For the current experiments, medium wave G3 F/3.0 lens with magnification number 3 ± 5% was employed. The MW G3 lens operates at the spectral band of 3.7 µm to 5.15 µm. The focal point of the lens is 38.8 mm ± 0.01 mm from the objective lens. The

resolution at which the camera can be operated using MW G3 lens is 320 × 256 for 30 µm pitch detector and 630 × 512 for 15 µm pitch detector. Thus, small area temperature can be precisely measured with high accuracy.

Hot plate

Heidolph MR Hei-Tee hot plate was used to heat the Gorilla Glass. The maximum temperature of the hot plate is 300^{o}C. For the calibration, the temperature was increased from 20^{o}C to 240^{o}C.

Thermocouple

Two Type K thermocouples with a tip diameter of 0.2 were employed. The accuracy of the thermocouples is +/- 1°C. Two thermocouples were used to measure the surface temperature of the black painted gorilla glass.

The thermocouple readings were recorded by a four-channel data logging thermometer purchased from General Tools. It has a full-scale operating range of -200^{o}C to 1260^{o}C. The minimum response time of the data logger is 1s. The resolution of the thermocouples' data logger is 0.1^{o}C with an accuracy of ± 2^{o}C.

Thermal bonding epoxy

To ensure proper thermal contact between the thermocouple and the Gorilla Glass, TBS Thermal bonding epoxy purchased from RS Components Pte. Ltd. was used. The thermal conductivity and specific heat capacity of TBS bonding epoxy are 1.1 W/mK and 0.5 cal/g/^{o}C (at 30 ^{o}C) respectively.

Paint

To ensure the emissivity from the surface is close to unity, PNM400 black paint purchased from RS Components Pte. Ltd. was used to paint the surface under observation.

Calibration experimental setup

The experimental setup for the calibration experiment is shown in Figure A1-2 and Figure A1-3. Figure A1-2 shows the setup of two Type K thermocouples used for the surface temperature reading of the chemically strengthened glass painted with PNM400 black paint. Figure A1-3 shows the setup of a thermal camera over the glass sample to measure the temperature field.

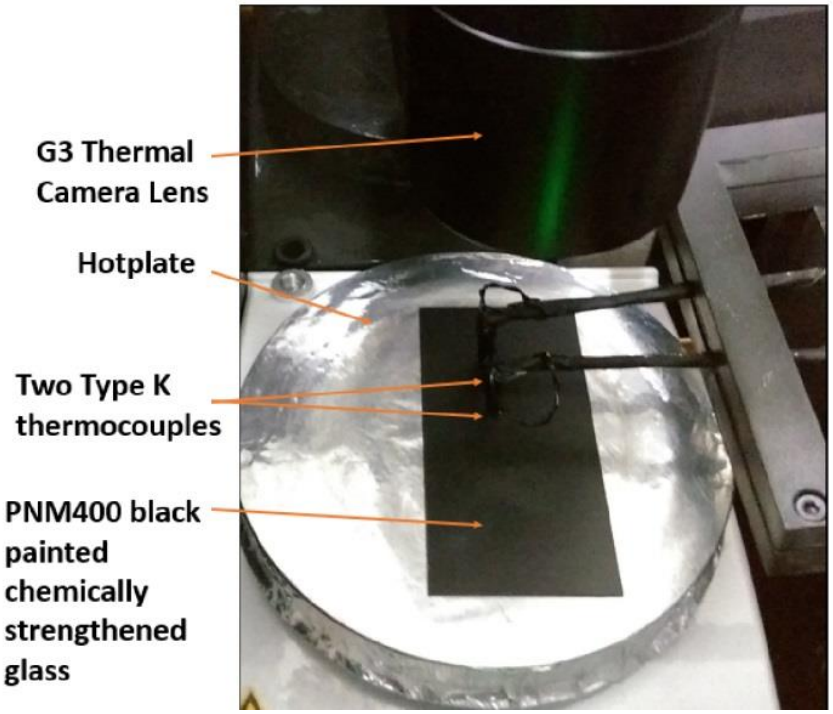

Figure A1-2: Two Type K thermocouples setup for calibration experiment.

Figure A1-3: FLIR® MWIR SC5000 thermal camera focused on black painted Gorilla Glass surface inside the black painted enclosure to minimize surrounding thermal irradiation reflection.

Black painted Gorilla Glass was laid flat over the hot plate. Before the calibration experiment, temperature distribution was recorded using a 27 mm embedded f/3 lens. Figure A1-4 shows the temperature distribution over the black painted Gorilla Glass at mean temperatures of 49.1°C and 66.78°C. The average temperature has been calculated over the surface of black painted Gorilla Glass as recorded by the thermal camera before the calibration experiment. The temperature distribution experiment had been performed using a 27 mm embedded f/3 lens.

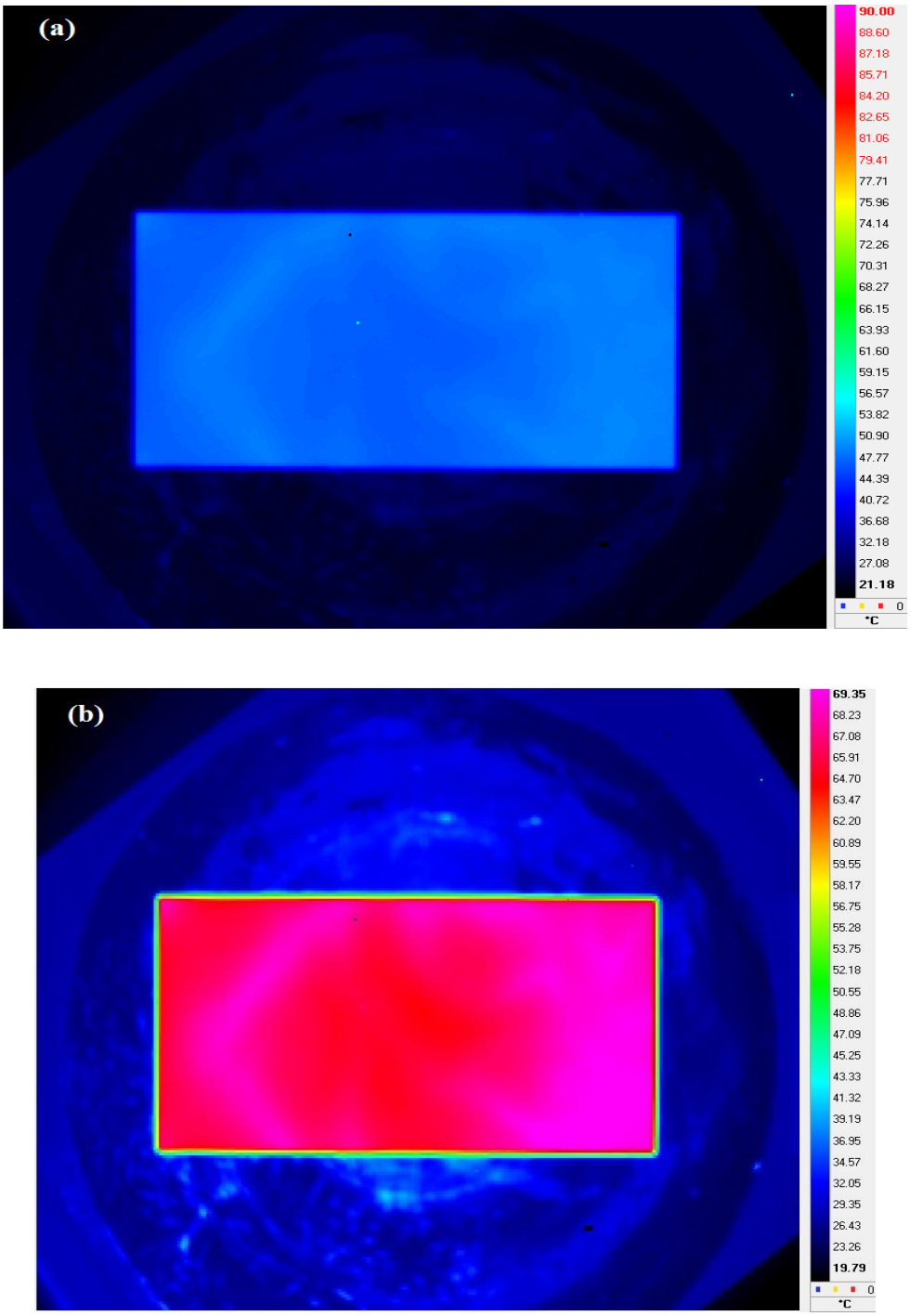

Figure A1-4: Temperature distribution over the surface of glass observed by 27mm lens with mean temperatures (a) 49.1°C (b) 66.78°C

The standard deviations of temperature measured by the thermal camera at mean temperatures 49.1°C and 66.78°C were 0.83°C and 1.47°C respectively. Their coefficient of variation of temperature calculated by equation A1-3 is less than 3%. Thus, it can be assumed that the average value can represent the temperature distribution with low variability. This measured temperature has been correlated to the average of the two thermocouple readings.

$$c_v = \frac{\sigma}{\mu} \qquad \text{(A1-3)}$$

Where c_v is the coefficient of variance of temperature, σ is the standard deviation of temperature distribution over the sample surface and μ is the mean of temperature distribution over the sample surface.

For calibration experiment, MW G3 lens with 3x magnification was used. The lens was focused at the surface of the glass by maintaining its objective lens 38 mm above the glass surface. Figure A1-5 shows the image taken by the thermal camera at a mean temperature of 65.06°C.

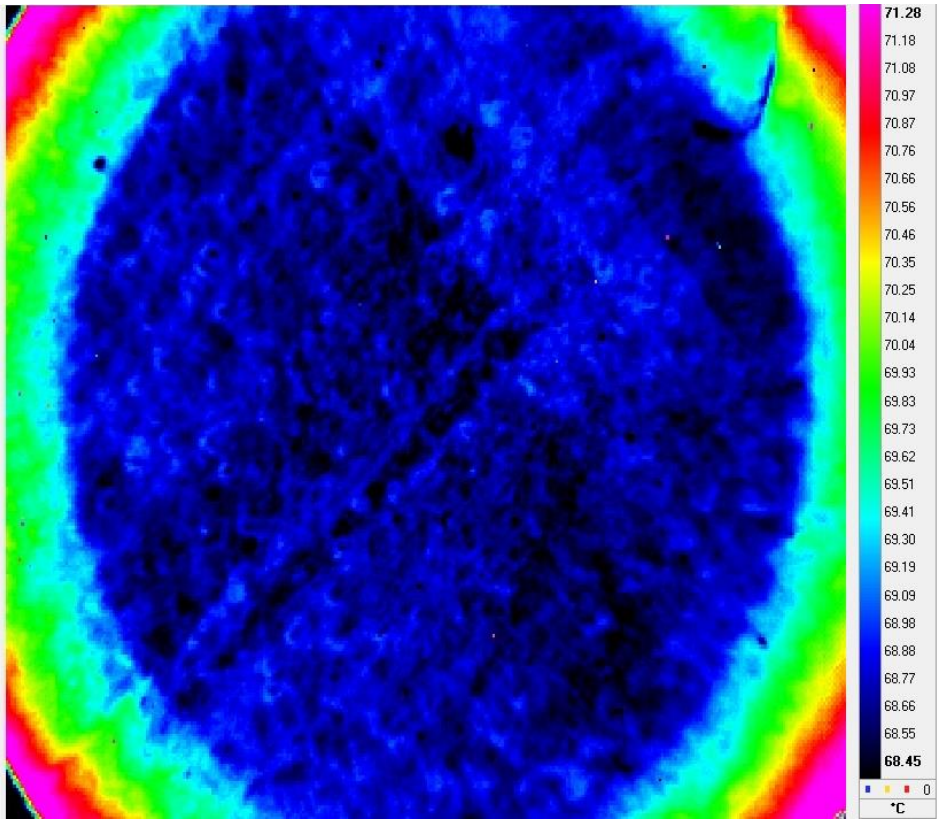

Figure A1-5: Focused thermal image taken by MW G3 lens at a mean temperature of 65.06^{o}C.

The readings for the calibration of temperature distribution were performed according to the procedure as described in SC5000 software calibration manual provided by FLIR:

1. 22 points were chosen to start from 20^{o}C to 240^{o}C with a step size of 10^{o}C . Hot plate temperature was set to these determined temperatures. Each reading for thermal camera or thermocouple was taken when the steady-state temperature was obtained.
2. When a steady state was reached, around 100 frames at 50 Hz sampling frequency were recorded. All the frames were averaged to get a single

frame average to eliminate time-varying noise. Figure A1-5 is an example of an averaged frame. Simultaneously, the temperature readings from the thermocouples were recorded.

3. In the averaged frame, area for the "approximate" black body (black painted Gorilla Glass) was determined; data was extracted with circular area selection tool. Over the selection area the average temperature, T_{cam}, was calculated. Table A1-2 shows all the recorded data of the two thermocouples (T_1 and T_2).

Table A1-2 Reading for thermocouples and thermal camera. T_1 and T_2 are thermocouple readings over the surface of black painted Gorilla Glass 2320. T_{avg} is the average of temperatures T_1 and T_2. T_{cam} is the averaged temperature reading of the thermal camera.

S.N.	T_1	T_2	T_{avg}	T_{cam}	S.N.	T_1	T_2	T_{avg}	T_{cam}
1	23.16	23.24	23.20	22.68	12	125.82	130.32	128.07	134.66
2	40.21	40.12	40.17	40.99	13	134.88	140.42	137.65	145.76
3	41.43	41.22	41.33	42.39	14	144.15	150.81	147.48	156.49
4	57.74	58.09	57.92	60.72	15	155.59	162.56	159.08	166.58
5	55.40	55.17	55.29	58.35	16	161.89	169.25	165.57	174.57
6	65.42	65.84	65.63	69.72	17	170.38	177.63	174.01	181.56
7	77.05	77.80	77.43	82.30	18	181.30	190.24	185.77	192.56
8	86.51	88.11	87.31	92.89	19	185.44	193.66	189.55	196.22
9	94.41	95.70	95.06	100.76	20	199.15	209.33	204.24	207.25
10	107.46	109.84	108.65	114.80	21	219.00	229.11	224.06	224.08
11	114.17	117.27	115.72	121.32	22	228.70	237.50	233.10	239.64

Moreover, average temperature readings of the averaged frame from the camera were correlated with the average temperatures of the two thermocouples. Figure A1-6 shows the correlation curve with the associated R^2-value.

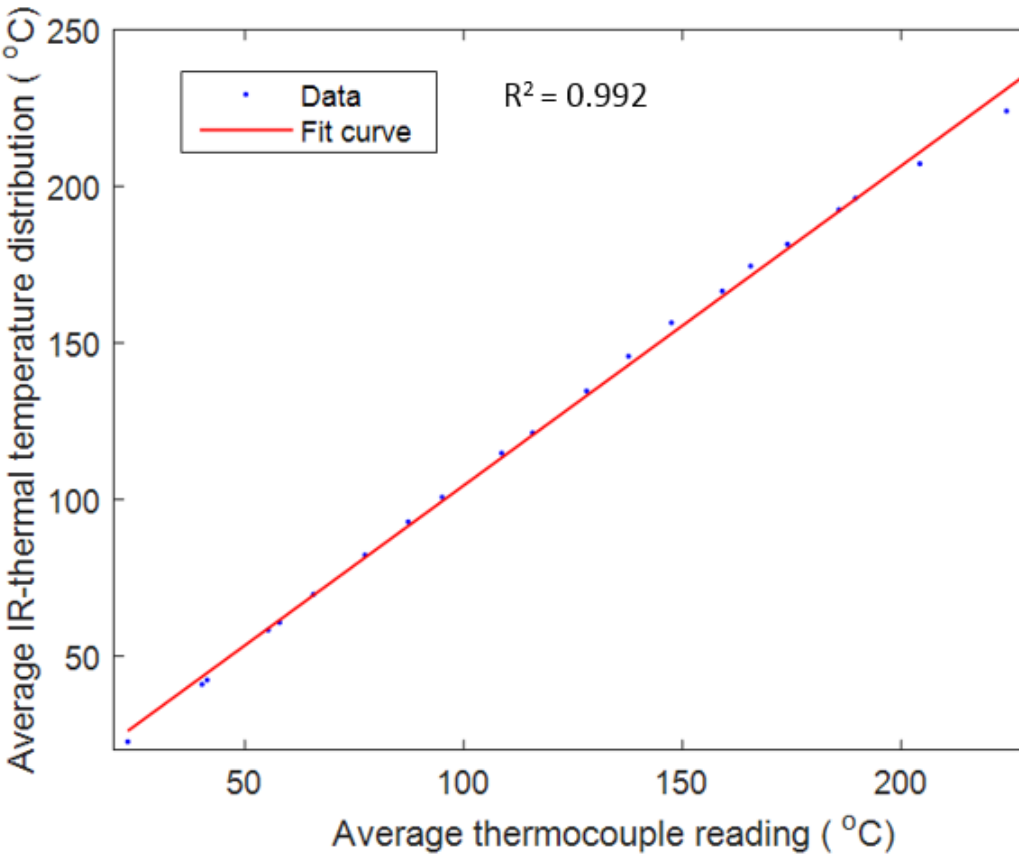

Figure A1-6: Correlation between average thermocouple reading and thermal camera temperature reading with R^2-value

From the correlation, the equation for conversion of the thermal camera readings to actual temperatures was calculated as:

$$T_{act} = 0.978 \cdot T_{cam} - 2.17 \qquad \text{(A1-4)}$$

Equation A1-4 has been employed for the conversion of the thermal camera temperature readings to the actual temperatures in all the subsequent analyses.

Appendix II

Numerical differentiation

The rate of change of any function *y = f(x)* with respect to the independent variable *x* is given by the first derivative of the function as:

$$f'(x) = \frac{dy}{dx} \tag{A2-1}$$

It is not always possible to determine analytically $f'(x)$. Instead, $f'(x)$ may be approximated numerically. The approximation of $f'(x)$ using a three-point forward difference formula can be written as:

$$f'(x) \approx \frac{-3f(x) + 4f(x+h) - f(x+2h)}{2h} \tag{A2-2}$$

Where h is the step length of the independent variable.

In this investigation, the absorption with respect to z-positions in the Z-scan analysis was known at discrete z-locations. To investigate the nonlinear absorption threshold intensity, the rate of change of absorption A(z) with respect to the z-positions is required. This cannot be evaluated analytically and was determined using equation A2-2 as:

$$A'(z) \approx \frac{-A(z) + 4A(z+\Delta z) - f(z+2\Delta z)}{2\Delta z} \tag{A2-3}$$

Where $A(z)$ is absorption at position z, $A(z+\Delta z)$ and $A(z+2\Delta z)$ are first and second points ahead of point $A(z)$.

Appendix III

Numerical integration

For a function *f(x)*, integration within the limit [a, b] is given as:

$$F(x) = \int_a^b f(x)dx \tag{A3-1}$$

However, it is not always possible to analytically determine the values of *F(x)*, and numerical integration may be required. Trapezoidal integration method, a numerical integration scheme, has been adopted in this investigation. the function *f(x)* as shown in Figure A3-1.

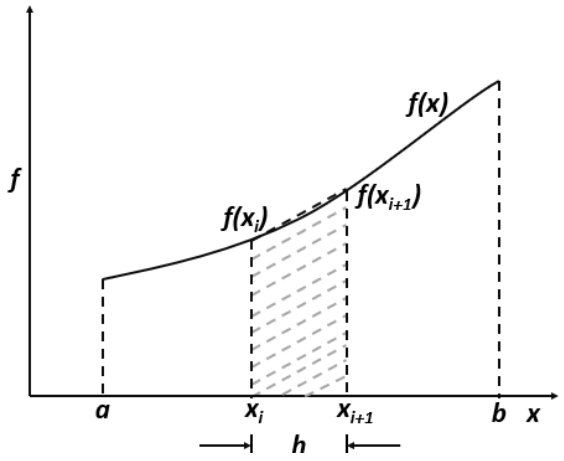

Figure A3-1: Function f(x) vs x

For the function *f(x)* as shown in Figure A3-1, integration of function *f(x)* between x-limits x_i and x_{i+1} is given by the area under the curve *f(x)* between these two x-limits. Thus, the integration can be numerically approximated by calculating the area

of the trapezoid formed, i.e. the shaded region in Figure A3-1. Thus, the integration of the curve between the limits x_i and x_{i+1} can be approximated as:

$$F(x)\Big|_{x_i}^{x_{i+1}} = \int_{x_i}^{x_{i+1}} f(x)dx \approx h \cdot \frac{f(x_i) + f(x_{i+1})}{2} \tag{A3-2}$$

Where h is the difference between x_i and x_{i+1}, also known as the step size. The approximation approaches the actual value as $h \to 0$. If the approximation in equation A3-2 is repeated over the domain between the x-limits [a,b], then the sum of all individual approximation over the step size h will be the overall approximation of integration of the function $f(x)$ between the limits [a,b] given as

$$F(x)\Big|_a^b = \int_a^b f(x)dx \approx \sum_{i=1}^{n-1} h \cdot \frac{f(x_i) + f(x_{i+1})}{2} \tag{A3-3}$$

Where n is the total number of discrete steps. As n increases the value of h decreases giving better approximation of $F(x)\Big|_a^b$.

In this investigation, trapezoidal integration method has been employed for the integration of intensity distribution with respect to the radial and temporal time steps. As all the calculations were performed using Matlab 2014b (a commercial numerical software), an inbuilt function *trapz* in Matlab for trapezoidal integration has been used.

Appendix IV

Calculation of convective coefficient (h)

Convective heat coefficient is given by equation A3.1 [1]:

$$h = \frac{k \cdot \overline{Nu_L}}{L} \tag{A4.1}$$

Where k is the thermal conductivity of material, $\overline{Nu_L}$ is the Nusselt number defined by equation A4.2. L is the characteristics length of the material, and for a rectangle it is defined as the ratio of area to circumference [2].

$$\overline{Nu_L} = 0.68 + \frac{0.670 Ra_L^{1/4}}{\left[1 + \left(\frac{0.492}{\mathrm{Pr}}\right)^{9/16}\right]^{4/9}} \tag{A4.2}$$

Pr and Ra_L are Prandtl and Rayleigh numbers described by equation A4.3 and equation A4.4

respectively.

$$\mathrm{Pr} = \frac{c_p u}{k} \tag{A4.3}$$

$$Ra_L = Gr_L * \mathrm{Pr} \tag{A4.4}$$

In equation A3.3 c_p is the specific heat capacity of air and u is the dynamic viscosity of air. In equation A3.4 Gr_L is Grashof dimensionless number defined by equation A3.5.

$$Gr_L = \frac{g\beta(\mathrm{T}-\mathrm{T}_\infty)\mathrm{L}^3}{v^2} \qquad \text{(A4.5)}$$

where g is the acceleration due to gravity, β is the coefficient of thermal expansion coefficient for air at T_∞ is the ambient temperature, L is the characteristic length and ν is the kinematic viscosity